Performance investigation of VentiFoil ship propulsion

Master of Science Thesis

L.P. Lagendijk

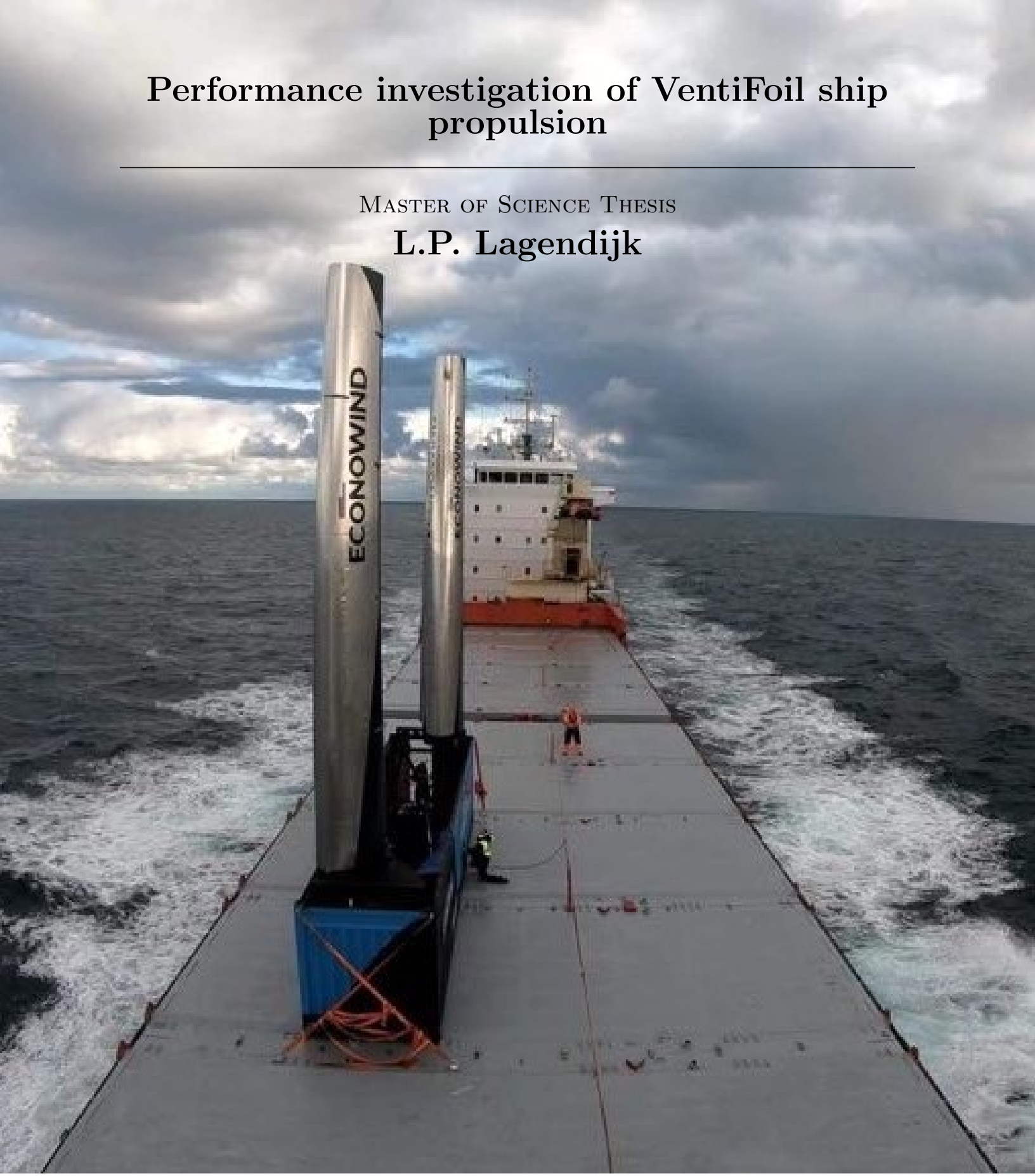

TU Delft ECONOWIND MARIN

Performance investigation of VentiFoil ship propulsion

Research into the propulsive performance of VentiFoils using CFD simulations

---

Master of Science Thesis

To obtain the degree of Master of Science in Marine Technology at Delft University of Technology

L.P. Lagendijk

December 9, 2018

Faculty of Mechanical, Maritime and Materials engineering - Delft University of Technology

Abstract

In recent years the awareness and the effort to reduce air pollution and global warming have increased. Many new ideas are being developed to reduce harmful emissions. Despite this, the shipping industry is still a large contributor to air pollution worldwide. To reduce the environmental impact of shipping, the use of sustainable energy sources such as wind energy on-board ships is being explored.

Wind energy is widely available at sea, the challenge is to harness this energy. The relatively unknown wind propulsion device called the Turbosail is a vertical wing shaped device which uses wind energy to provide thrust. This propulsion technology was invented in the 1980's by the Frenchman Jacques-Yves Cousteau.

This report describes the investigation into the similar wind propulsion device called the VentiFoil. Two retractable VentiFoils are fitted inside a 40 foot container, this ship propulsion device is called the eConowind unit. Multiple eConowind units can be installed on the hatch covers of general cargo vessels. If successful, this wind propulsion device can be applied on many different ships.

The VentiFoil concept will be investigated and improved using Computational Fluid Dynamics (CFD) research tools. These tools are used to simulate the flow around different VentiFoil geometries.

The result of this project will be a better understanding of the working principles of the VentiFoil, sensitivity information for the variation of different characteristic design parameters and an evaluation of the generated forces and performance of VentiFoil propulsion.

Preface

This thesis report is written as part of the Master Thesis project of Laurens-Jan Lagendijk for the study Marine Technology, Science Track, specialization Ship Hydromechanics at Delft University of Technology, the Netherlands.

The opportunity for this project is provided by eConowind BV located in the Netherlands. In order to make use of the expertise and the facilities available at the Maritime Research Institute Netherlands (MARIN), most of the research and the simulations are conducted at MARIN in Wageningen, the Netherlands.

This report provides guidance and clarifies the thesis. The structure of the report is informative whereby report explains the performed analyses.

The report is meant for employees of eConowind, Conoship, teachers of the study Marine Technology at Delft University of Technology, people involved in the VentiFoil project through MARIN and other people involved in the project.

I would like to thank Guus van der Bles and Frank Nieuwenhuis from eConowind BV for the opportunity to work on this topic.
I would like to thank Maxime Garenaux who is a CFD specialist at MARIN for his help end expertise in the use of the Refresco CFD and the post processing software. I would also like to thank Rogier Eggers from MARIN and Tom van Terwisga from the TU Delft and MARIN for their guidance and comments.

Contents

List of Figures

List of Tables

Nomenclature

Symbol	Description	Unit
A_{mat}	Coefficient matrix	–
A_o	Open suction area	m^2
A_{pf}	VentiFoil projected front area	m^2
A_s	Total suction area	m^2
A	VentiFoil projected side profile area	m^2
C_D	Drag coefficient	–
C_L	Lift coefficient	–
C_T	Thrust coefficient	–
C_p	Pressure coefficient	–
C_q	Suction coefficient	–
F_D	Drag force parallel to the wind direction	N
F_L	Lift force perpendicular to the wind direction	N
F_S	Side force in the perpendicular to the heading	N
F_T	Thrust force in the direction of the heading	N
F_x	Force in x direction	N
F_y	Force in y direction	N
L_2	Root mean square convergence norm	–
L_F	Flap length	m
L_∞	Convergence norm for the maximum residual in the domain	–
Ma	Mach number	–
N_p	Number of parameter settings	–
N_s	Number of simulations	–
P_a	Aspiration power	W
P_w	Available wind power	W
P_s	Suction power without losses	W
P	Exponent of the power-law wind profile	–
Q	Suction flux	$\frac{m^3}{s}$
R^2	Coefficient of determination, ranges between 0 and 1 whereby larger values represent a more accurate fit	–
U_a	Apparent wind speed	m/s
U_s	Velocity of the ship	m/s
U_t	True wind speed	m/s
V_{ref}	Far field velocity magnitude	m/s
V_z	Vertical velocity component	m/s
V	Velocity component	m/s
α	Angle of attack, angle between the chord line and the apparent wind direction	°
$\beta_{a,max}$	Maximum apparent wind angle at which thrust can be generated	°
β_a	Apparent wind angle	°
β_t	True wind angle	°
β	Flap angle	°
δ	Boundary layer thickness	–
η_a	Efficiency related to aspiration power	–
η_a	Efficiency realted to available wind power	–
η_{gen}	Efficiency electricity cable	–
η_{gen}	Efficiency of the electrical power generator	–

Symbol	Description	Unit
η_{gen}	Efficiency propulsion power transfer through bearings (and a gearbox)	–
η_{prop}	Propeller efficiency	–
η_s	Suction efficiency to account for aspiration power losses	–
κ	Suction surface permeability	–
λ_T	VentiFoil constant taper ratio	–
λ_c	VentiFoil chord taper ratio	–
λ_t	VentiFoil thickness taper ratio	–
λ_w	Weibull distribution scale parameter	–
λ	Leeway angle, angle between the heading coarse of the ship	°
σ	Standard deviation	–
θ_m	Angle between the middle of the suction region and the chord axis	°
θ	Angular extend suction region	°
φ	Solution vector	–
a	Bezier curve shape parameter	–
b	Right hand side vector	–
c_{bottom}	Chord length at the bottom of the VentiFoil	m
c_{top}	Chord length at the top of the VentiFoil	m
c	Speed of sound	m/s
c	Chord length	m
h	Bezier curve shape parameter	–
k_w	Weibull distribution shape parameter	–
k	Curvature	m^{-1}
p_∞	Far field pressure	Pa
p_c	VentiFoil chamber pressure	Pa
p_s	Suction pressure	Pa
s_m	Spacing margin inside the container from the moving Ventifoil surface	m
s	Span	m
t_{bottom}	Profile thickness at the bottom of the VentiFoil	m
t_{tip}	Thickness of the flap tip	m
t_{top}	Profile thickness at the top of the VentiFoil	m
t	Maximum profile section thickness	m
u^+	Dimensionless wall distance	–
u_∞	Far field velocity	m/s
u	Velocity	m/s
x'	Relative x location along the chord from the leading edge	m
y^+	Dimensionless wall distance	–

Acronyms

AIAA	The American Institute of Aeronautics and Astronautics
CAD	Computer Aided Design
CFD	Computational Fluid Dynamics
ECMWF	European Centre for Medium-Range Weather Forecasts
EEDI	Energy Efficiency Design Index
FOM	Figure Of Merrit
GMRES	Generalized minimal residual method
MARIN	Maritime Research Institute Netherlands
NACA	National Advisory Committee for Aeronautics
RANS	Reynolds Averaged Navier-Stokes
SST	Shear Stress Transport
TVD	Total Variation Diminishing
URANS	Unsteady Reynolds Averaged Navier-Stokes
WASP	Wind Assisted Ship Propulsion

Introduction

The objective of naval architects is to make shipping and ships as efficient as possible. This can among others be achieved by optimization of the resistance characteristics and propulsion systems of ships, with the aim to improve energy efficiency. This report addresses a new means of ship propulsion in the form of the eConowind unit which features VentiFoils to provide wind propulsion.

Cargo ships originally used to exploit wind energy as a means of propulsion whereby thrust was provided by sails. These wind propelled ships used to be the norm but with the invention of the marine engine, the widespread use of commercial wind propulsion has disappeared. Fossil fuels have become the new prevalent energy source used to propel cargo vessels. As fuel cost make up a large part of the operational expenses of ships, the fuel price significantly influences the design of ships. High fuel prices can stimulate the exploration of different energy sources and propulsion methods. During the 1980's the high fuel prices have lead to the invention and development of the turbosail concept by the French research group consisting of Jacques-Yves Cousteau, Lucien Malavard and Bernard Charrier. In this report, turbosail type airfoils will be referred to as VentiFoils.

Due to changes in regulations such as the requirement for the majority of new vessels to have an Energy Efficiency Design Index (EEDI). In recent years emissions have become more significant design consideration. This provides an additional incentive to explore the use of alternative energy sources such as wind energy. Wind propulsion can be applied in addition to conventional propulsion. This concept is called Wind Assisted Ship Propulsion (WASP). For this project the use of an eConowind WASP system is investigated to reduce the propulsion power required to propel the ship whereby the speed of the ship is not changed. The eConowind unit provides a modular propulsion unit which allows for easy and quick installation, automated operation and retractable VentiFoils inside the form factor of a 40 foot container.

Based on prior research into the application of wind propulsion, the VentiFoil concept is deemed best [11] and most feasible. There are however uncertainties regarding the factors influencing propulsive performance of VentiFoils. Uncertainties in the application of the suction boundary condition and interaction of multiple VentiFoils are described in the thesis report of A. Kisjes [9] written in 2017. These aspect will be investigated in this report. From the eConowind company, there is a desire to investigate and improve the propulsive performance of VentiFoils. Therefore the aim is to investigate the propulsive performance of VentiFoils by variation of parameters using CFD analyses.

The scope of this project is to investigate the performance of Ventifoil propulsion by variation of geometric section parameters of the flap angle, flap length, leading edge shape, thickness ratio, suction width and suction extend. The tip effects will also be investigated by variation of the span and different applications of an end plate at the tip of the VentiFoil. The effect of interaction between two VentiFoils will also be examined.

The first chapter describes wind propulsion and the working principles of the VentiFoil propulsion and the eConowind unit. The wind and operating conditions are described in the second chapter. The third chapter contains the description of the the simulation and numerical evaluation of the flow around VentiFoils. The fourth chapter describes 2D simulations, domain and grid sensitivity and the parametric investigation of VentiFoil section parameters. The fifth chapter describes the domain and grid sensitivity in 3D, the tip effects at the tip of a VentiFoil and interaction between two VentiFoils. The sixth chapter contains the investigation into an improved geometry based on a best guess with knowledge from the previous chapters. The seventh and last chapter describes the conclusions and provides recommendations for the VentiFoil design and recommendations for continuation of the research project and area's where further research is needed.

Chapter 1

Ventifoil wind propulsion

This chapter describes the working principle of VentiFoils as a propulsive device for the use on commercial ships whereby the VentiFoils are fitted inside an eConowind unit.

1.1 Wind assisted ship propulsion

The efficiency of wind propulsion depends on the wind conditions and on the velocity of the vessel. Slower travelling vessels are more favourable for WASP propulsion as the prevalent apparent wind angle (β_a) is more often favourable. The ship type considered for this research assignment is a coaster type vessel with an operational area of Northern Europe, considering the North and Baltic Sea.

When applying wind propulsion systems on a ship, the influence of these systems on the ship operations must be minimal. To ensure easy loading and offloading, the wind propulsion system should be easily removable and the occupied deck area must be minimal. Therefore the size of the propulsive installation is minimal and wind propulsion system should feature a large thrust coefficient (C_T) such that large thrust can be generated for a relatively small airfoil. The VentiFoil has the potential to meet these requirements.

1.2 VentiFoil geometry

Before the VentiFoil unit can be improved, the working principles behind the VentiFoil as an airfoil must be understood.
The VentiFoil is an aspirated wind propulsion device which is designed for ship propulsion. It consists of a vertically orientated airfoil profile as shown in Figure 1.1. To prevent boundary layer separation and achieve large lift coefficients (C_L), the VentiFoil features boundary layer suction on the leeward side along the span of the airfoil. To be able to use the VentiFoil on both port and starboard tack, the profile shape is line symmetrical over the chord axis. The profile features a flap which can rotate around the trailing edge to seal the windward suction region and to ensure flow separation behind the profile. The entire VentiFoil can rotate around the vertical axis to be able to trim the angle of attack such that maximum thrust can be generated for different apparent wind angles. This is equivalent to the sheeting angle on a conventional sail.

The VentiFoil as described by [11] features a thick (bluff body) profile. This profile shape is selected based on internal and external flow. A relatively thick profile allows for a large suction chamber. This reduces internal losses, ensures the vertical pressure distribution is more constant over the suction area and allows for the application of a larger fan diameter.

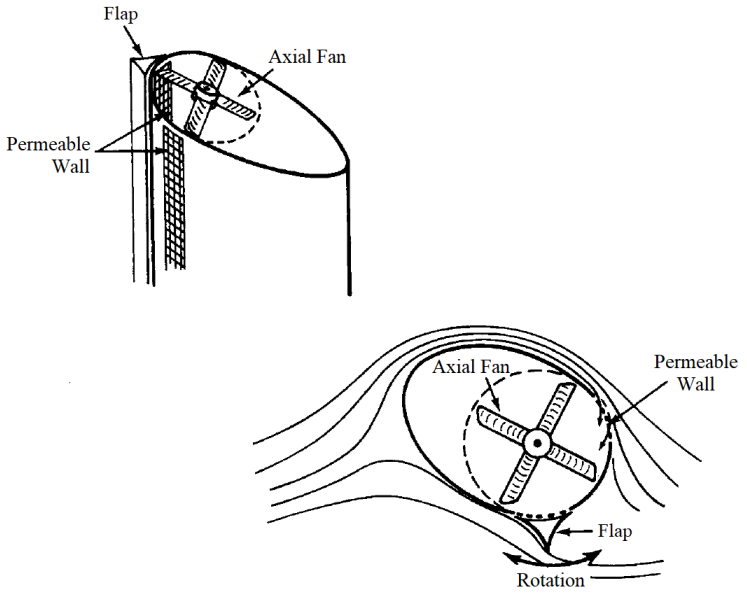

Figure 1.1: Schematic VentiFoil representation, fan located at the top [11]

The characteristic dimensions for a VentiFoil are defined in Figure 1.2 and Figure 1.3. Based on these dimensions, characteristic parameters for the shape of the VentiFoil can be derived. The projected side area is defined in Equation 1.1. The VentiFoil chord taper is defined as Equation 1.2. The VentiFoil thickness taper is defined as Equation 1.3. When the profile thickness ratio does not change over the span, the constant taper ratio is defined as $\lambda_T = \lambda_c = \lambda_t$.

$$A = \bar{c} \cdot s \tag{1.1}$$

$$\lambda_c = \frac{c_{top}}{c_{bottom}} \tag{1.2}$$

$$\lambda_t = \frac{t_{top}}{t_{bottom}} \tag{1.3}$$

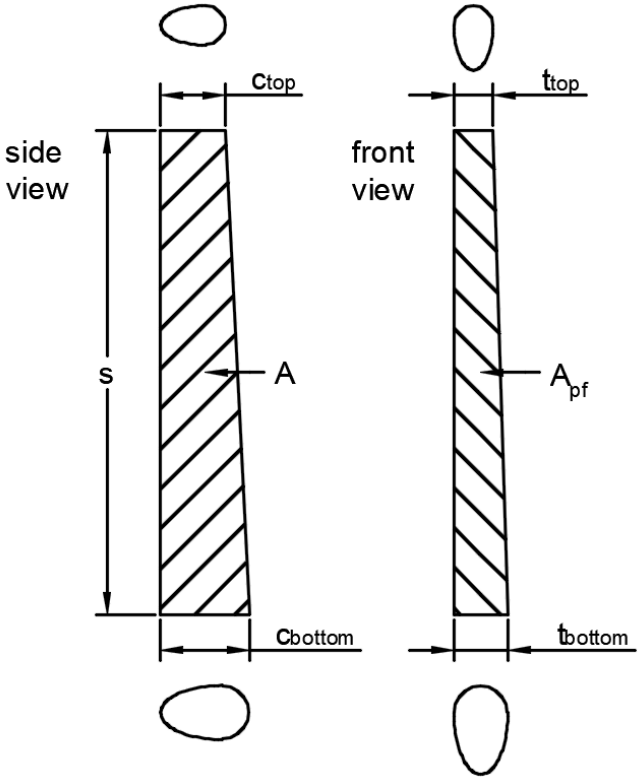

Figure 1.2: Dimensions and nomenclature of the VentiFoil

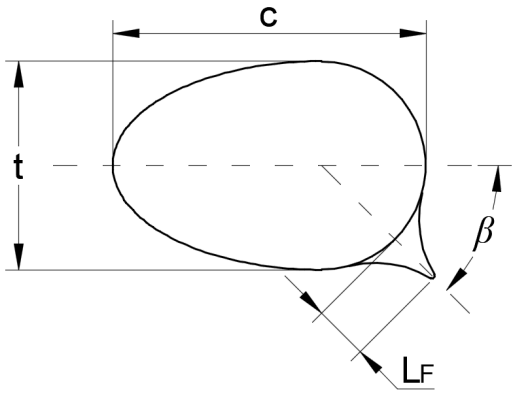

Figure 1.3: Section dimensions of the VentiFoil

1.3 eConowind unit

The eConowind unit is a modular wind propulsion unit in the form of a 40 foot container, containing two retractable VentiFoil type airfoils. The form-factor of a container allows for application on many ships and quick installation ("plug and play") as many general cargo vessels have space and twist-lock connections available on the hatch covers to place one or multiple eConowind units. The eConowind unit will be oriented lengthwise on the ship as the conventional container orientation. This is shown in Figure 1.4. The ability to fold both VentiFoils into the container allows for easy installation when the module is folded. This also enables the eConowind unit to be turned off and the VentiFoils to be retracted when no beneficial thrust is generated or to prevent damage in case of a storm.
The maximum dimensions of the VentiFoil and therefore the thrust of a single eConowind unit is limited by the dimensions of the VentiFoils and therefore by the size of the container. To increase the wind propulsion, multiple eConowind units can be installed.

The most efficient location to apply the eConowind depends on the wind speed as explained by [9]. For limited side forces, the side force is most efficiently produced by the rudder. Therefore the preferred location of the eConowind unit in conditions with limited side force is at the aft of the ship. However in stronger wind conditions and larger side forces, the use of the rudder to counteract the side force produced by the VentiFoils can require significant rudder angles such that the maneuverability of the ship is reduced in large wind conditions. To remain manoeuvrable, the rudder angle must not be close to the rudder angle of maximum lift. To be able to operate the eConowind unit in stronger wind conditions with larger side forces and to retain manoeuvrability, the side force must largely be produced by the hull. This means a larger induced resistance for light wind conditions because the hull is less efficient lifting body to counteract the side force compared to the rudder. However the manoeuvring capability is less negatively affected. Therefore the preferred eConowind location is at the bow of the ship as concluded by [9] whereby the side force is mainly counteracted by lift from the hull of the ship as the result of a leeway angle.

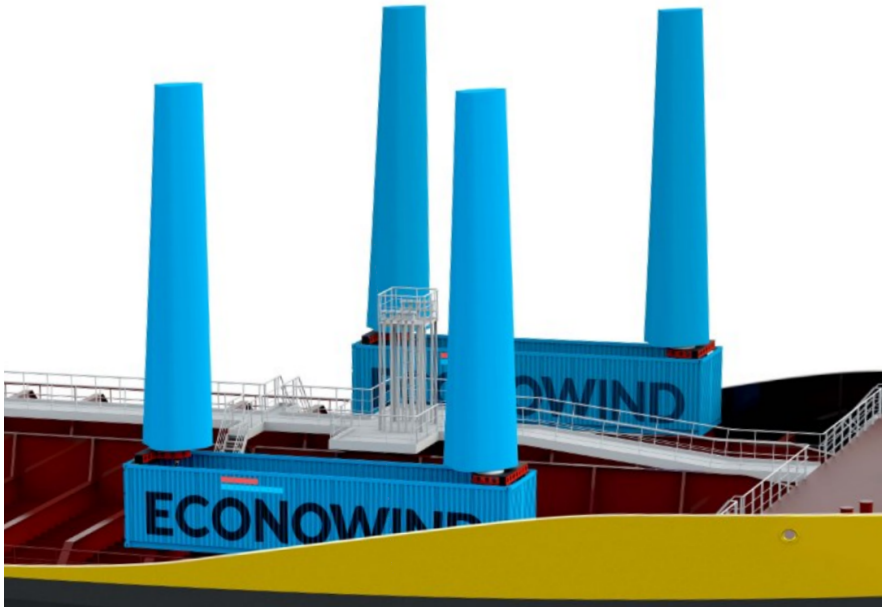

Figure 1.4: Impression of two eConowind units installed on the deck of a ship

1.4 Figure of merit

The Figure Of Merrit (FOM) provides a measure of the efficiency gain of VentiFoil wind propulsion. The efficiency of VentiFoil propulsion can be evaluated by comparing the energy input as aspiration power and the effective energy output based on the delivered thrust and the ship's speed. The suction power without losses can be obtained from the pressure difference between the far field pressure and the chamber pressure and the total suction volume flux as defined by [14] and expressed in Equation 1.4. The aspiration efficiency is expressed in Equation 1.6. Aspiration efficiency's (η_a) larger than 1 means the eConowind generates more propulsive power than the required aspiration power.

$$P_s = (p_\infty - p_c)Q \tag{1.4}$$

$$P_a = \frac{P_s}{\eta_s} \tag{1.5}$$

$$\eta_a = \frac{F_T U_s}{P_a} \tag{1.6}$$

The purpose of the eConowind unit is to reduce the propulsion power required to propel the ship. Therefore the eConowind can be considered beneficial when the propulsive efficiency exceeds the propulsive efficiency of the conventional propulsion system. These efficiency's are expressed in Equation 1.7 as a fraction to obtain the FOM. A FOM larger than 1 indicates that propulsion by the eConowind unit is more efficient compared to conventional propulsion. As $\eta_a \gg 1$, the FOM is generally also much larger than 1 because the propulsive efficiency of the eConowind unit is generally much better compared to the efficiency of the conventional propulsion unit. This is because the eConowind unit exploits wind energy and only requires relatively small aspiration power.

The FOM can be used to evaluate the optimum aspiration power and therefore determining at which C_q more aspiration power results in more efficient thrust. For large wind speeds, the fan will be operating at maximum aspiration power. However when the wind speed is lower the aspiration power should be tuned such that most efficient propulsion is obtained. This can mean the suction is not maximum for small wind

velocities. When the derivative of the FOM with respect to the aspiration power (P_a) is zero, the conventional propulsion unit is equally efficient to eConowind propulsion.

$$FOM = \frac{\eta_{gen}\eta_{cable}\eta_a}{\eta_{transfer}\eta_{prop}} \tag{1.7}$$

As the eConowind unit is generally more efficient in providing thrust compared to the conventional propulsion unit. It is desirable to generate as much thrust as possible using the eConowind unit. Therefore the eConowind unit is designed to obtain maximum thrust from a single unit. The thrust is limited by the wind conditions, the total VentiFoil area which can be fitted inside the container dimensions of the eConowind unit and by the maximum aspiration provided by the fan. The produced forces may also be limited by the structural strength of the connection of the eConowind unit to the deck of the ship and the stability of the ship.

1.5 Airfoil working principle

When a fluid moves past an object, the direction in which the fluid moves is changed due to the fluid exerting a pressure on the surface of the object. This pressure results in a force on the object. This force can be divided in lift and drag components whereby lift is defined as the resulting force in the direction perpendicular to the far field flow and drag is defined as the force parallel to the far field flow. Airfoils are devices which generate lift when moving through a fluid. For many airfoil applications the goal is to generate maximum lift for minimum drag. This is referred to as the C_L/C_D ratio. This ratio is used as an expression for the lifting efficiency of an airfoil.

$$C_L = \frac{F_L}{\frac{1}{2}\rho U_a^2 A} \tag{1.8}$$

$$C_D = \frac{F_D}{\frac{1}{2}\rho U_a^2 A} \tag{1.9}$$

The generation of lift works on the principle that the direction of linear momentum of the fluid passing the airfoil is changed. Based on this principle, the generation of a lift force is always accompanied by a drag force. Both lift and drag forces can be increased by increasing the angle of attack. This is defined as the angle between the far field flow direction and the chord of the airfoil (α) as shown in Figure 1.5.

1.6 Resulting forces

The forces generated by the eConowind unit influence the ship similar to how a sailing yacht is influenced by the forces acting on the sails. The forces generated by WASP propulsion are relatively small compared to the total propulsive force. Therefore the effects are smaller compared to fully wind propelled vessels. However these forces still need to be accounted for if they significantly influence the behaviour of the ship.

The eConowind unit generates lift (F_L) and drag forces (F_D). For propulsion purposes, the thrust force is most interesting. Therefore the lift and drag forces are translated into thrust (F_T) and side forces (F_S) using Equation 1.10. This translation depends on the apparent wind angle (β_a). The thrust force can be increased by increasing the angle of attack as this increases the lift and drag forces until flow separation before the suction region occurs.

$$\begin{bmatrix} F_T \\ F_S \end{bmatrix} = \begin{bmatrix} cos(\frac{\pi}{2} - \beta_a) & -cos(\beta_a) \\ sin(\frac{\pi}{2} - \beta_a) & sin(\beta_a) \end{bmatrix} \cdot \begin{bmatrix} F_L \\ F_D \end{bmatrix} \tag{1.10}$$

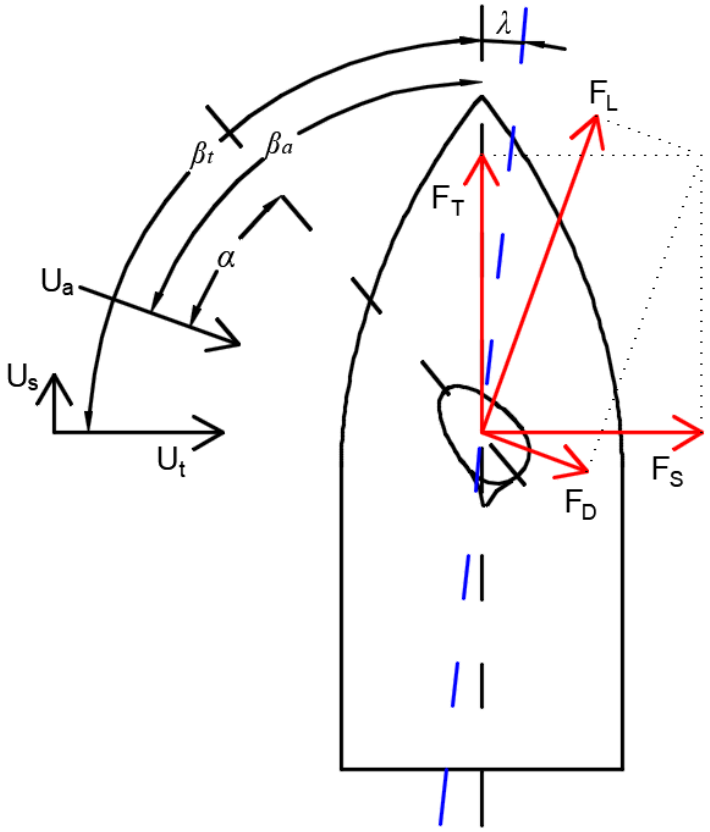

Figure 1.5: Schematic representation of the angles and generated forces on a vessel

The delivered thrust imposes a pitching moment resulting in a trim change of the ship. The longitudinal stability of a general commercial cargo ship is large compared to the imposed moment. Therefore the trim change is assumed small and can be neglected.
The side force generates a heeling moment, this causes the ship to heel towards leeward as usually seen on sailing ships. This heeling moment is assumed small compared to the size of the transverse stability of the ship. This heel can possibly be compensated by ballasting. The effect of heel is therefore neglected and is assumed not to influence the flow over the VentiFoils. The side force is counteracted by forces from the rudder and the hull. To generate these lifting forces, a leeway angle (λ) is imposed on the heading of the ship. This leeway angle results in an induced resistance. Even though the submerged body of a general cargo vessel is not an efficient lifting device. The induced resistance is assumed small with respect to the overall ship resistance. The leeway angle is also assumed small and is therefore neglected.

The forces generated by the eConowind unit must be transferred to the ship by the connection of the eConowind unit to the hatch covers. These connections, the hatch covers and the other supporting structure must be capable of handling the additional loads from the eConowind unit. In conditions when the loads surpass the capability of the structure, VentiFoil aspiration can be turned off and the VentiFoils can be retracted into the container.

The forces on the VentiFoils are pressure dominated. For both 2D and 3D simulations, the magnitude of the force due to friction is less than 0.4% of the total force acting on the VentiFoil.

1.7 Separation control

The eConowind unit requires a relatively small deck area. This can be achieved because VentiFoils have the ability to generate large lift coefficients provided that the angle of attack and the applied suction are

sufficiently large. The lift of an airfoil can be increased by increasing the angle of attack. Therefore to obtain more thrust, large angles of attack are required. Large angles of attack can cause the adverse pressure gradient over the lifting surface to increase. This adverse pressure gradient causes the surface flow in the boundary layer to lose momentum which ultimately can lead to reversed flow and separation of the boundary layer. This is illustrated in Figure 1.6. The location where the flow separates is defined as the location where $\frac{\partial u}{\partial y} = 0$.

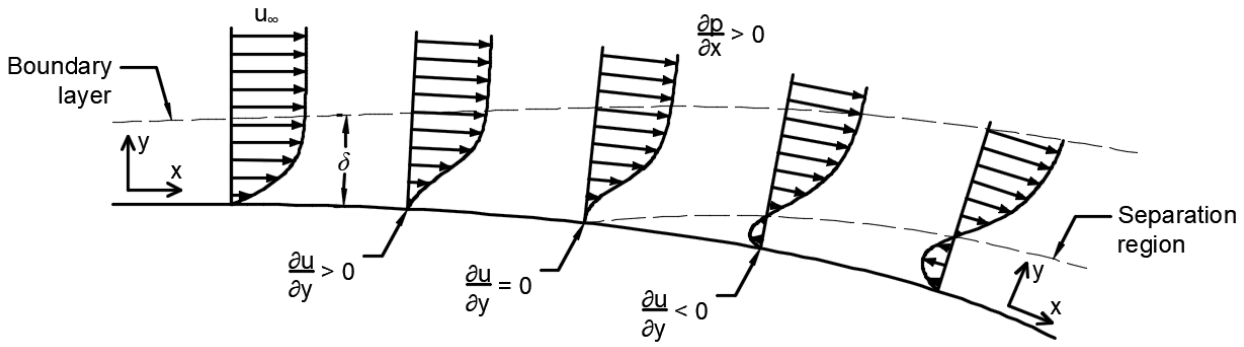

Figure 1.6: Schematic representation of boundary layer separation

On most airfoils separation of the flow, also known as stall, is undesired as it generally results in loss of lift and increase in drag. By ensuring the pressure along the airfoil does not rapidly increase, separation of the flow can be delayed or prevented. For large angles of attack boundary layer separation can be avoided by preventing the surface flow in the boundary layer to loose momentum. This can be achieved by multiple methods. One method is to blow high velocity air into the boundary layer under an angle to increase the momentum in the boundary layer. Another method is to mix the low momentum flow inside the boundary layer with the fast moving flow outside the boundary layer. This can be achieved by making the flow turbulent for example by using vortex generators as sometimes seen on airplane wings. Separation can also be controlled by removing the low momentum air form the boundary layer using suction. The VentiFoil uses suction to control the boundary layer separation whereby the low momentum air is removed from the surface of the airfoil using suction holes. Only a part of the boundary layer has to be removed as stated in [1]. The shape of the VentiFoil is such that flow separation deliberately occurs at the trailing edge. This flow separation is unsteady and can lead to periodic fluctuations in the lift and drag due to vortex shedding. To prevent structural damage, the period of this behaviour should not be close to the resonating frequency of the turbosail profile. This method of boundary layer suction is only feasible at low advection velocities because otherwise the required suction flux and consequently the required power will become large. This is because the required suction increases linearly proportional with the advection velocity as shown in Equation 1.11. The parameter of C_q can be used to determine the required suction for different apparent wind speeds. This parameter is often used in literature [11] whereby the flow behaviour is assumed similar for different apparent wind speeds but the same values of C_q. This also influences the lift and drag obtained from a VentiFoil profile as shown in Figure 1.7.

$$C_q = \frac{Q}{AU_a} \tag{1.11}$$

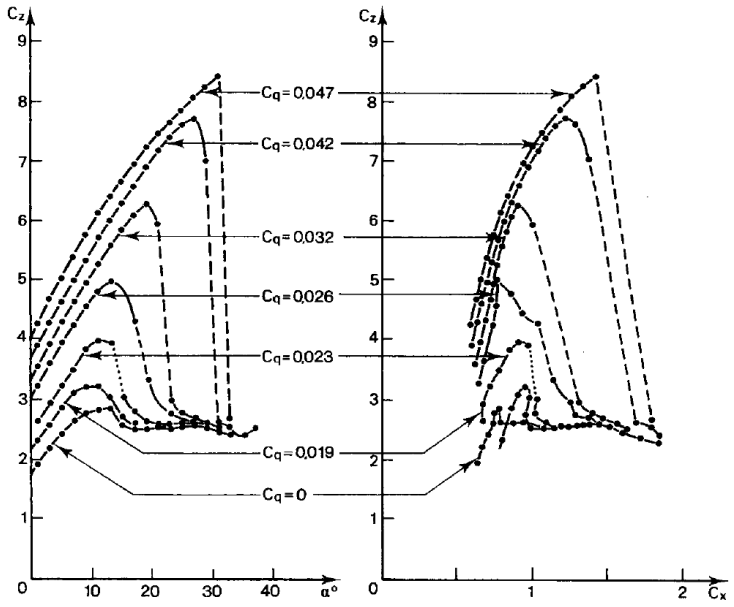

Figure 1.7: Lift and drag coefficients for different angles of attack and C_q from [11]

Due to boundary layer suction in the separation region, the VentiFoil can be used at large angles of attack and therefore generate larger lift coefficients compared to non aspirated airfoils. The effect of suction on the boundary layer is represented in Figure 1.8.

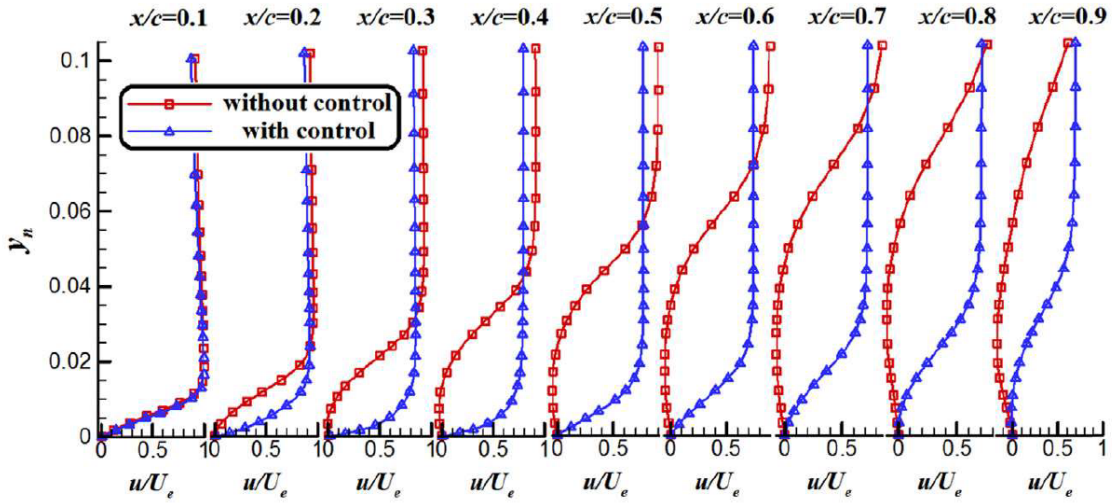

Figure 1.8: Averaged boundary layer velocity distribution comparison with and without suction control on a NACA0012 airfoil [18]

1.8 Suction

The VentiFoil features distributed suction whereby the pressure difference is provided through a perforated surface which connects the outside flow to the chamber inside the turbosail. The pressure inside the chamber is lower compared to the outside pressure, therefore this pressure difference causes suction of the boundary layer. The low pressure inside the chamber is provided by an axial fan which is located at the bottom of the Turbosail profile. This location allows for a large fan diameter and keeps the motor close to the rotation axis when unfolding. The aspirated air will be exhausted vertically at the bottom of the VentiFoil. The air could

also be exhausted at the top as applied by [1]. For this study, the exhaust will be located at the bottom based on structural considerations. An overview of applied suction configurations in literature is given in Table 1.1.

Table 1.1: Suction parameters of the thickness ratio(t/c) and the width (θ), location (θ_m) and permeability (κ) of the suction region as obtained from literature

Source	Test method	t/c	θ [°]	θ_m [°]	κ	Perforation type
[4]	CFD, potential	0.5-0.7	45	*72.5*	-	-
[3]	CFD	0.67	35	62.5	-	-
[13]	CFD, URANS	0.66	24-48	*66-78*	0.5	-
[12]	CFD	*0.67*	48	*62*	*0.5*	slots
[17]	Model test	1	-	-	0.4	holes 4mm
[6]	Model test	1	30	50-190	0.18	holes 2mm

The perforated surface should be located such that the low momentum flow is removed from the boundary layer. Because the suction is more effective for thin boundary layers as stated in [5]. The suction region should be located close to the location where the boundary layer starts to separate ($\frac{\partial u}{\partial y} \geq 0$). The parameters defining the suction region are shown in Figure 1.9.

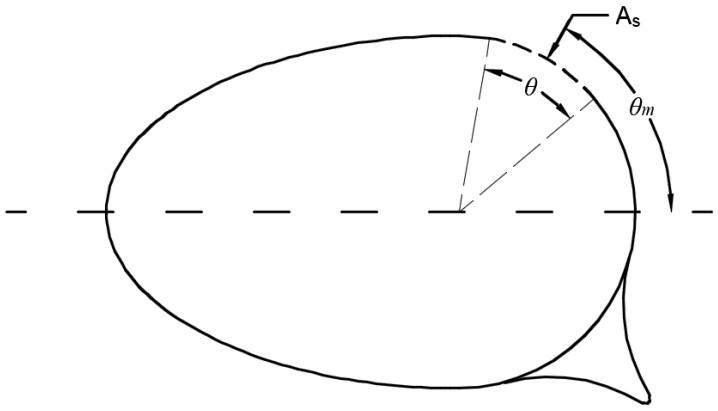

Figure 1.9: Turbosail suction region parameters

The permeability (κ) of the suction area is defined by the ratio between the open area and the total suction area as shown in Equation 1.12.

$$\kappa = \frac{A_o}{A_s} \tag{1.12}$$

The shape and size of the suction holes will influence the flow and the suction efficiency. The existing VentiFoil concepts all feature small round/elliptic holes or open slots used in experimental setups. As stated in [5], it has been shown that small holes provide a good approximation to continuous suction. The size of the holes for suction control is limited such that the holes and the porosity should be small enough not to critically affect the structural integrity of the VentiFoil. The size of the holes should be large enough such that the holes will not get clogged up with sea salt as experienced during the experiments of J. Cousteau and partners. The size of the holes should be small such that the resistance over the holes is large compared to the chamber resistance. This ensures the pressure is more gradually distributed over the perforated surface when small holes are applied. Small holes will require a larger pressure difference in order to provide the same suction. This is because the flux through many small holes is smaller compared to the flux through a few larger holes for the same pressure difference. Therefore, in order to obtain gradually distributed suction, a larger suction pressure is required. The flux through round holes is smallest because the edge length is short

compared to the surface area. Therefore the resistance over round holes is lowest and the required power to obtain a certain suction flux will be smallest for round holes. Another reason for selecting round holes is for easy manufacturing and expansion of the hole size by drilling.

1.8.1 Suction measurements

In order to get an estimate for the provided suction, tests on the half scale model are done by measuring the exhausted volume flux. This is done by measuring the average exhaust velocity at the fan and the diameter of the fan. The exhaust velocity is measured when the VentiFoil was not upright and operating, therefore this measurement provides a rough estimate of the suction range which can be achieved with the mobile half scale VentiFoil. The open area of the suction holes (A_o) is known, therefore the suction flux at the exhaust is evaluated. This flux is the same as the flux through all suction holes. The far field velocity is measured over a period of about 10 minutes. These measurements provide enough information in order to evaluate the suction coefficient to be in the range of $C_q \approx 0.04$. The upright half scale model on which the measurements were conducted is shown in Figure 1.10.

Figure 1.10: Measurements on the VentiFoil half scale model

1.9 Section profile shape

To prevent separation, a profile with smooth and small curvature is required to provide a smooth pressure distribution (C_p) along the leeward surface. A smooth profile shape is defined in [11] as a bluff body consisting of an ellipse at the leading edge and a circle at the trailling edge. The thickness ratio of this profile is $\frac{t}{c} = 0.67$. The pressure is gradually distributed over the suction side of the profile as shown in Figure 1.11. Therefore

this shape is good at preventing separation.

$$C_p = \frac{p - p_\infty}{\frac{1}{2}\rho_\infty U_a^2} \tag{1.13}$$

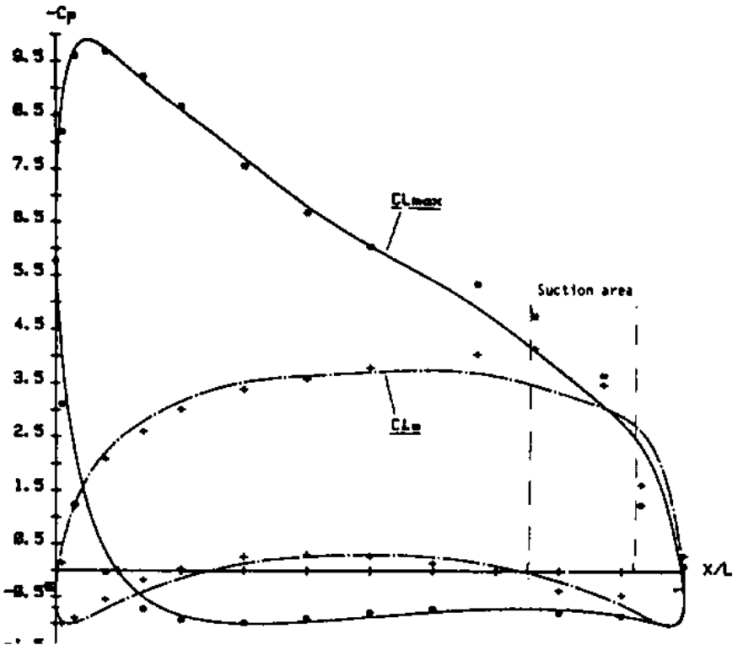

Figure 1.11: Distribution of pressure coefficients on the turbosail profile of the Alcyone - Comparison between theoretical calculations and measurements for C_{Lmax} and C_L at zero angle of attack [1]

The shape of the trailling edge is circular such that the flap can rotate to adjust the shape to the wind conditions when tacking.
The elliptical shape along the leading edge is sensible because it satisfies both conditions of a smooth leading edge and a continuous first derivative at the connection with the circle at the trailling edge.

The study of [4] investigates the effect of the thickness ratio. This study concluded that thicker profiles (larger $\frac{t}{c}$) provide more lift at large angles of attack, however the drag also increases for thicker profiles.

1.10 Container limitation

The dimensions of the VentiFoils inside the eConowind unit are limited by the inner container dimensions. Whereby tolerances between the VentiFoils and the sides of the container should also be accounted for. The container dimensions limit the span (s), the maximum thickness (t) and the chord length (c). The VentiFoil profile thickness is limiting when trying to fit the VentiFoil of thickness ratio $\frac{t}{c} = 0.67$ as used by [11] inside a container. The width limitation can be resolved by tapering the profile over the span. This reduces the area of the turbosails (A) and therefore reduces the thrust provided by the Ventifoil unit. This has a significant influence on the provided thrust by a VentiFoil, because the thrust is assumed linearly proportional with the surface area for the same lift coefficient as shown in Equation 1.14.

$$F_T = \frac{1}{2} C_T \rho U_a^2 A \tag{1.14}$$

In order for the VentiFoil to provide maximum thrust, the balance between an efficient profile shape and the total area of the profile shape is optimized as described in subsection 4.5.4. A schematic representation of different configurations fitted inside a container are shown in Appendix A.

1.10.1 Flap

The Flap is located near the trailing edge of the VentiFoil profile. This flap is used to seal the suction holes on the windward side and to ensure flow separation behind the VentiFoil. To ensure separation, the curvature at the edge of the flap must be large. Due to the separation, a turbulent wake will form behind the VentiFoil. This wake will consist of relatively high pressure as illustrated in Figure 1.12.

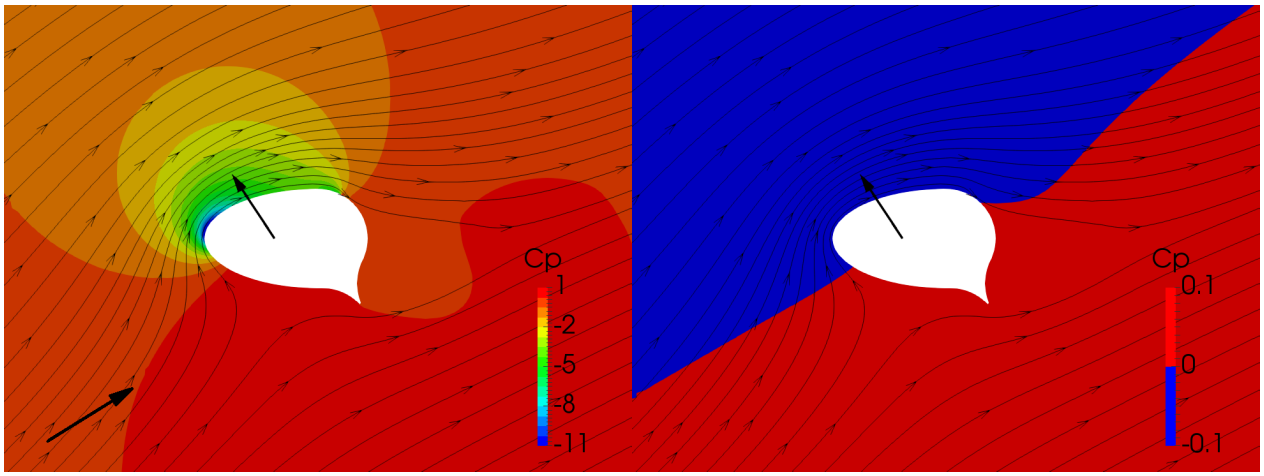

Figure 1.12: Pressure distribution a VentiFoil at $\alpha = 32[°]$ and $C_q = -320[Pa]$

The influence of the position of the flap is investigated by [6]. This study concluded that the location of the flap has a less significant influence on the VentiFoil performance compared to the suction area. However it is still an important parameter to consider. The flap parameters available in literature are given by Table 1.2.

Table 1.2: Flap parameters obtained from literature

Source	Test method	t/c	β	L_F
[4]	CFD, potential	0.5-0.7	0-35	-
[3]	CFD	0.67	40	*0.18c*
[13]	CFD, URANS	0.66	*46*	*0.3c*
[12]	CFD	*0.67*	*45*	*0.31c*
[17]	Model test	1	-	0.42c
[6]	Model test	1	10-100	0.3c

1.11 Base geometry

At the time this report is written, one VentiFoil mounted on a trailer and a full scale eConowind unit have been built. The VentiFoil mounted on the trailer is a half scale test model with a span of 5.5[m] without tapering. This model is used as a test setup on which the resulting forces can be measured. The geometry of this test model will be referred to as the half scale geometry. The first full scale eConowind unit features two full scale VentiFoils with constant taper. The shape of these full scale VentiFoils will be referred to as the base geometry.

Table 1.3: Shape parameters from the built VentiFoils at mid-span

	Half scale geometry	Base geometry	Unit
s	5.5	10.25	m
c_{top}	0.997	1.372	m
c_{bottom}	0.997	1.887	m
t/c	0.646	0.609	-
L_F/c	0.173	0.145	-
β	50	52	°
θ	20.2	14	°
θ_m	67.4	68.8	°

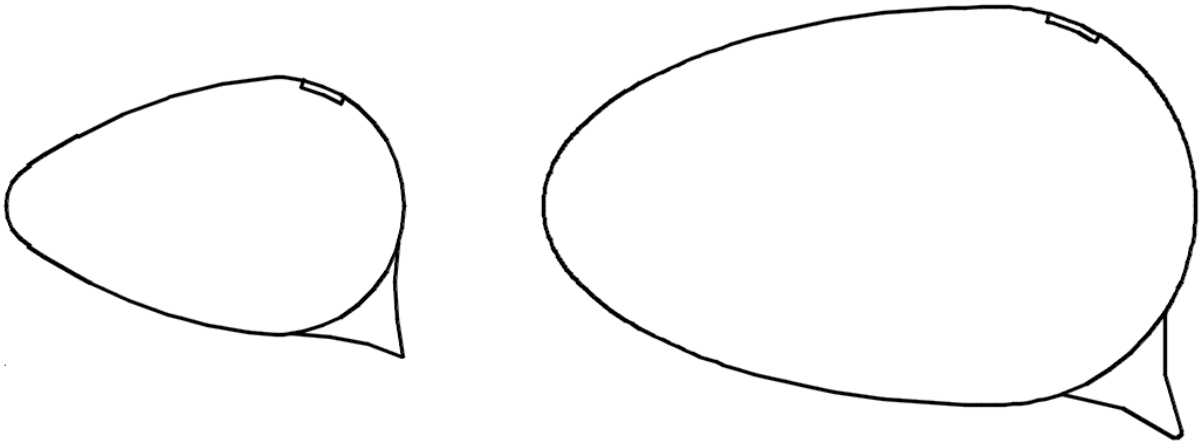

Figure 1.13: Left: half scale geometry, Right: base geometry

Chapter 2

Wind conditions

The performance of the Ventifoil unit depends on the wind conditions over the VentiFoil. The magnitude of the apparent wind (U_a) and the angle of attack (α) affect the produced forces. The thrust component of the produced forces is also influenced by the apparent wind angle (β_a). This chapter will investigate the wind conditions in which the VentiFoils will be operating.

2.1 Angle of attack

The angle of attack is an important parameter with respect to the produced lift and drag and therefore also with respect to the produced thrust. The optimum angle of attack is different for different apparent wind angles as illustrated in the polar diagram of Figure 2.1. This figure also illustrates that for most apparent wind angles the optimum angle of attack varies only slightly. The angle of attack can be tuned by rotating the VentiFoils such that maximum thrust is obtained.

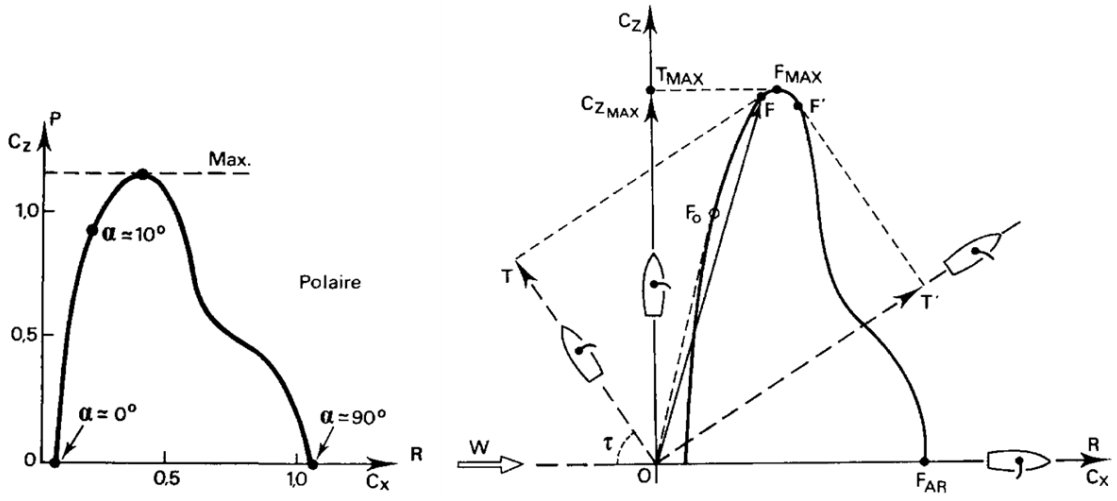

Figure 2.1: Polar diagrams for lift and drag coefficients at different angles of attack, obtained from [11]

The angle of attack is limited by the stalling behaviour of the Ventifoil. The produced forces generally increase when the angle of attack is increased provided that the applied suction is sufficient to prevent the VentiFoil from stalling.

The thrust obtained when sailing downwind is not favorable because in this condition, the thrust is per definition produced by the drag force. The drag force cannot be significantly increased by increasing the angle of attack because stall will occur and the drag force will not be significant because the characteristic

area of the VentiFoil is relatively small. Because the VentiFoil is excellent in the production of, the side force when sailing downwind is significant.

2.2 Apparent wind

The apparent wind is the wind the ship encounters. And therefore the apparent wind determines the operating conditions of a VentiFoil. The apparent wind speed and direction differ from the true wind speed due to the forward speed of the ship. This is illustrated in Figure 2.2 The magnitude of the apparent wind speed is obtained from the true wind speed and the ship speed as stated in Equation 2.1.

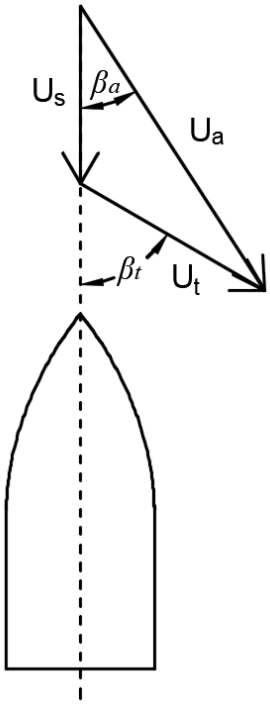

Figure 2.2: Wind directions

$$U_a = \sqrt{(U_s + U_t cos(\beta_t))^2 + (U_t sin(\beta_t))^2} \tag{2.1}$$

The apparent wind angle differs from the true wind angle due to the forward velocity of the ship. The forward velocity of the ship will decrease the apparent wind angle except for stern and head wind conditions. The apparent wind angle can be obtained from Equation 2.2.

$$\beta_a = tan^{-1}\left(\frac{U_t sin(\beta_t)}{U_s + U_t cos(\beta_t)}\right) \tag{2.2}$$

The suction coefficient C_q is assumed to provide a good parameter to characterize the required suction at different apparent wind speeds as often used in literature. This might not exactly be the case because the turbulence regime changes depending on the velocity. Therefore the optimization should be conducted for appropriate wind conditions and geometric scales.

The apparent wind angle for which positive thrust can be obtained ($\beta_{a,max}$) depends on the C_L/C_D ratio.

This angle can be evaluated by Equation 2.3.

$$\beta_{a,max} = tan^{-1}\left(\frac{C_D}{C_L}\right) \tag{2.3}$$

2.3 Wind conditions

The wind conditions which the ship will encounter influence the flow and separation behaviour of the Ventifoil. This wind speed is evaluated using statistic wind data for the North Sea and the Baltic Sea at the above sea (blue) locations as shown in Figure 2.3 and Figure 2.4 obtained from European Centre for Medium-Range Weather Forecasts (ECMWF).

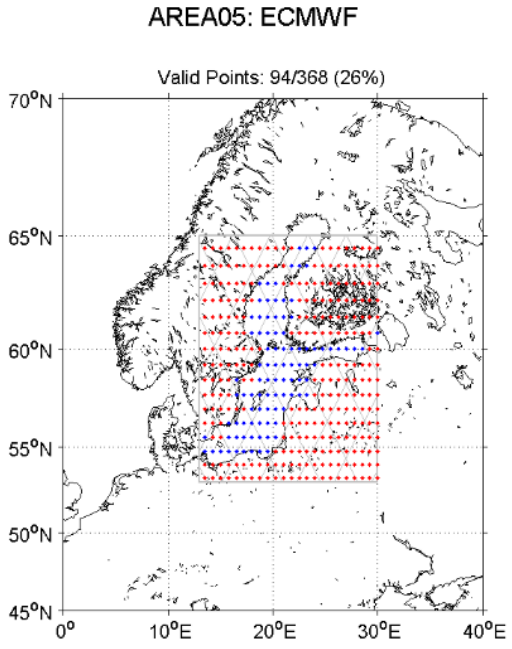

Figure 2.3: Baltic Sea data grid

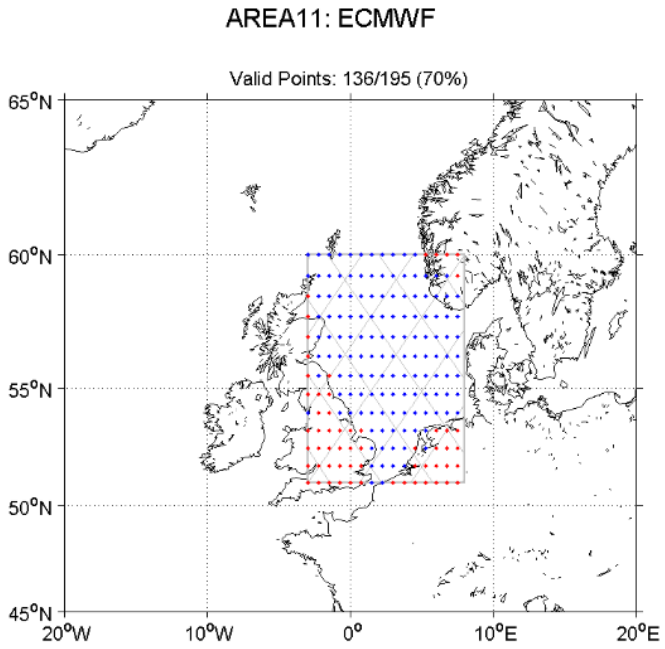

Figure 2.4: North Sea data grid

The Weibull distribution provides a good fit for wind data as used in [8] and shown in Figure 2.5 for wind data from the North Sea and Baltic Sea.

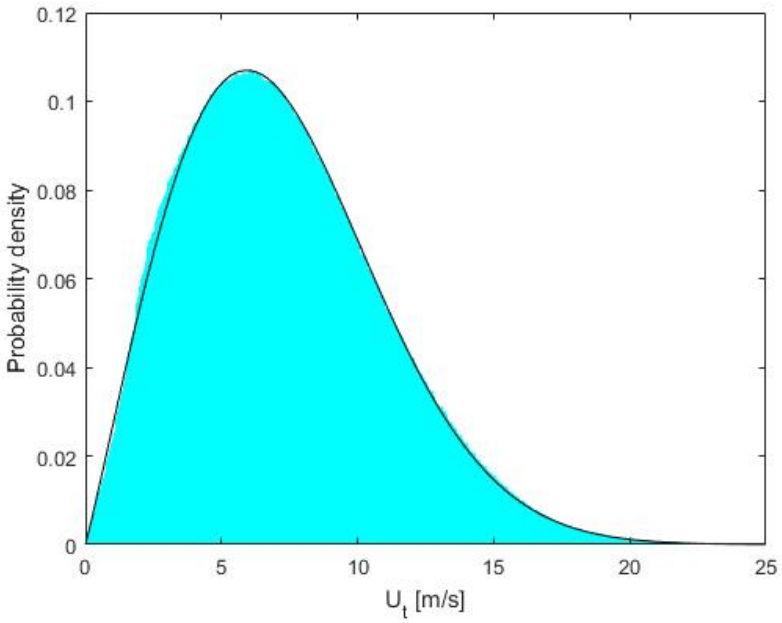

Figure 2.5: Probability distribution of the true wind velocity on the Baltic and North Sea, including a Weibull distribution with parameters $\lambda_w = 8.178$ and $k_w = 2.061$

The probability of the encountered true wind angle with respect to the heading of the ship is assumed to be uniformly distributed. This is an assumption which is made because the true wind angle on a large area is considered and because not one particular ship or one particular shipping route is considered. Only one side (from 0 to 180°) is considered because the apparent wind angle is symmetric.

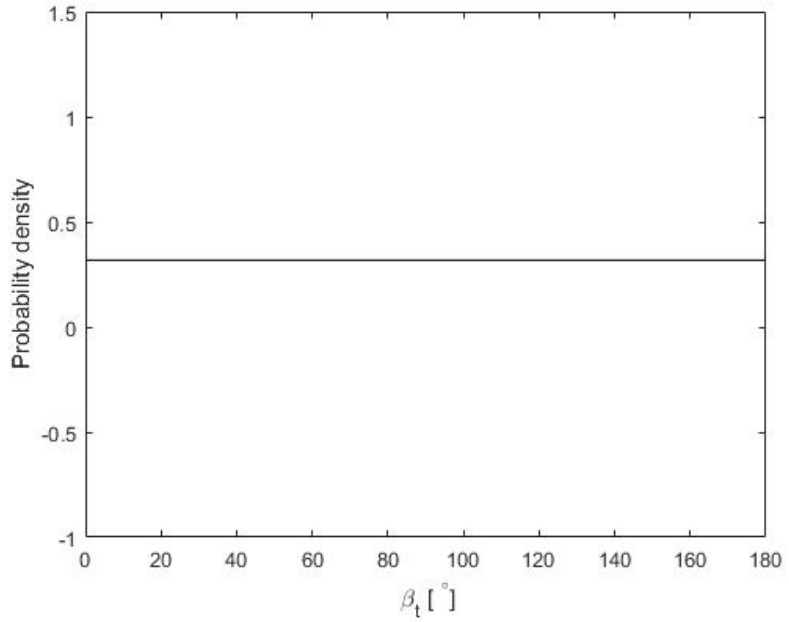

Figure 2.6: Probability true wind direction with respect to the heading of the ship

From these distributions, the Apparent wind speed and apparent wind angle are evaluated for a ship sailing $U_s = 5.67[m/s] \widehat{=} 11[kn]$. In order to obtain maximum performance from the Ventifoil, the optimization should

be conducted for energetic and frequently occurring true wind speeds such that the Ventifoil is optimized for the conditions where most of the energy can be extracted during long term operation. The mean of the energy density spectrum provides a good parameter to evaluate the wind speed at which most energy can be extracted. Because $P_w \propto {U_s}^3$, the mean wind velocity of the energy density spectrum is evaluated from Equation 2.4.

$$U_{a,max(P_w)} = \overline{U_a^3}^{1/3} \tag{2.4}$$

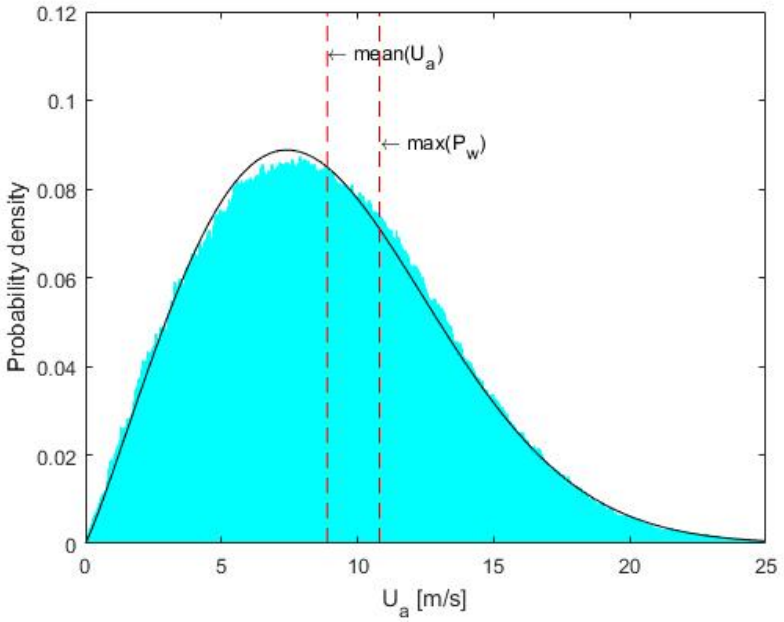

Figure 2.7: Probability distribution of the apparent wind speed on the Baltic and North Sea for $U_s = 11[kn]$, including a Weibull fit with parameters $\lambda_w = 10.00$ and $k_w = 2.096$

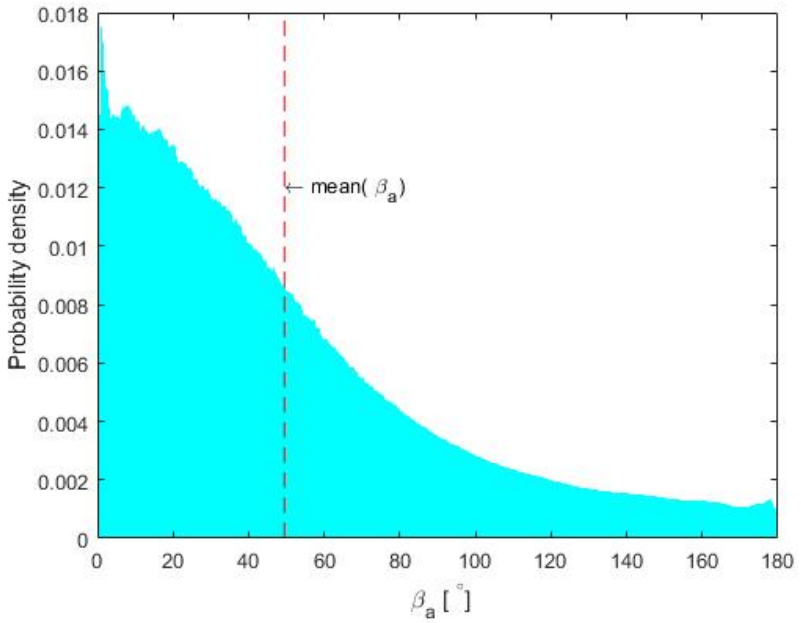

Figure 2.8: Probability distribution of the apparent wind direction on the Baltic and North Sea for $U_s = 11[kn]$

Based on these wind conditions, the mean wind speed for the wind energy is $U_a = 10.8[m/s]$. The mean apparent wind angle used to translate lift and drag into thrust and side force is $\beta_a = 50[°]$.

2.4 Vertical wind profile

Due to the boundary layer along the sea surface, the true wind velocity varies over the height above the sea surface. This is known as wind shear. Because the VentiFoil profiles are mounted vertically, the vertical differences in wind velocity influences the inflow conditions over the span of the VentiFoil. The increasing true wind velocity over the height generally means that the apparent wind velocity and the apparent wind angle both increase towards the top of the VentiFoil. Therefore the wind conditions are generally more favorable at the height of the top of the VentiFoil compared to the bottom.

The vertical wind profile can be approximated using the power law with exponent $P = 0.11$ as obtained from [15] and shown in Equation 2.5. The reference height is usually $10[m]$ above mean sea level.

$$U_t(z) = U_t(10)\left(\frac{z}{10}\right)^P \tag{2.5}$$

The bottom of the VentiFoil is located approximately $10[m]$ above the waterline. Therefore the top will be located approximately $20[m]$ above the waterline. An approximation for the difference in true wind speed can therefore be expressed as Equation 2.6.

$$\left(\frac{U_{t,top}}{U_{t,bottom}}\right)^P = 1.08 \tag{2.6}$$

Roll and pitch motions of the ship can have an influence on the vertical wind profile because the top of the VentiFoils extends far above the center of flotation. For this study, the ship motions are assumed small because the VentiFoil will be retracted in heavy sea states. Therefore the influence of ship motions on wind speed is neglected.

2.5 Surrounding structure and exhaust

The flow over the Ventifoil is influenced by the surrounding structure such as the ship and the container of the Ventifoil unit. The presence of the ship causes the flow to accelerate above the deck for beam wind as shown in Figure 2.9. There is no significant variation in normalized wind speed for beam wind directions $\pm 30°$ as explained in [2]. This effect contradicts the velocity profile due to wind shear. Therefore the varying velocity profile over the height is assumed small and is neglected.

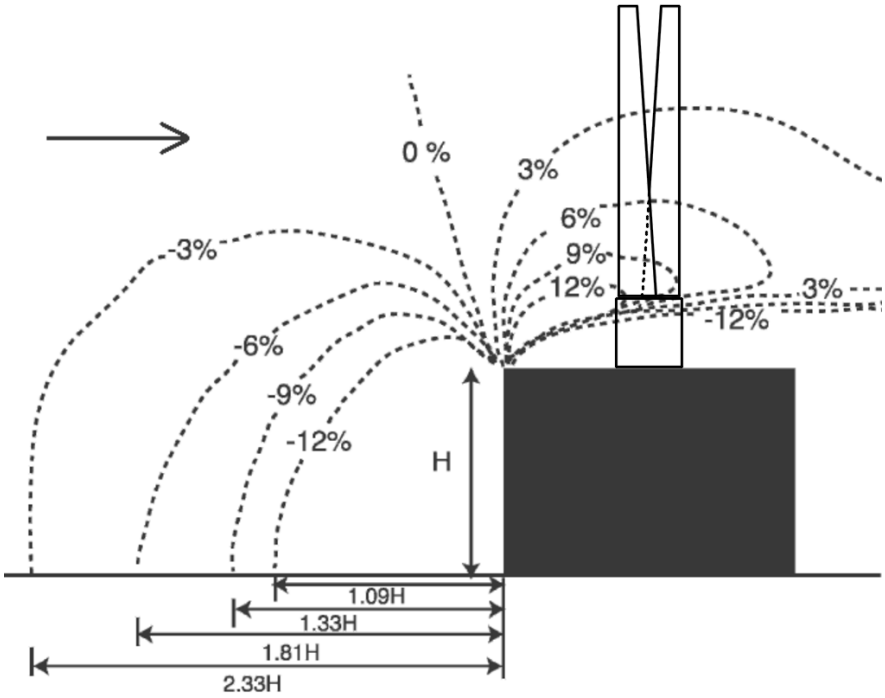

Figure 2.9: Flow velocity distortion in front of the block for beam-on flow, obtained from [2] and adapted to include the eConowind unit

The Ventifoil units should not be placed directly in front of the bridge as the bridge will disturb the flow at this location. A re-circulation region or a wake are formed which both result in smaller wind velocities just in front of the bridge.

The exhaust of the fan which provides the suction disrupts the wind flow at the bottom of the VentiFoil just above the container. The influence and the significance of the disruption of the flow due to these effects is limited because just above the deck, and just above the container there is a low velocity region. Therefore this region does not provide much thrust and the influence of the exhaust flow on the Ventifoil performance is less significant.

Chapter 3

Computational fluid dynamics

CFD is a numeric method to solve fluid flow problems. This project uses CFD analyses to analyze the flow around VentiFoils. CFD uses an iterative computational process to evaluate the flow according to the governing equations. The advantage of using CFD analyses is that the flow properties can be evaluated and visualized in every point of the computational domain. This chapter explains the essential parts of the used CFD analyses.

3.1 Parameters and dimensionless numbers

The CFD simulations are made for full scale and half scale VentiFoils. The half scale simulations are made in order to validate the CFD simulations based on the measurement data from the tests of the half scale model.

The wind speed (U_a) for all computations is set at 10[m/s]. This is a reasonable encountered wind speed for as shown in Figure 2.7. This results in Reynolds numbers in the order of $1E6$. Therefore the flows are turbulent and significantly inertia dominated.

This wind speed results in a Mach number as shown in Equation 3.1. Because the Mach number is smaller than 0.25, the flow can be modeled as incompressible and isothermal.

$$Ma = \frac{U_a}{c_{air}} = \frac{10[m/s]}{343[m/s]} = 0.0292 \tag{3.1}$$

3.2 Physical modeling

The physics which describe flow behaviour is governed by the conservation of mass and the conservation of momentum. Both these conservation laws are captured in the Navier-Stokes equations.

3.2.1 Conservation of mass

The mass in the system remains constant because the mass entering the domain through the inflow is the same as the mass exiting the domain through the outflows at the outer edges of the domain and at the suction region. This is also true for the grid cells. Therefore no mass is added or removed. This conservation of mass is described by the continuity equation. This equation is shown in differential form in Equation 3.2.

$$\frac{\partial \rho}{\partial t} + \nabla \cdot \rho \mathbf{u} = 0 \tag{3.2}$$

Because the Mach number is significantly smaller than 0.25, the flow can be modeled as incompressible. For an incompressible flow the continuity equation becomes Equation 3.3.

$$\nabla \cdot \mathbf{u} = 0 \tag{3.3}$$

3.2.2 Conservation of momentum

Momentum can only be changed by forces acting on the fluid. Therefore the conservation of momentum describes a force balance. Momentum is conserved in all three Cartesian directions. The momentum in the flow is conserved for the entire domain as well as for the grid cells. This is described by [7]. Equation 3.4 describes the conservation of momentum in differential form which is satisfied when momentum is conserved. The first term in this equation represents forces due to acceleration of the flow. The second term represents forces due to convection of momentum. The third term represents the forces due to pressure. The fourth term represents the viscous forces. The total of these terms equals the body forces. For the simulations in this study, no body forces are considered. When these forces are balanced, momentum is conserved.

$$\frac{\partial u_j}{\partial t} + u_i \frac{\partial u_j}{\partial x_i} + \frac{1}{\rho}\frac{\partial p}{\partial x_j} - \frac{1}{\rho}\frac{\partial \tau_{ij}}{\partial x_i} = f_i \tag{3.4}$$

3.2.3 Boundary conditions

The boundary conditions determine the flow inside the computational domain. Therefore the boundary conditions should be applied such that the physical flow is modeled correctly.

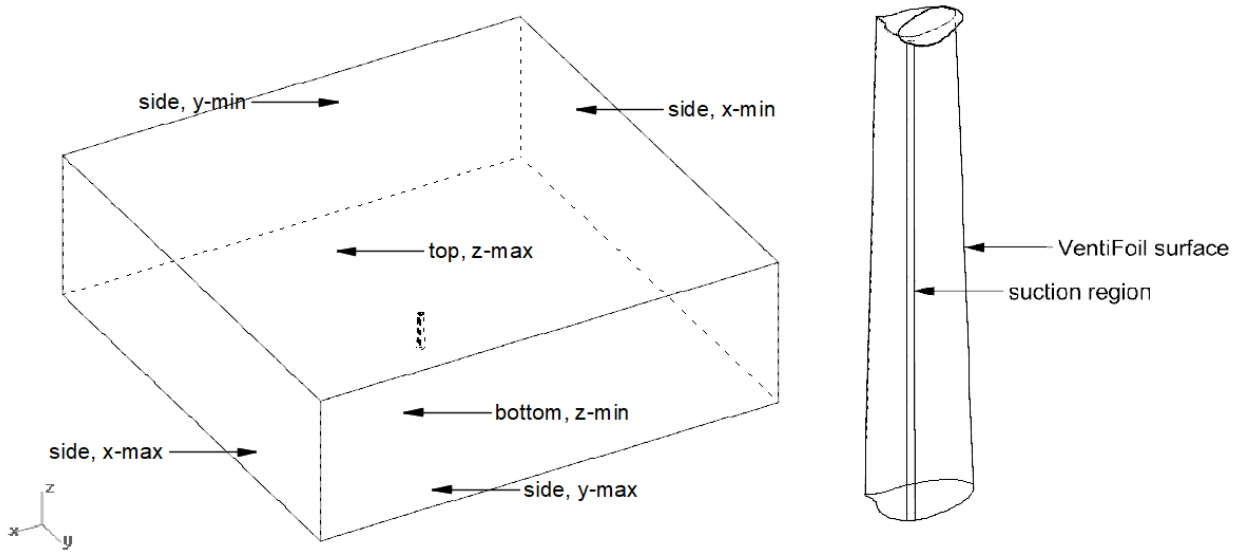

Figure 3.1: Boundary conditions

The reference pressure in the domain is 0 [Pa], Therefore the evaluated pressures represent the dynamic pressure.

Domain sides

The boundary conditions at the sides of the domain determine the far field wind conditions. The boundary condition "autodetect" from Refresco is used for these boundaries. This boundary condition uses either the

specified far field velocity or the reference pressure depending on the location of the boundary. Because the flow is not perpendicular or parallel to the sides of the domain, the autodetect boundary condition is used to determine the location of the pressure and the velocity conditions.

Domain bottom

The bottom of the domain is modeled as a symmetry boundary condition such that there is no friction at this surface ans no flow through this surface.

Domain top

When the flow is modeled as a slice and for 2D simulations, the top boundary condition is modeled as a symmetry plane and therefore the same as at the bottom of the domain. For 3D simulations the top boundary condition is set sufficiently far above the VentiFoil in order not to significantly influence the flow over the VentiFoil. Therefore top boundary condition is a far field condition. The reference pressure of 0[Pa] is specified at this domain boundary.

Plate surface

The surface boundary condition on the plate surface of the VentiFoil is specified as a no-slip condition. This means that there is no flow through or along the plate surface. This boundary condition results in a boundary layer and viscous forces acting on the surface.

Suction boundary condition

The suction boundary is modeled using a pressure boundary condition whereby a negative dynamic pressure is applied to the surface. This low pressure causes the flow to exit the domain through the suction surface as shown in Figure 3.2.

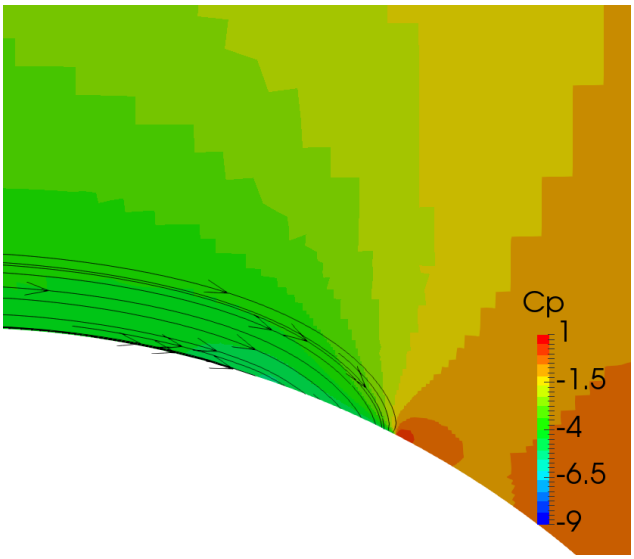

Figure 3.2: Outflow at the suction region

In order to reduce the required computational effort, the suction boundary condition is modeled as a surface which extends over the span of the VentiFoil, this will be referred to as a slot. In order to evaluate the accuracy of this modeling method, the results for a slot are compared to simulations whereby round holes with a pressure condition are used for the suction boundary. In order to reduce the computational effort of

modeling the holes, this comparison is made for a model of a slice with a span of 0.25[m]. Holes with a radius of 0.01[m] and 0.005[m] are compared in order to evaluate the effect of a different hole size. The permeability of the suction surface is constant at $\kappa = 0.4$. The distance between the holes is determined according to Equation 3.5.

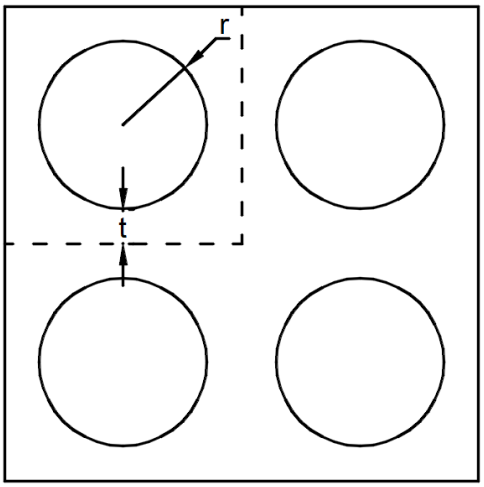

Figure 3.3: Holes distribution

$$t = \frac{1}{2}\left(\frac{\sqrt{\pi}}{\sqrt{\kappa}} - 2\right) r \tag{3.5}$$

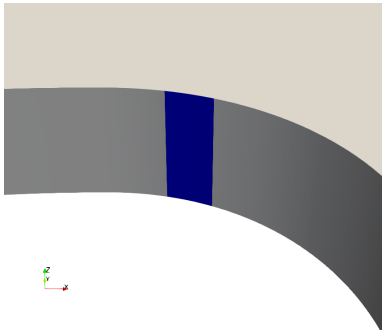

Figure 3.4: Slot

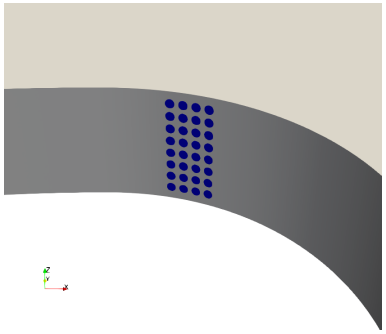

Figure 3.5: Holes $r = 0.01[m]$

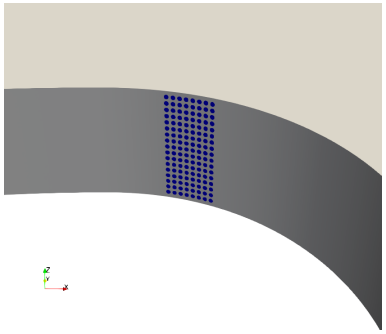

Figure 3.6: Holes $r = 0.005[m]$

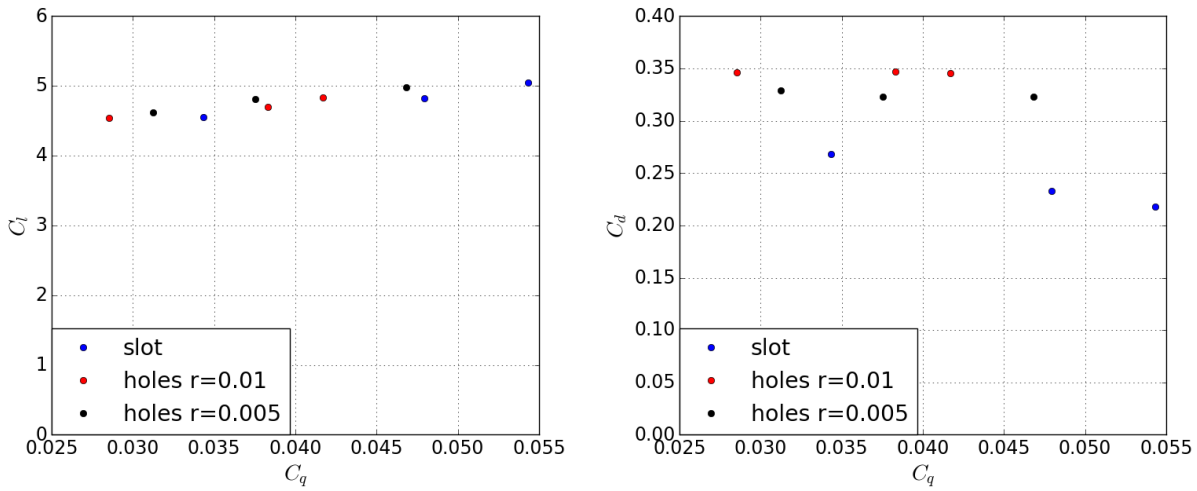

Figure 3.7: Lift and drag coefficient for different suction boundary conditions

The geometries with holes also have a higher pressure region behind the suction holes, however this high pressure region is less pronounced for the holes when comparing to the slot. The pressure is even more smoothly distributed for smaller holes.

Suction regions with holes result in larger drag coefficients as shown in Figure 3.7. This is because the low pressure on the suction holes also reduces the pressure on the surface between the holes. Because this surface is approximately perpendicular to the far field flow direction, the pressure on this surface has a large influence on the drag force and results in a larger drag coefficient because the pressure on this surface is low.

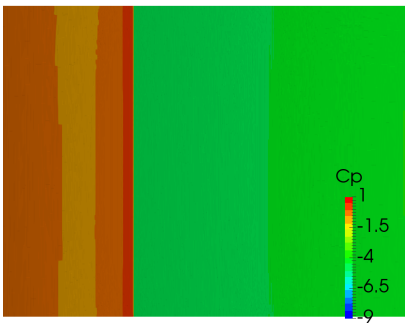

Figure 3.8: Slot

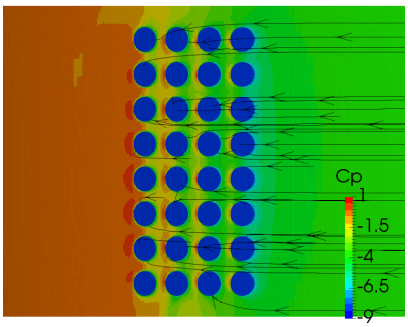

Figure 3.9: Holes $r = 0.01[m]$

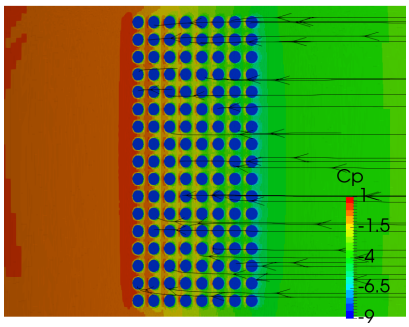

Figure 3.10: Holes $r = 0.005[m]$

3.2.4 Separation

The separation location for a VentiFoil type profile is well defined on the pressure side as well as on the suction side. Flow separation at the tip of the flap is induced because of the large curvature at this location. Flow separation on the suction side will occur just behind the suction region due to the large adverse pressure gradient at this location. Part of the turbulent flow is removed from the boundary layer at the suction location as shown in Figure 3.11.

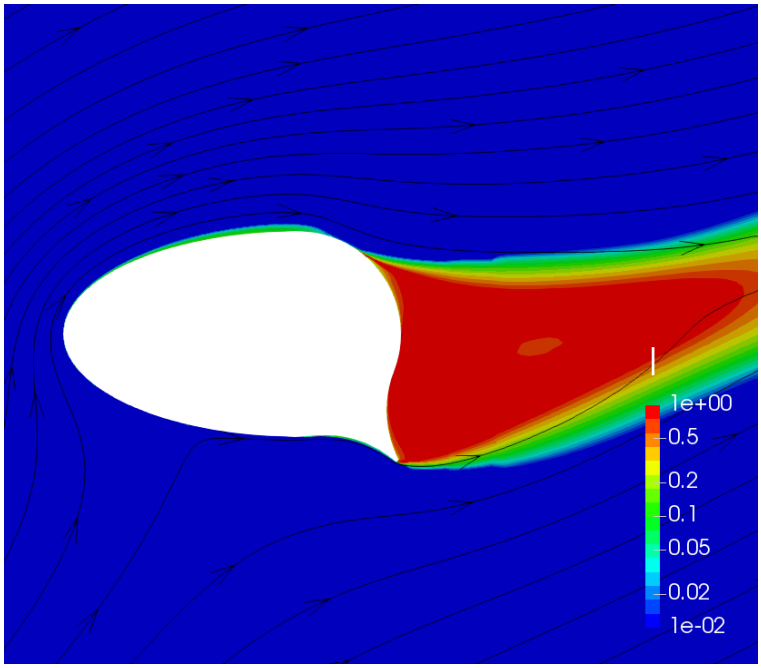

Figure 3.11: Turbulence intensity

3.2.5 Unsteady simulation

Because the Ventifoil has a bluff body shape with a turbulent wake behind the VentiFoil, the forces on the VentiFoil might be unsteady. The unsteady flow is studied by [9] using 2D Unsteady Reynolds Averaged Navier-Stokes (URANS) simulations. This study concluded that the difference in generated lift is small for unsteady simulations and the difference for drag is slightly increased for unsteady simulations due to pressure fluctuations in the wake which cause a lower average pressure in the wake.

The far field velocity is simulated as steady in magnitude as well as direction. This is not the case on sea because there are velocity variations in the form of gusts and periodic directional variations. Therefore the flow is quasi static. The suction should be sufficient in order to prevent stall when there are small changes of the wind conditions. Because the applied suction and angle of attack can be changed when the wind conditions are changing, the effect of unsteady inflow is assumed to be small and is neglected.

3.3 Mathematical modeling

Some complex flow features are not resolved. These features cannot be neglected, therefore these are modeled in order to provide an approximation for these effects.

3.3.1 RANS

The flow is modeled using Reynolds Averaged Navier-Stokes (RANS) simulation whereby the mean flow is resolved, resulting in a steady flow solution. Due to the averaging of the velocities, a term of two fluctuating velocities which cannot be resolved appears in the Navier-Stokes equation. This term is called the Reynolds stress tensor. In order to resolve this term, turbulence modeling is used.

3.3.2 Turbulence modeling

Turbulence is modeled because the grid refinement is not sufficient in order to capture all turbulence scales and because the flow is solved using RANS simulations which does not capture velocity fluctuations as found in turbulent flows. Therefore turbulence modeling is used to approximate the effects of turbulence. The applied turbulence model is the Shear Stress Transport (SST) k-ω model from Menter (2003). This turbulence model was investigated by [9] and found to be suitable.

3.4 Numerical modeling

3.4.1 Spacial discretization

In order to solve the governing equations, the domain is discretized to provide control volumes for which the equations can be solved. The domain is discretized using the grid generation program Hexpress. This program is used to generate unstructured hexahedral grids around the VentiFoils. The use of Hexpress allows for the generation of many grids with similar settings for a series of different geometries.

3.4.2 Boundary layer refinement

The boundary layer is resolved rather than modeled in order to correctly capture the separation behaviour. To resolve the boundary layer, the grid refinement at no-slip surfaces is refined such that $y^+ < 1$. This is common practice at MARIN to ensure the viscous sublayer law of $u^+ = y^+$ can be used. As shown in Figure 3.12, the global maximum value for y^+ is located just behind the suction region with a value of 0.8. This is a small region with a large y^+.

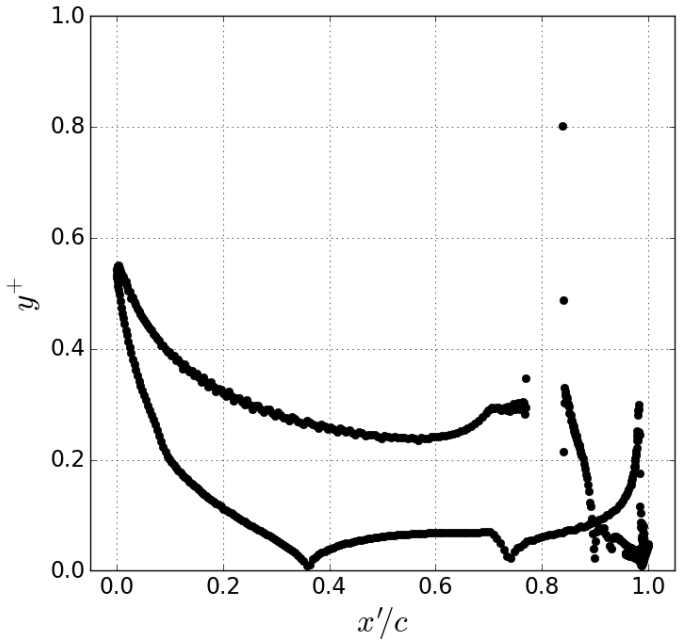

Figure 3.12: y^+ for the 2D base geometry with $\alpha = 30[°]$ and $p_s = -300[Pa]$

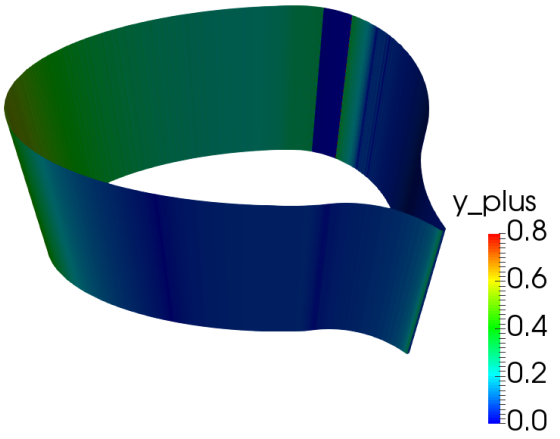

Figure 3.13: y^+ plotted on the 2D base geometry with $\alpha = 30[°]$ and $p_s = -300[Pa]$

A local y^+ maximum is found at the suction side of the leading edge. This location is to be expected for a maximum because the velocity at this location is largest with up to 3.4 times larger than the far field reference velocity as shown in Figure 3.14.

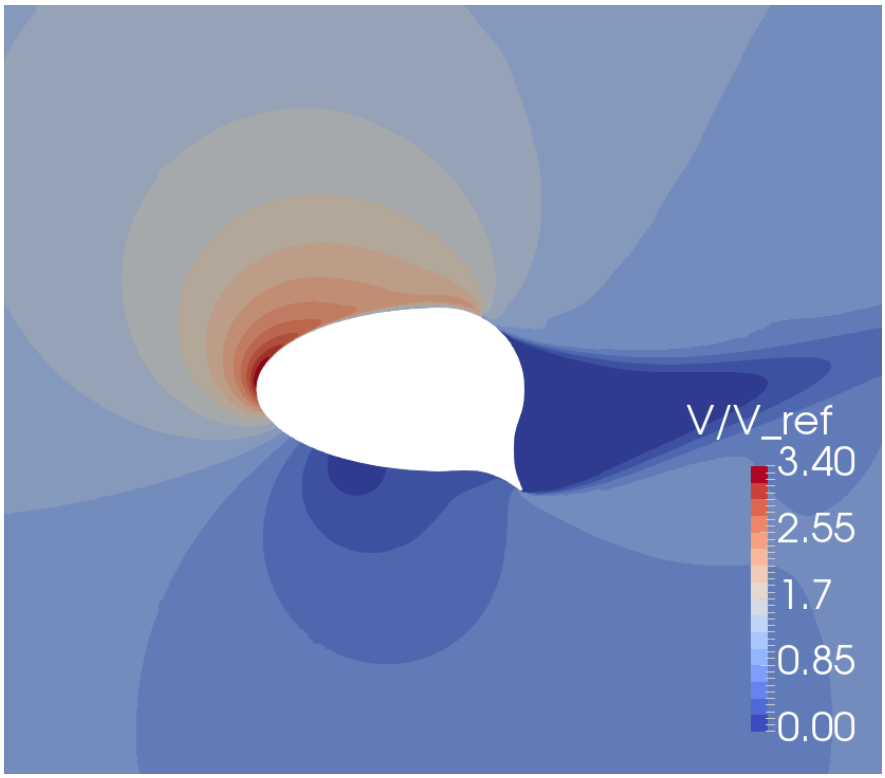

Figure 3.14: Relative velocity profile

3.4.3 Numeric discretization

The Navier-Stokes equations are discretized in order to solve the equations on the grid cells. The convective flux discretization uses a Total Variation Diminishing (TVD) scheme for momentum whereby the Refresco

default Harmonic scheme is used as flux limiter. The convective flux discretization scheme which is used for turbulence is the first order upwind scheme.

3.5 Solver

The discretization leads to a system of linear equations which has to be solved as described by [7] and shown in Equation 3.6 whereby A_{mat} is a large known matrix, φ is the variable which has to be solved and b is a known vector.

$$\underline{\underline{A}} \cdot \underline{\varphi} = \underline{b} \tag{3.6}$$

Because A is large, the inverting of this matrix is computationally expensive. Therefore the Generalized minimal residual method (GMRES) default Refresco solver is used to provide the solution. This method attempts to provide a solution with a minimal residual whereby the residual is defined as the deviation from the solution of the system of linear equations as shown in Equation 3.7.

$$\underline{R}^n = \underline{\underline{A}} \cdot \underline{\varphi}^n - \underline{b} \tag{3.7}$$

3.5.1 Convergence criteria

The simulations are stopped when the forces are stable and the solution is sufficiently converged as indicated by the residuals. The L_2 residuals for the 2D simulations are at least below 1e-8. The residuals for 3D simulations converge less well however the forces for these residuals are stable. For 3D simulations, only solutions with an L_2 residual lower than 1e-3 are used. The L_∞ residuals are generally 2 orders higher compared to the L2 residuals. This means that the maximum residual in the domain is about two orders of magnitude larger than the root mean square of all the residuals in the domain. The convergence behaviour of the L_2 and L_∞ residuals for 2D and 3D simulations is shown in Figure 3.15.

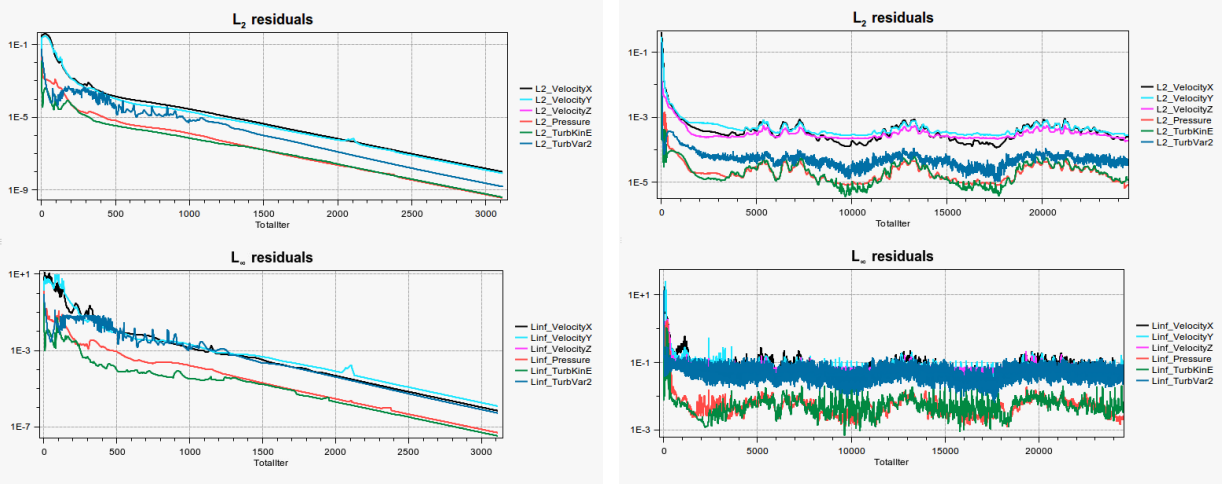

Figure 3.15: Residual convergence of the base geometry, left: 2D, right: 3D

3.6 Uncertainty

The simulated results presented in this report are based om some assumptions. This section will describe most significant assumptions and uncertainties in the results.

3.6.1 Uncertainty in converged results

The converged and non-separated solutions of the CFD simulations are used to evaluate the resulting forces from the VentiFoils. The forces appear steady when the simulations are sufficiently converged. This is shown in Figure 3.16. Because the scale of these forces is not visible in the figures, the unsteadiness of the forces can be expressed by the standard deviation. The relative standard deviation for different forces is shown in Table 3.1. Based on these standard deviations, the solutions are considered sufficiently stable.

Table 3.1: Relative standard deviation for 2D and 3D base geometries

	Iteration range	$\sigma_{F_x} / \lvert F_x \rvert$	$\sigma_{F_y} / \lvert F_y \rvert$
2D	1500-3112	4.62E-5	2.90E-5
3D	5000-27184	8.10E-4	2.47E-4

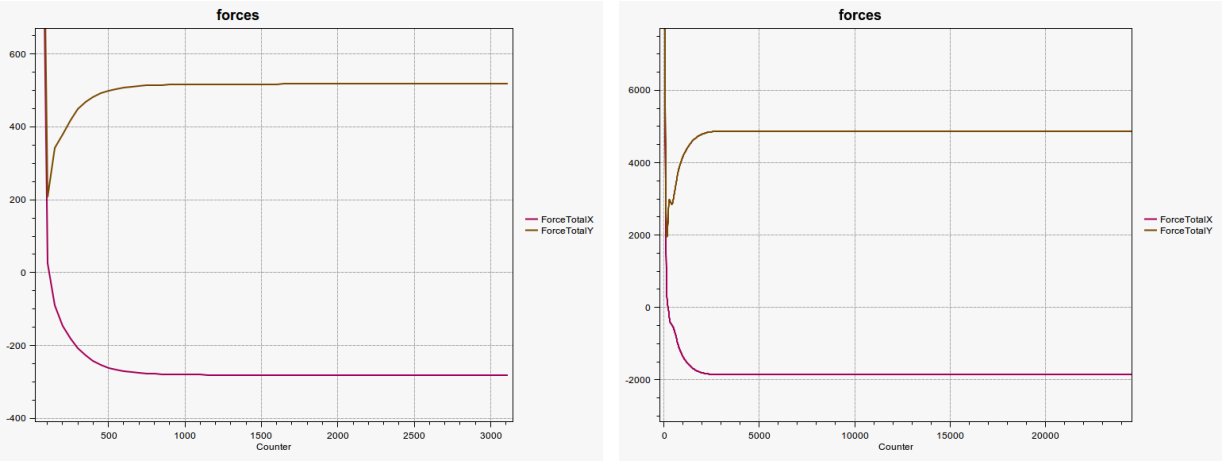

Figure 3.16: Force stabilization of the base geometry, left: 2D, right: 3D

3.6.2 Input assumptions

The, wind direction, wind speed and turbulence intensity of the in flowing wind are assumed constant. In true wind conditions these properties would be due to wind gusts and shifting wind directions. Wind shear and rotation of β_a over the span is also assumed constant as explained in section 2.5.

Chapter 4

2D parametric investigation

The propulsive performance of a VentiFoil is determined by the wind conditions, the applied suction and the shape of the VentiFoil. The shape of the VentiFoil can be described by multiple shape parameters which differently influence the performance of a VentiFoil. When designing a VentiFoil, it is uncertain which section profile should be used and what the influence and sensitivity of different parameters is on the performance of a VentiFoil. This chapter describes the investigation of the influence of characteristic shape parameters on the performance of a VentiFoil using steady 2D CFD simulations.

4.1 Geometry description

The section profile is defined using shape parameters for the shape of the leading edge, the chord length, the thickness ratio, the length of the flap, the thickness of the flap tip, the flap angle, the suction location and the width of the suction region. The Computer Aided Design (CAD) program Rhino combined with the Grasshopper plugin and a Python script is used to generate multiple different systematic series of geometries whereby one section shape parameter is varied. Some shapes of the section profile such as the circular trailing edge and the curvature of the flap are fixed.

The section parameters of the specific geometries are specified using the code as shown in Figure 4.1 whereby each number refers to a parameter setting. The section variations are conducted around a base geometry with parameters as shown in this figure. All geometries have a chord length of 1.63[m] as specified by the midsection of the base geometry in Table 1.3. Therefore the characteristic area (A) of all profiles is the same. The thickness of the tip of the flap is also kept constant at $t_{tip}/c = 0.0128$ which approximately corresponds to a thickness of 2[cm].

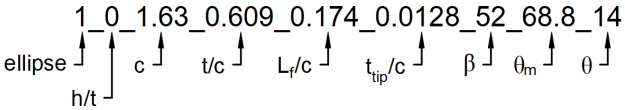

Figure 4.1: Shape parameters of the 2D base geometry

4.1.1 Leading edge

The leading edge is described by [1] as an ellipse. To perform a shape variation of the leading edge, two cubic (3^{rd} order) Bezier curves with equally weighted points are used to describe the leading edge. Because the section is line symmetric over the chord axis, two mirrored Bezier curves are used to describe the geometry. The setting whether a Bezier curve or an ellipse is used is determined by the first shape parameter from Figure 4.1. When an ellipse is used, the first value is 1. When a Bezier curve is used, the first value is 0 and the second value (h/t) determines the shape. The Bezier curve is constructed based on two conditions:

1. The leading edge must be rounded, therefore the bottom and top leading edge curves must be tangential.
2. The curvature at the connection to the circular trailling edge must be continuous.

Condition 1 is per definition satisfied by an ellipse. For a Bezier curve this means that the first control point should be located above the leading edge.

Condition 2 can per definition not be satisfied for an ellipse unless for a circular leading edge (c=t). For a Bezier curve, this condition can be met by setting the same curvature at the connection point between the Bezier curve and the circular trailling edge. Equation 4.1 as obtained from [16] defines the curvature of the Bezier curve at the connection to the circular trailling edge. For a cubic Bezier curve, $n = 3$ for Equation 4.1. This results in the equation as shown in Table 4.1. Condition 2 is satisfied by defining a as described in Equation 4.2. After the implementation of these conditions, there remains one free Bezier curve parameter which is used to define the shape of the leading edge (h/t).

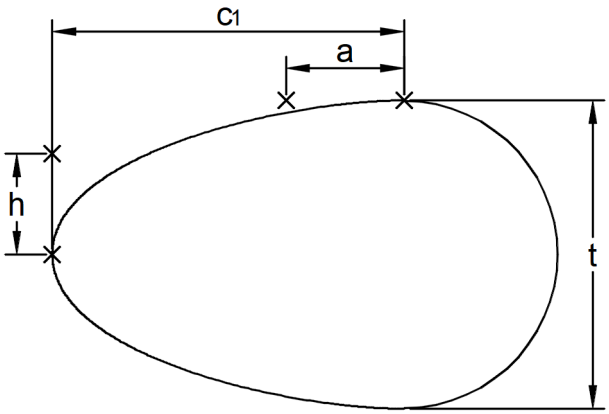

Figure 4.2: Bezier curve parameters, the control point locations are indecated by the crosses

$$k = \frac{n-1}{n} \cdot \frac{h}{a^2} \tag{4.1}$$

Table 4.1: Curvature at connection to the trailling edge

	Bezier curve	Circle	Ellipse
Curvature	$k = \frac{2}{3}\frac{h}{a^2}$	$k = \frac{2}{t}$	$k = \frac{t}{2{c_1}^2}$

$$a = \sqrt{\frac{h}{3t}} \tag{4.2}$$

4.2 2D simulation

The parametric performance investigation is performed using 2D CFD simulations. The advantage of using 2D simulations is that less computational effort is needed in order to provide a flow solution. This allows for the evaluation of multiple section profiles for many different angles of attack and suction pressures. 2D simulations do not capture end effects and therefore tend to overestimate the lift and underestimate the drag.

4.2.1 Geometry

In order to compare the simulations to previous VentiFoil research as described in [9], the same geometry is used for the grid parameter study.

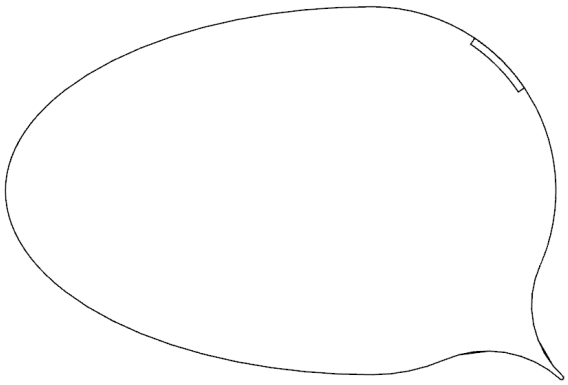

Figure 4.3: Geometry as defined by [9]

4.2.2 Computational Domain

The shape of the computational domain is square because this shape fits well with the hexahedral cells of the Hexpress grids.

The size of the domain can influence the flow solution if the domain boundaries are not sufficiently far away from the VentiFoil. The spanwise domain size does not influence 2D simulations, therefore a unit span of 1[m] is selected for the height of the domain. The domain size in xy-plane does influence the flow and the resulting pressures. Because the cells at the edges of the domain are coarse, increasing the size of the domain has a low impact on the required computational effort. The influence of the domain size is shown in Figure 4.4. This figure shows the relative deviation from the results at the selected value of 1600 times the chord length which is plotted against the extend of the domain. From this figure it can be concluded that a domain which is too small will underestimate the lift and overestimate the drag. A domain size of 1600 times the chord length (c) is selected whereby the deviation for lift is negligible and for drag within 2% of the maximum evaluated domain size of 3200 times the chord length. Therefore this domain size provides solutions close to the asymptotic value. The size of this domain is considered large with respect to the size of the VentiFoil but is needed in order not to significantly influence the resulting forces.

The results of the domain size study are compared to the results from previous research from A. Kisjes [9] whereby round structured grids are used. Figure 4.4 shows that the results are within 0.5% for lift and within 3.3% for drag.

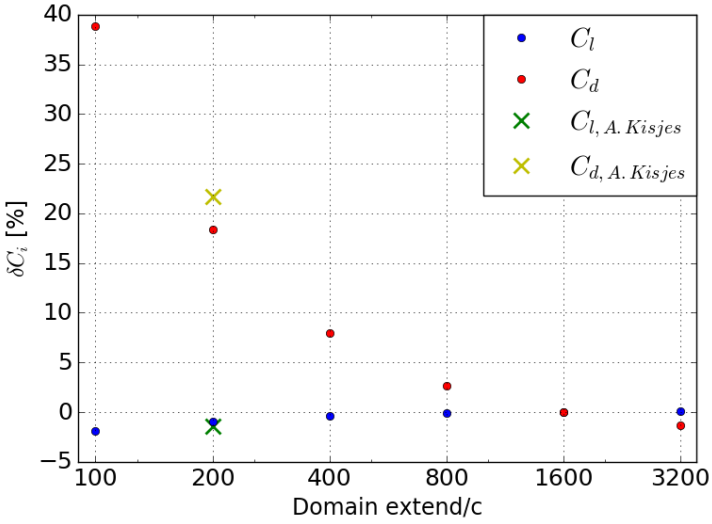

Figure 4.4: Investigation 2D domain extend

4.3 Grid sensitivity

To reduce the required computational effort, the influence of 2D grid parameters is investigated in this section. Multiple different grid parameters are evaluated over a range of settings to evaluate the effect on the resulting forces.

The flow solution depends on the discretization of the flow volume. This discretization leads to a discretization error. The refinement parameters of the grid influence the flow solution. The influence of different grid parameter and the grid refinement is evaluated in this section. This information is used to determine which grid parameters are appropriate in order to have a sufficiently small discretization error whilst maintaining a reasonable number of cells in the grid in order to limit the required computational effort.

4.3.1 Initial refinement

The initial refinement is the grid refinement at the edge of the domain. Therefore these are the coarsest cells in the domain. The influence of the initial cells over the length and width of the domain are shown in Figure 4.5. The number of initial cells has a significant influence on the required computational effort. Therefore 56 initial cells are selected whereby the deviation for lift is within 1% and drag within 3% of the results for the range of evaluated initial refinement settings.

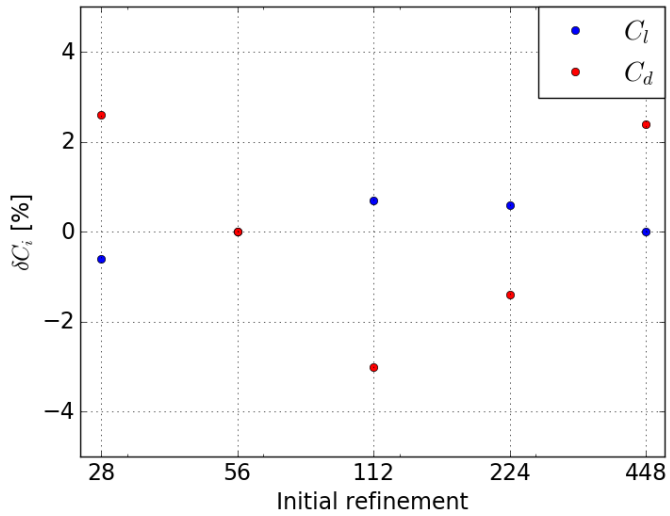

Figure 4.5: Investigation 2D initial refinement

4.3.2 Refinement diffusion

The refinement diffusion determines the extend of a certain refinement level of the grid. A larger refinement diffusion means a larger extend per refinement level and consequently requires more cells. The refinement diffusion has a less significant influence on the required computational effort compared to the initial refinement but the influence is still significant. Based on the influence as shown in Figure 4.6, a refinement diffusion of 10 is selected whereby the deviation for lift is negligible and for drag within 3% of the results for the range of evaluated refinement diffusion settings.

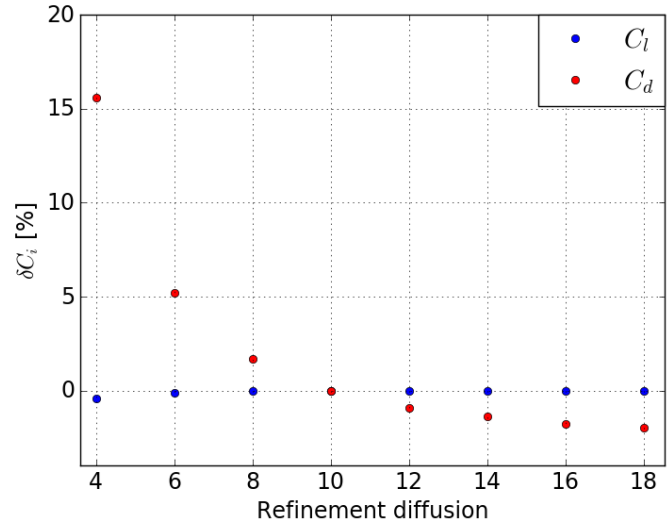

Figure 4.6: Investigation 2D refinement diffusion

4.3.3 Refinement levels

The number of refinement levels determines the refinement close to the VentiFoil surface. The refinement levels has a slightly less significant influence on the required computational effort compared to the initial refinement but is more significant than the refinement diffusion. Therefore a value of 13 is selected whereby

the deviation for lift is within 1% and drag within 3% of the results for the range of evaluated refinement level settings.

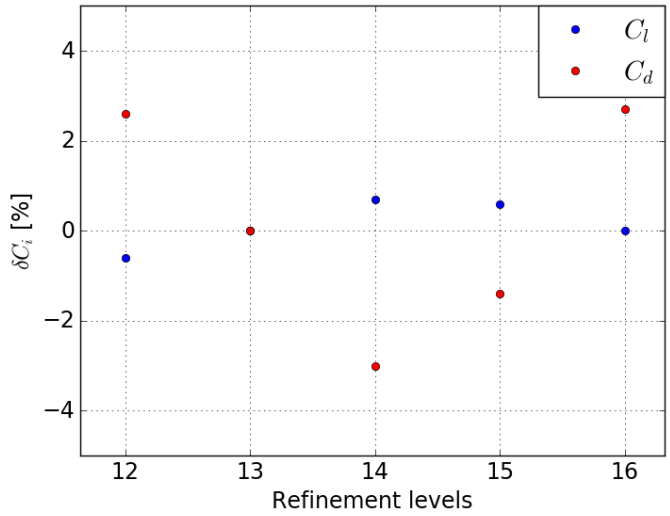

Figure 4.7: Investigation 2D refinement levels

The refinement levels and the initial refinement follow the same trend whereby the resulting forces are not much different. This is because increasing the initial cells and the refinement levels both influence the refinement close to the surface of the VentiFoil. Increasing the refinement levels only refines the cells close to the VentiFoil surface and increasing the initial refinement causes all cells in the domain to be refined. From this it can be concluded that refinement close to the VentiFoil surface has a more significant influence compared to the refinement in the far field.

4.3.4 Discretization uncertainty

The grid settings as determined previously are used to determine the parameters of the grid. In order to evaluate the discretization uncertainty, a grid refinement study according to the procedure of [10] is used. This procedure uses a series of geometrically similar grids which are shown in Appendix B. The boundary layer settings are such that the grids are geometrically similar. For the most refined grids this means a larger transition at the edge of the boundary layer refinement region. This is due to the boundary layer generation in Hexpress.

The results of this study are shown in Figure 4.8 whereby the grid with the selected settings is represented by relative step size 1.3. These grid generation settings are selected and used for the 2D parameter variation study because of the required computational effort and the limited discretization uncertainty of $\pm 1.1\%$ for C_L and C_D. These uncertainties for the geometrically similar grid series are considered small compared to the variation of the resulting forces obtained from the variation of grid parameter settings.

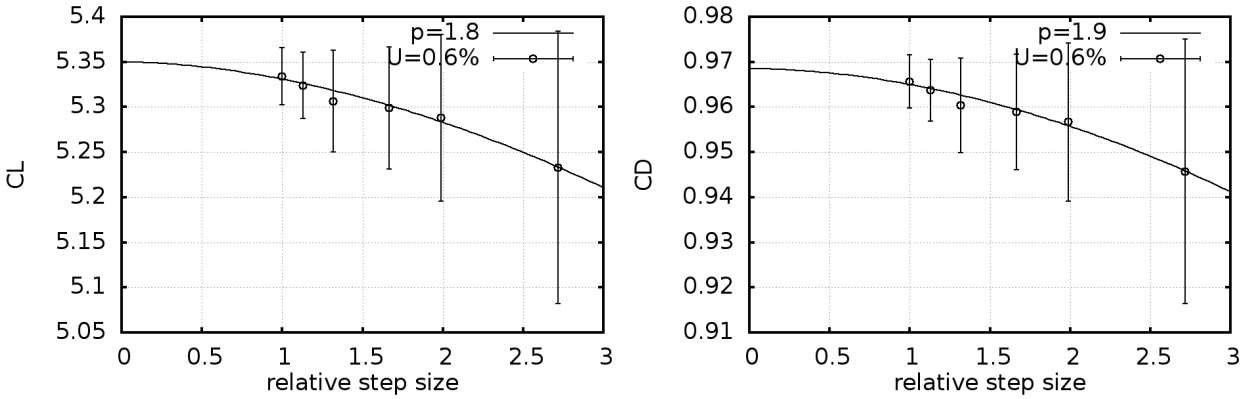

Figure 4.8: Uncertainty study 2D similar grid refinement

4.3.5 Selected grid parameters

Based on the grid sensitivity study, grid parameters which result in a grid of approximately $1.3E5$ cells as shown in Figure 4.9, Figure 4.10 and Figure 4.11 are selected.

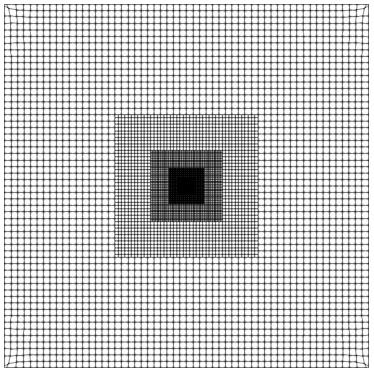

Figure 4.9: Full 2D grid

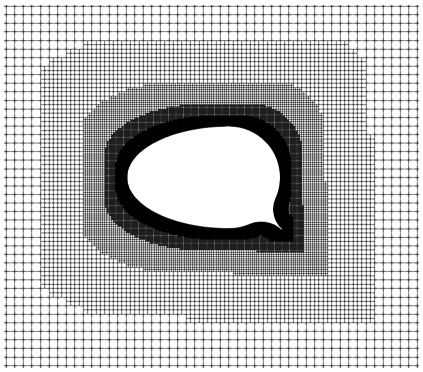

Figure 4.10: Zoomed 2D grid

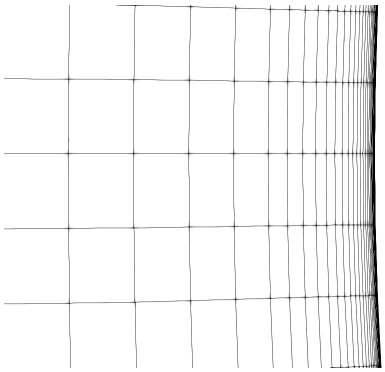

Figure 4.11: Boundary layer 2D

4.4 Performance evaluation

The purpose of a VentiFoil is to provide thrust, therefore the performance of a VentiFoil should be determined based on the produced thrust. However the thrust is not the same for every operating condition. Therefore the average thrust over all operating conditions should provide a suitable parameter to evaluate the performance of a VentiFoil and can be used make a fair comparison between different VentiFoil configurations. This enables the fair comparison between different configuration to evaluate the influence and sensitivity of different characteristic section parameters.

4.4.1 Performance in different conditions

The produced forces of a VentiFoil is evaluated in different operating conditions. Every profile section which is analyzed is simulated for 6 different angles of attack varying from 0 to 40[°] in steps of 8[°] degrees and at least 6 different suction pressures varying from 0 to at least -400[Pa] in steps of 80 pa. Therefore each section profile is simulated in at least 36 different operating conditions. The conditions which do not provide a converged solution (residuals larger than 1e-8) or configurations which have separated flow are filtered out.

Whether the flow is separated is determined by the flow direction through two velocity line monitors which monitors which are perpendicular to the surface of the suction side with a length of $0.2c$ as shown in Fig-

ure 4.12. On average, over at least 2% of the length of the line monitors, the flow passing through these line monitors should not be reversed. Otherwise the flow is considered to be separated.

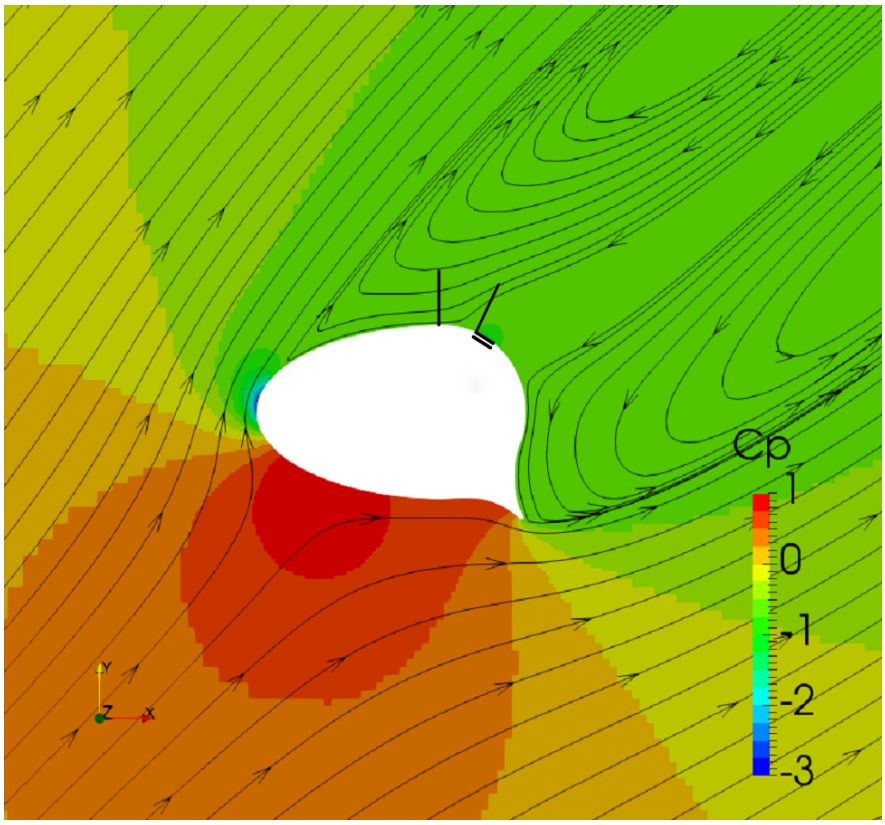

Figure 4.12: Separation monitors, separated but converged flow

The remaining simulations are used to construct a quadratic surface which represents the lift (C_L) and drag (C_D) results of one section profile in different operating conditions. These surfaces are generated using the Python scipy package to find the best fitting quadratic surface. Some examples of these surfaces are shown in Figure 4.13 for lift and Figure 4.14 for drag. The deviation of the fit accuracy to the points is determined using R^2 The mathematical description of these surfaces is stated below the figures. In these equations x represents α and y represents C_q. There are no converged and attached solutions in the region where the angle of attack is large and C_q is low because the flow has separated in this region. In order to exclude these conditions from the performance evaluation, the lift coefficients in this region are set to 0. The lift and drag performance surfaces for all evaluated geometries are shown in Appendix C.

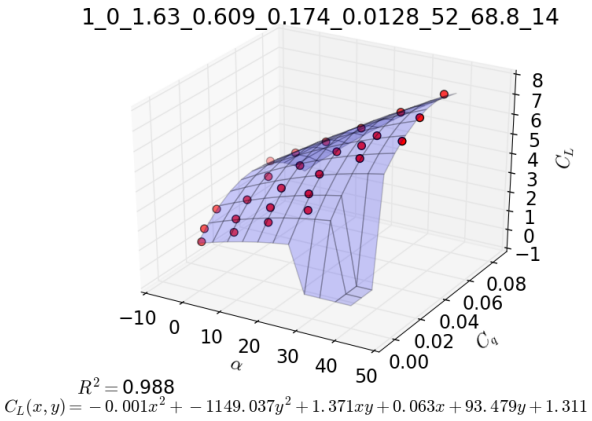

Figure 4.13: Surface fit C_L

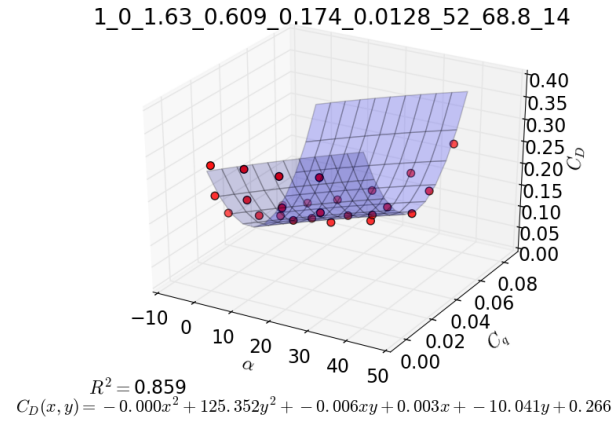

Figure 4.14: Surface fit C_D

These lift and drag coefficients are translated to thrust and side force coefficients using the apparent wind angle as described by Equation 1.10. When the thrust coefficient is negative, the VentiFoil will be folded in. Therefore negative thrust coefficients are set to 0.

$$C_T = \begin{cases} C_T & \text{if } C_T > 0 \\ 0 & \text{if } C_T \leq 0 \end{cases} \tag{4.3}$$

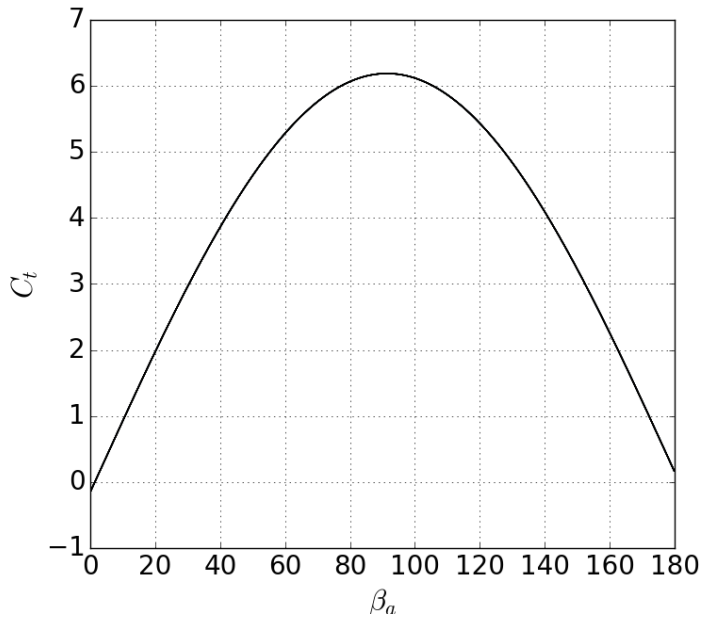

Figure 4.15: Thrust coefficient for different apparent wind angles at $\alpha = 32°$ and $C_q = 0.04$

A characteristic performance graph is obtained by multiplying the probability of a certain apparent wind angle by the thrust coefficient obtained at this apparent wind angle as shown in Figure 4.16. The performance of a section profile can be evaluated by taking the integral of the thrust coefficient for every apparent wind angle multiplied by the probability of this apparent wind angle. This is done for 600 different apparent wind angles which are distributed according to the probability of occurrence as shown in Figure 2.8. The integral over the area underneath the graph as shown in Figure 4.16 results in the average thrust coefficient ($\overline{C_T}$)

which is referred to as the performance of a certain geometry for a certain level of suction. The performance figure depends on the applied level of suction. The performance figure is plotted for a range of suction coefficients from 0.02 to 0.06, this plot is used to compare the performance of different geometries.

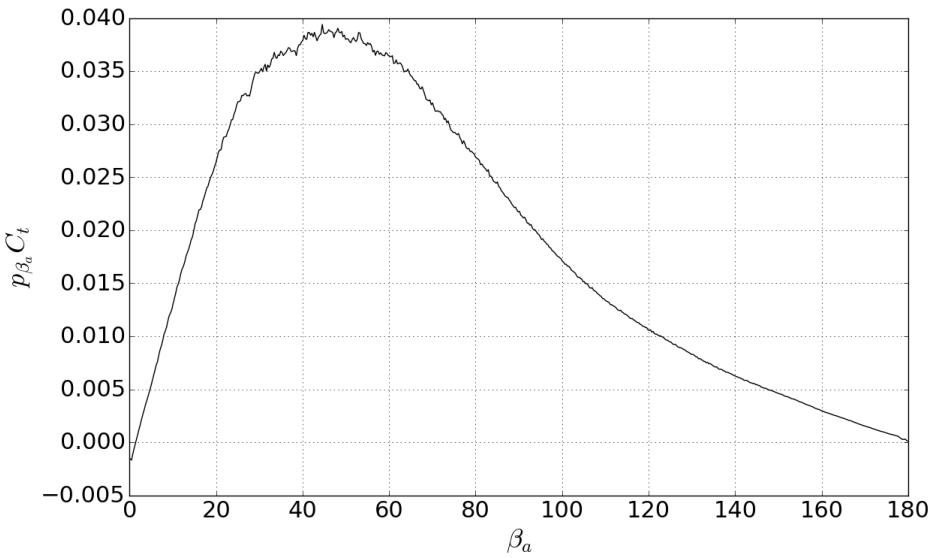

Figure 4.16: Probability of an apparent wind angle multiplied with the corresponding thrust coefficient for different apparent wind angles at $\alpha = 32°$ and $C_q = 0.04$

$$\overline{C_T} = \int_{\beta_a=0}^{180} p_{\beta_a} C_T d\beta_a \tag{4.4}$$

Not all simulations are used in the performance evaluation because some simulations diverge or result in separated flows. The fraction of simulations which is used is shown in the last numbers in the legend as shown for example in Figure 4.18. The fill density of the dashed line also represents this fraction whereby longer dashes represents a configuration which has used more simulations to evaluate the performance and is therefore less sensitive for divergence of separation in different flow conditions.

4.5 Single parameter variation

To investigate the influence of profile section parameters on performance, many different parameter settings have to be evaluated. When using combined parameter variation, the number of required simulations increases rapidly with the number of parameters settings as shown in Equation 4.5.

$$N_s = \prod_{i=1}^{N_p} N_{s,i} \tag{4.5}$$

Single parameter variation investigates parameter variations based on a base design. This method is useful to investigate the performance sensitivity for different parameters. When using single parameter variation, the required number of simulations is reduced significantly. This is therefore a useful method to investigate the base design and evaluate the sensitivity. Therefore this method is used for the parametric investigation. The number of simulations required for single parameter variation is shown in Equation 4.6.

$$N_s = \sum_{i=1}^{N_p} N_{s,i} \tag{4.6}$$

For every parameter which is investigated, a minimum of 5 different section profiles are evaluated and compared based on the obtained average thrust coefficient. This section will discuss and explain the results of these analyses.

4.5.1 Flap angle

The flap angle influences the pressure side separation location and therefore the flow on the pressure side and the size of the separated wake behind the trailling edge of the VentiFoil. The flap angle is varied from 0 to 57° in steps of 14,25° as shown in Figure 4.17. The results of this variation are shown in Figure 4.18.

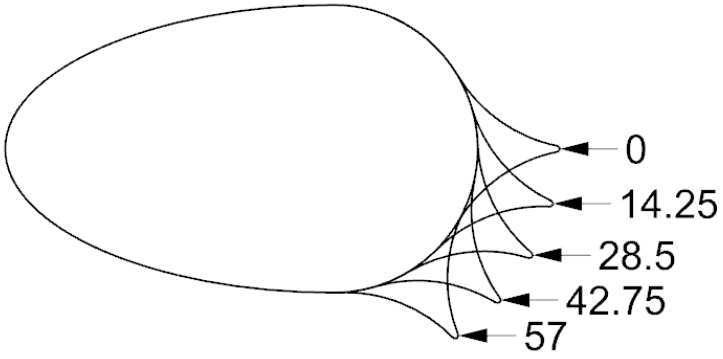

Figure 4.17: Configurations β variation

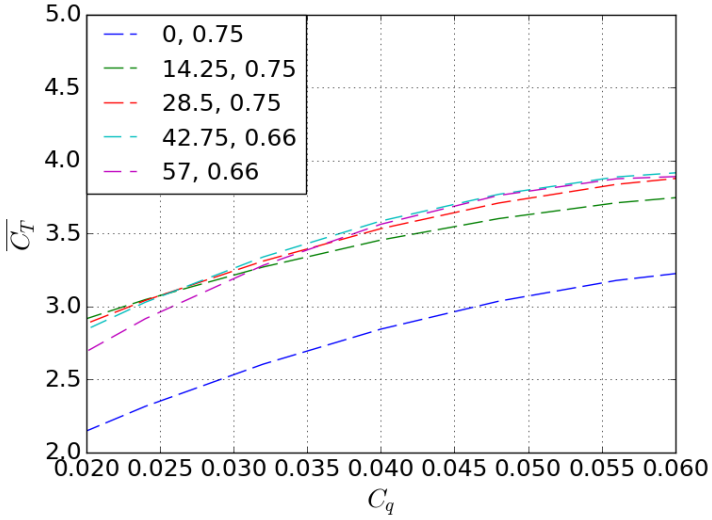

Figure 4.18: Flap angle influence on performance

The parameter variation shows that large flap angles are generally better although the influence of the flap angle is small. This is because the flap angle mainly influences size of the wake behind the VentiFoil and does not have a significant influence on the pressure profile on the suction side provided that the flap angle is sufficient to induce separation at the tip. When the flap is located on the center line, there is no separation behind the VentiFoil and the low pressure region at the leading edge is smaller and the airflow is less deflected.

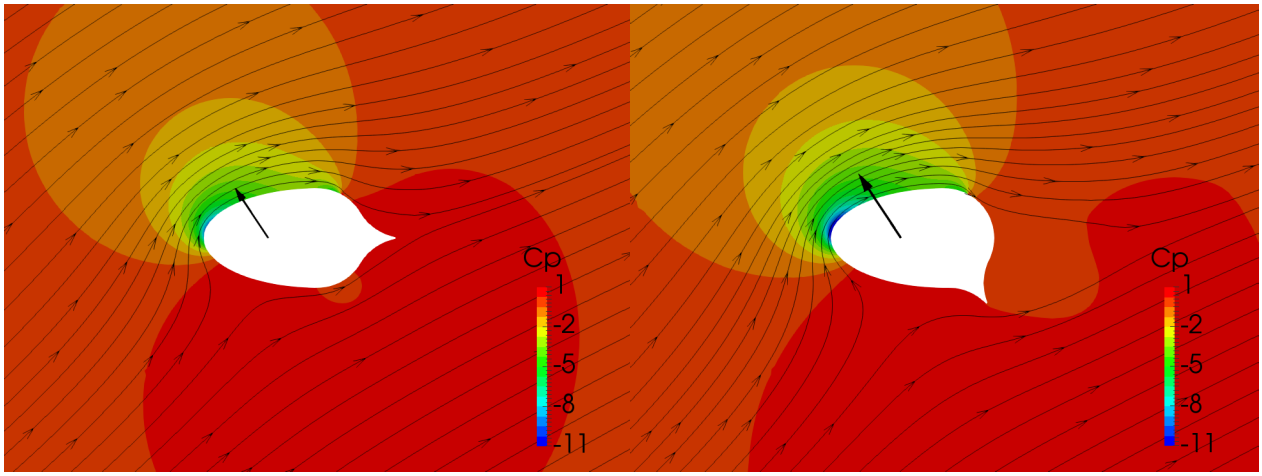

Figure 4.19: C_p contours, β variation for $\alpha = 32°$ and $p_s = -320[Pa]$, Left: $\beta = 0°$, Right: $\beta = 57°$

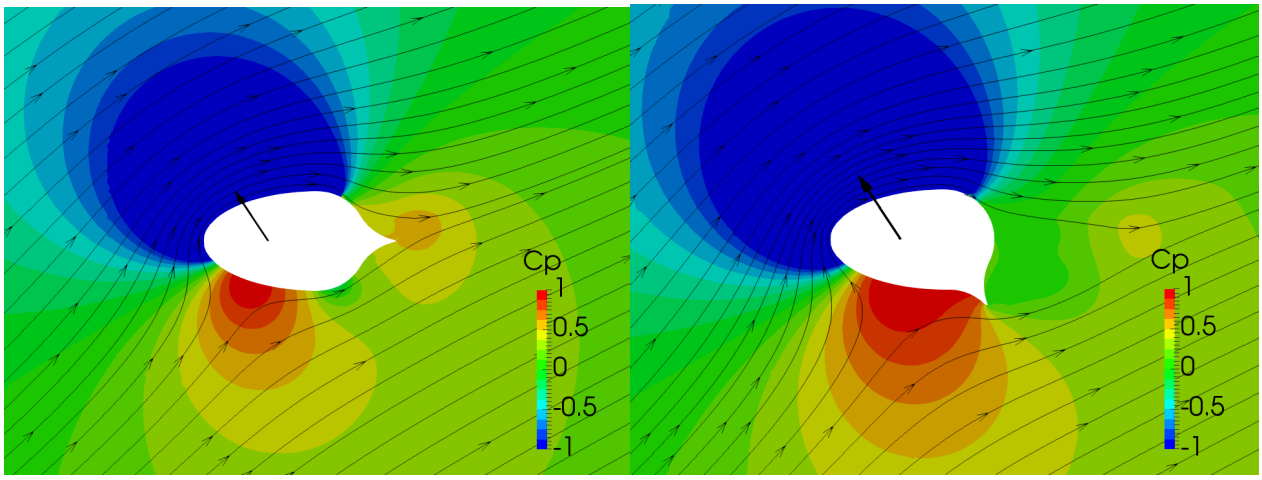

Figure 4.20: C_p contours, β variation for $\alpha = 32°$ and $p_s = -320[Pa]$, Left: $\beta = 0°$, Right: $\beta = 57°$

4.5.2 Flap length

The flap length influences the pressure side separation location and therefore the flow on the pressure side and the size of the separated wake behind the trailling edge of the VentiFoil. The flap length is varied from L_F/c from 0.12 to 24 in steps of 0.03 as shown in Figure 4.21. The results of this variation are shown in Figure 4.22.

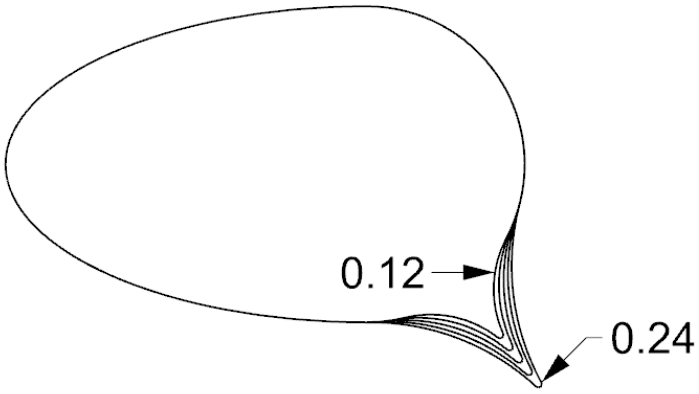

Figure 4.21: Configurations L_F/c variation

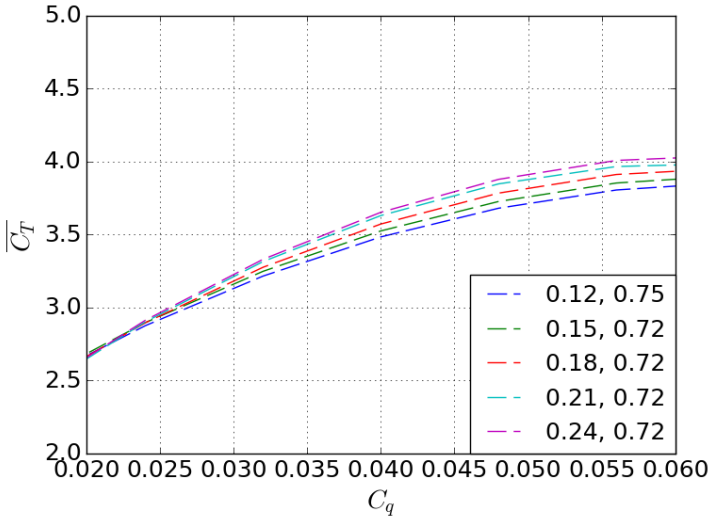

Figure 4.22: Flap length influence on performance

The parameter variation shows that larger flap lengths provides an increase in performance for all suction coefficients. This is because a larger flap increases the size of the high pressure wake behind the trailling edge of the VentiFoil. Increasing the flap length can also be seen as increasing the effective area of the profile and therefore also increasing the performance.

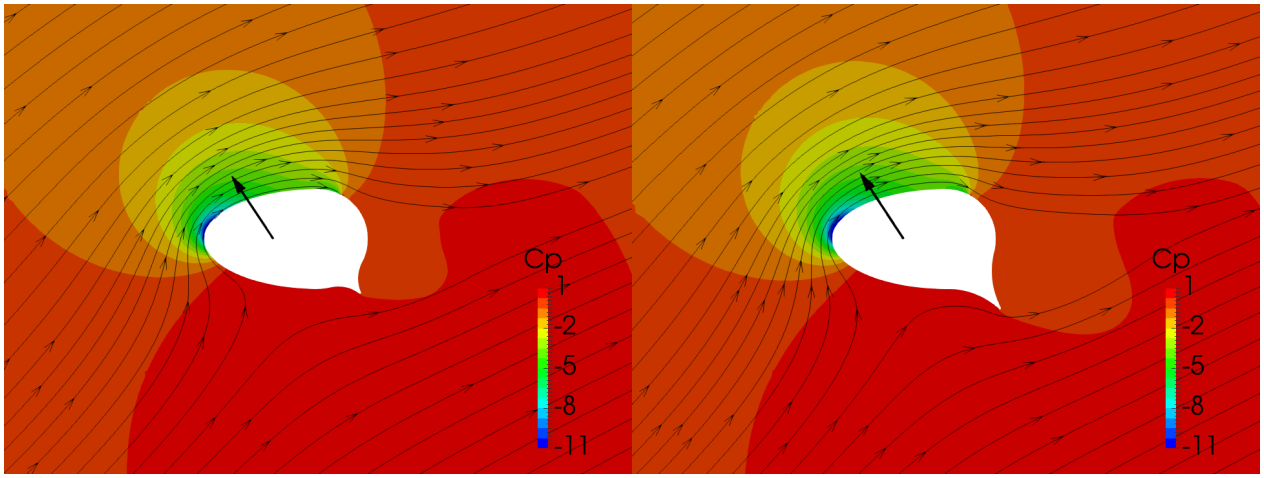

Figure 4.23: C_p contours, L_F variation for $\alpha = 32°$ and $p_s = -320[Pa]$, Left: $L_F = 0.12$, Right: $L_F = 0.24$

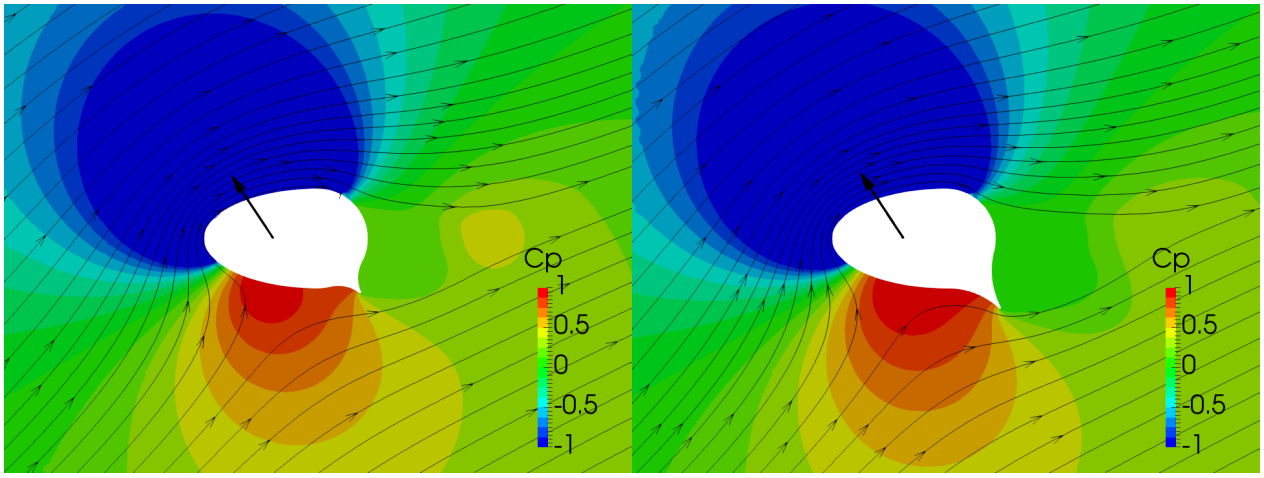

Figure 4.24: C_p contours, L_F variation for $\alpha = 32°$ and $p_s = -320[Pa]$, Left: $L_F = 0.12$, Right: $L_F = 0.24$

4.5.3 Leading edge

The shape of the leading edge influences the pressure distribution on the suction side because this depends on the curvature of the surface. The leading edge shape is varied using the h/t parameter in the range of 0 to 0.72 in steps of 0.18. The ellipse shaped leading edge is also included in analyses as shown in Figure 4.25. The results of this variation are shown in Figure 4.26.

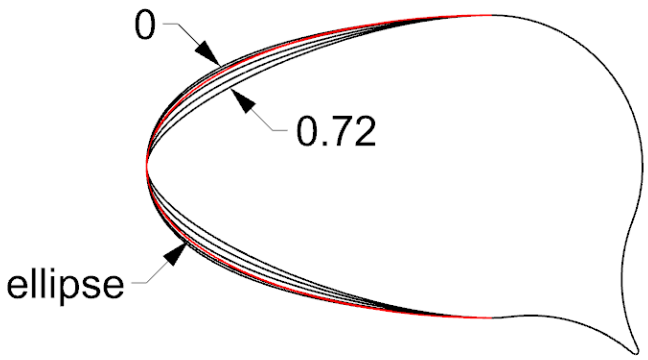

Figure 4.25: Configurations leading edge shape variation

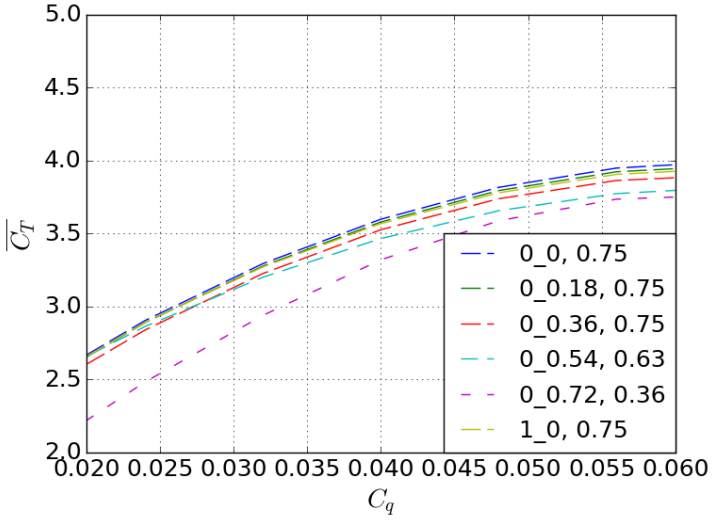

Figure 4.26: Influence of the leading edge shape on performance

The parameter variation shows that larger h/t ratios and therefore a smaller curvature at the leading edge provides an increase in performance for all suction coefficients. This is because a smaller curvature at the leading edge distributes the low pressure region over a larger area and therefore reduces the pressure gradients including the adverse pressure gradient which causes separation. Therefore section profiles with a smaller leading edge curvature are less sensitive to stall.

Figure 4.26 shows that the section profile with $h/t = 0.72$ has the least number of converged and attached simulations. This section profile is therefore most sensitive for flow changes. Because of the large curvature at the leading edge, the pressure at the leading edge is lower on a small area. Therefore there is a large pressure gradient which makes the profile more susceptible to separation.

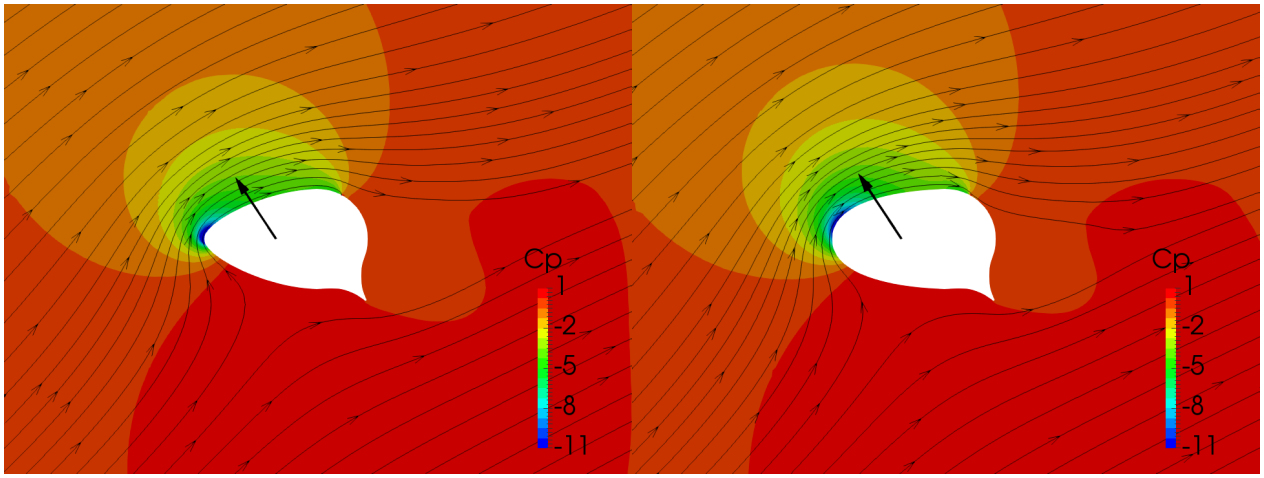

Figure 4.27: C_p contours, h/t variation for $\alpha = 32°$ and $p_s = -320[Pa]$, Left: $h/t = 0.72$, Right: $h/t = 0$

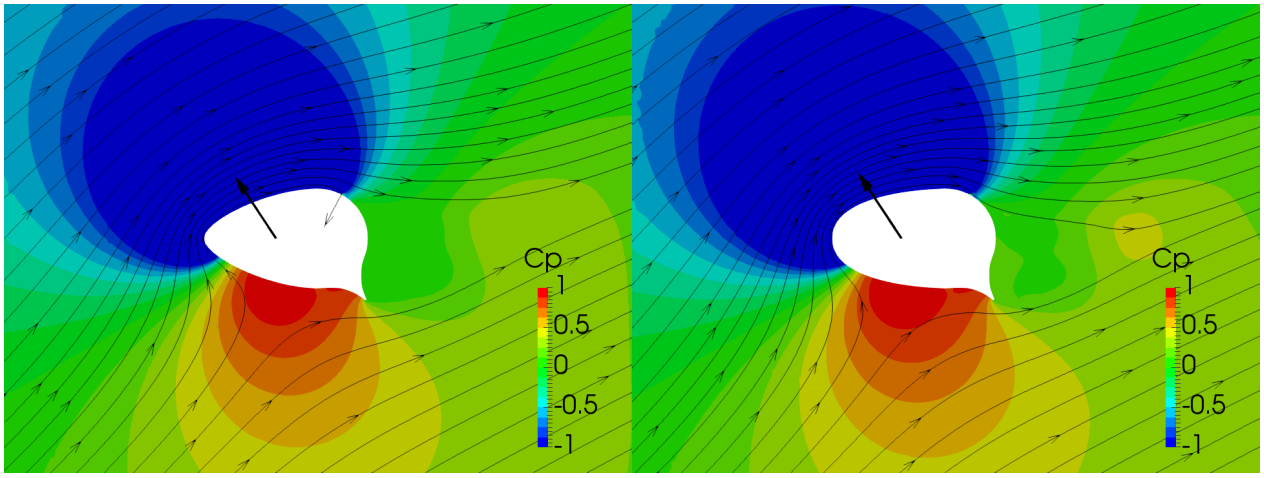

Figure 4.28: C_p contours, h/t variation for $\alpha = 32°$ and $p_s = -320[Pa]$, Left: $h/t = 0.72$, Right: $h/t = 0$

4.5.4 Thickness ratio

The thickness ratio influences flow around the entire airfoil. The thickness ratio is varied from 0.55 to 0.99 in steps of 0.11 as shown in Figure 4.29. The results of this variation are shown in Figure 4.30.

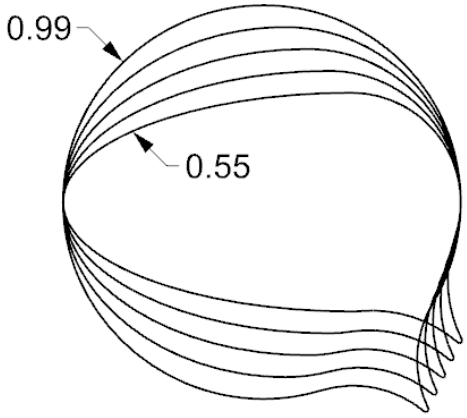

Figure 4.29: Configurations t/c variation

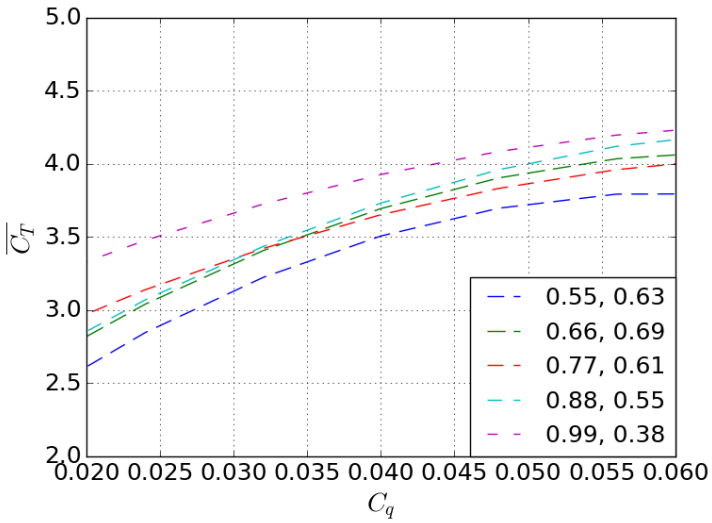

Figure 4.30: Influence of the thickness ratio on performance

The parameter variation shows that larger t/c ratios and therefore a smaller curvature at the leading edge provides an increase in performance. The flow and pressure distribution around the leading edge and the suction side is influenced most significantly by the thickness variation. This is because a smaller curvature at the leading edge distributes the low pressure region over a larger area and therefore reduces the pressure gradients including the adverse pressure gradient which causes separation. Therefore smaller leading edge curvatures require less suction to keep the flow attached and the low pressure is acting on a larger area. This confirms the findings by [4] as stated in section 1.9. The results from this study are produced using a panel method and should therefore be handled with care.

Figure 4.30 shows that the section profile with $t/c = 0.99$ has the least number of converged and attached simulations. This section profile is therefore most sensitive for flow changes.

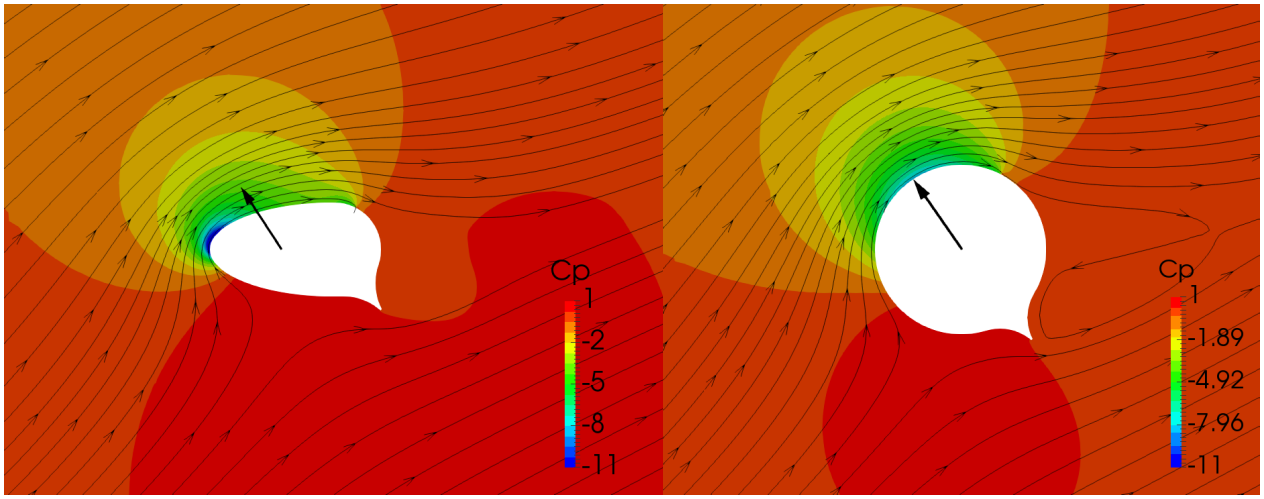

Figure 4.31: C_p contours, t/c variation for $\alpha = 32°$ and $p_s = -320[Pa]$, Left: $t/c = 0.55$, Right: $t/c = 0.99$

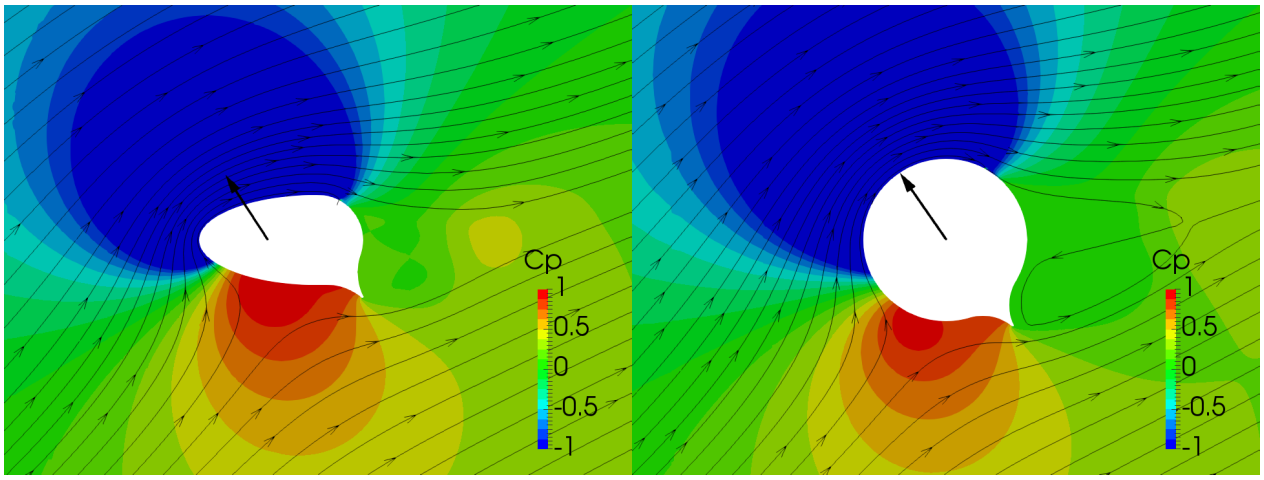

Figure 4.32: C_p contours, t/c variation for $\alpha = 32°$ and $p_s = -320[Pa]$, Left: $t/c = 0.55$, Right: $t/c = 0.99$

4.5.5 Taper ratio

Because the VentiFoils have to fit inside a container, the chord length and thickness of the VentiFoils is limited. As shown in Appendix A, the application of taper can help to fit two VentiFoils with a larger thickness ratio inside the container. However this is at the expense of the characteristic area (A). The thrust is linearly proportional to the thrust coefficient (C_T) and the characteristic area (A)as shown in Equation 1.14. Both these parameters depend on the t/c ratio.

A linear curve is fitted through the data points of $\overline{C_T}$ at a C_q of 0.04, this provides a coarse analytic expression of $\overline{C_T}$ as a function of t/c. This is shown in Figure 4.33.

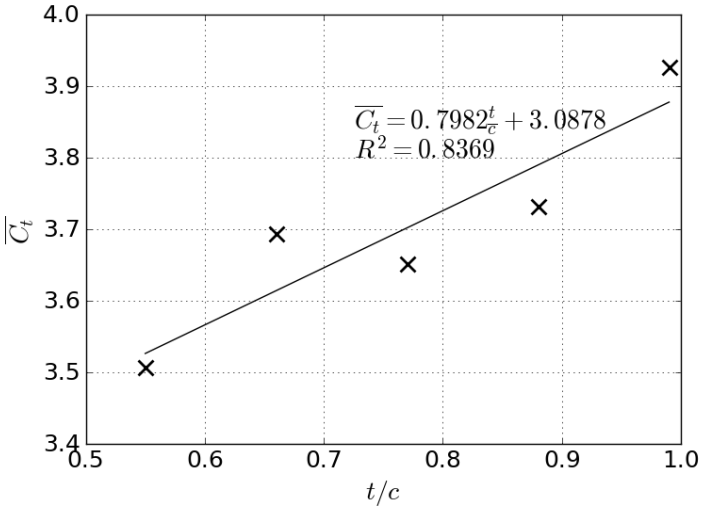

Figure 4.33: Influence of the thickness ratio on performance for $C_q = 0.04$

The function of the characteristic area is derived from geometrical relations whereby the container size and spacing from Table 4.2 is used. Between the VentiFoils, the spacing margin (s_m) is applied twice while between the VentiFoils and the edge of the container there is one spacing margin as shown in the figures of Appendix A. The expression of the characteristic area is given in Equation 4.7.

Table 4.2: Container dimensions

	$L_{container}$ [m]	$B_{container}$ [m]	s_m [m]
Value	12.029	2.35	0.1

$$A = \frac{(L_{container} - 2S_m)(B_{container} - 4S_m)}{2\frac{t}{c}} \tag{4.7}$$

The applied t/c ratio in the full scale base geometry is 0.61. In order to evaluate the t/c ratio with the best performance and and therefore the best performing taper, $\overline{C_T}A$ should be maximum. The minimum and maximum t/c which can be fitted in a container with dimensions as shown in Table 4.2 are respectively 0.445 and 0.89. This is plotted in Figure 4.34. This figure shows that smaller t/c ratio's and therefore less taper provides more average thrust provided that the full width of the container is utilized.

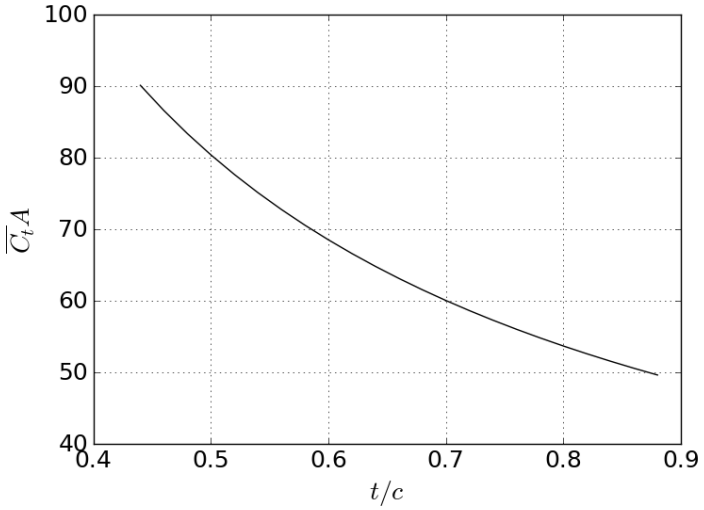

Figure 4.34: Influence of the thickness ratio on thrust performance for $C_q = 0.04$

Therefore the configuration without taper is the best performing. This can be explained by the difference in performance for the minimum and maximum thickness ratio. The average thrust coefficient increases around 10% whereas the area is doubled. Therefore the characteristic area has a more significant influence on the obtained thrust and should be maximized by applying no taper provided that the control equipment from the eConowind unit can still be fitted inside the container.

4.5.6 Suction width

The width of the suction region influences the suction side flow and therefore the low pressure distribution over this surface. The width of the suction area is varied from 8 to 24° in steps of 4° as shown in Figure 4.35. The results of this variation are shown in Figure 4.36.

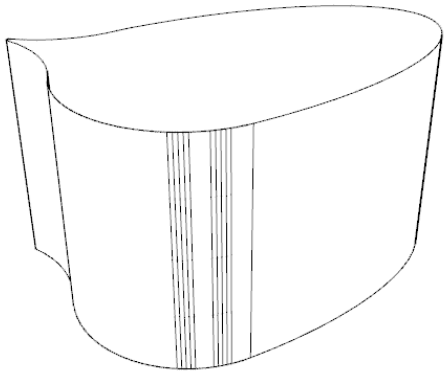

Figure 4.35: Configurations θ variation

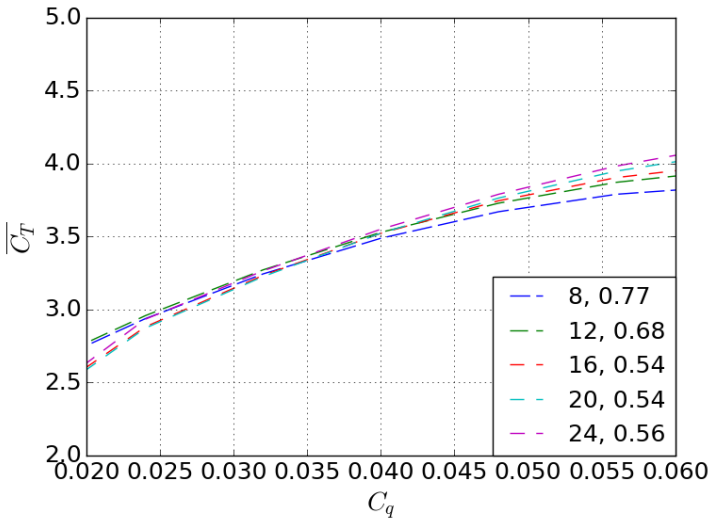

Figure 4.36: Influence of the suction width on performance

The parameter variation shows that a larger width of the suction area provides an increase in performance, mainly for large suction coefficients. This is because a larger width of the suction area allows for more gradual suction for the same suction coefficients. For a narrow suction region with a large suction coefficient, the suction region will induce large velocity gradients whereas a wider suction region allows for more gradual suction and therefore more efficient suction. The angle between the flow past the suction region and the surface of the suction region provides a parameter to evaluate the suction intensity.This is shown in Figure 4.37.

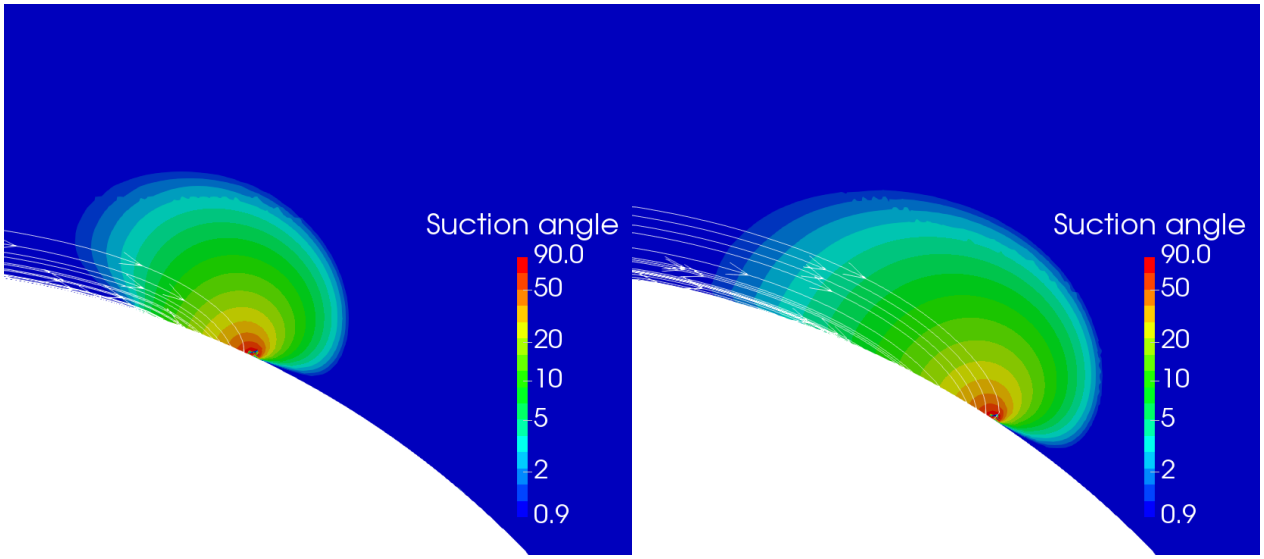

Figure 4.37: Suction angle contours, θ variation for $\alpha = 32°$ and $p_s = -320[Pa]$, Left: $\theta = 8°$, Right: $\theta = 24°$

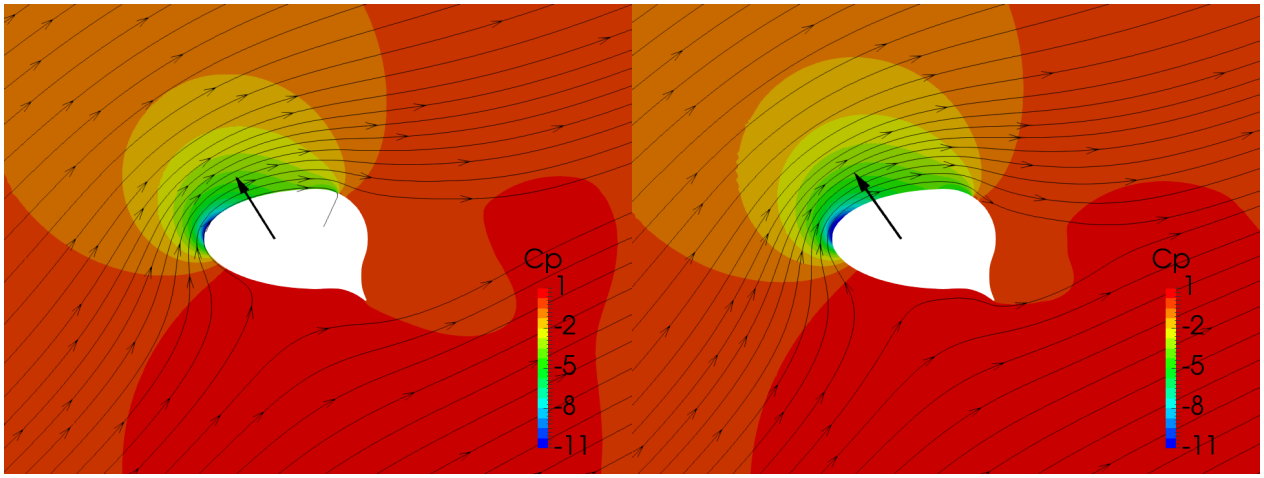

Figure 4.38: C_p contours, θ variation for $\alpha = 32°$ and $p_s = -320[Pa]$, Left: $\theta = 8°$, Right: $\theta = 24°$

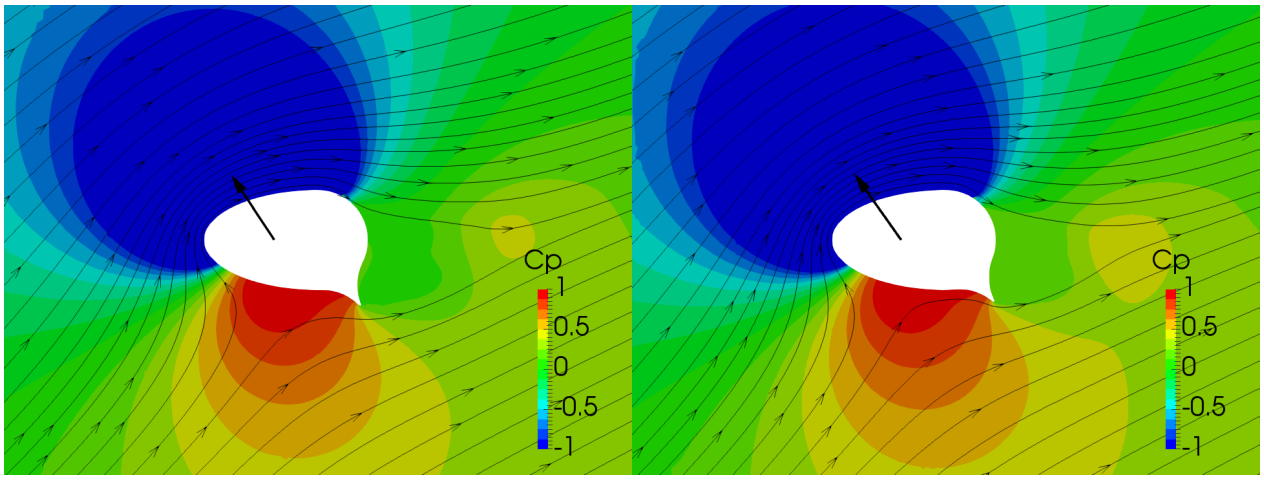

Figure 4.39: C_p contours, θ variation for $\alpha = 32°$ and $p_s = -320[Pa]$, Left: $\theta = 8°$, Right: $\theta = 24°$

4.5.7 Suction location

The location of the suction region influences the suction side flow and therefore the low pressure distribution over this surface. The suction location is varied from 36 to 80° in steps of 11° as shown in Figure 4.40. The results of this variation are shown in Figure 4.41.

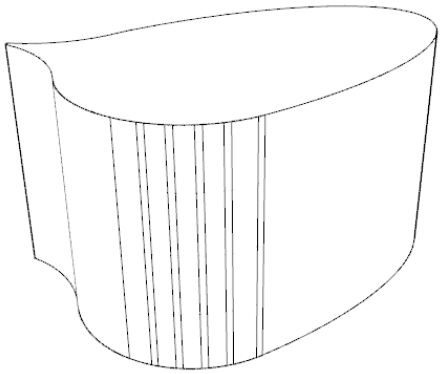

Figure 4.40: Configurations θ_m variation

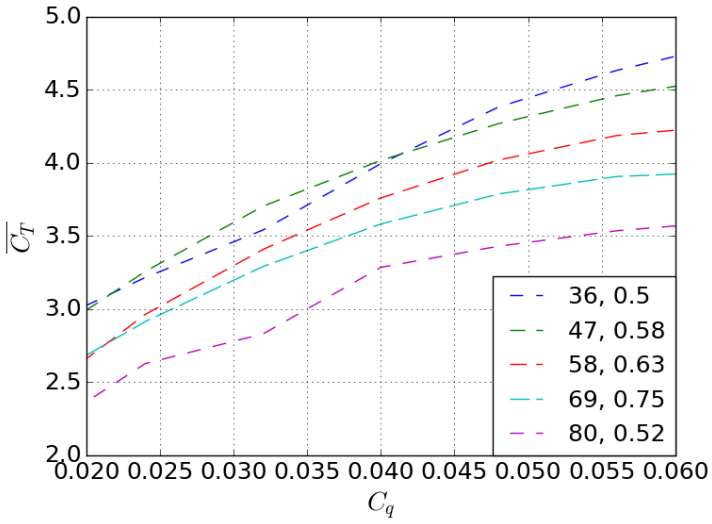

Figure 4.41: Influence of the suction location on performance

The parameter variation shows that suction locations which are located more towards the trailling edge provide a significant increase in performance, especially for large suction coefficients. This is because the low pressure area on the suction side is extended by moving the suction region further towards the trailling edge. This increases the sensitivity of the profile to separation at small suction coefficients but has the potential to provide a significant performance increase for large suction coefficients.

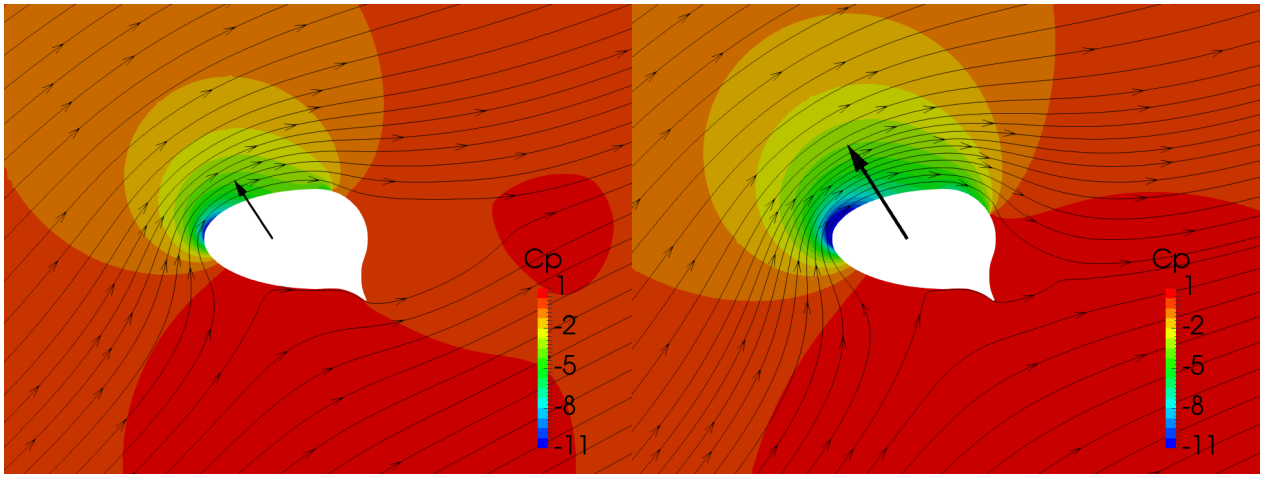

Figure 4.42: C_p contours, θ_m variation for $\alpha = 32°$ and $p_s = -320[Pa]$, Left: $\theta_m = 80°$, Right: $\theta_m = 36°$

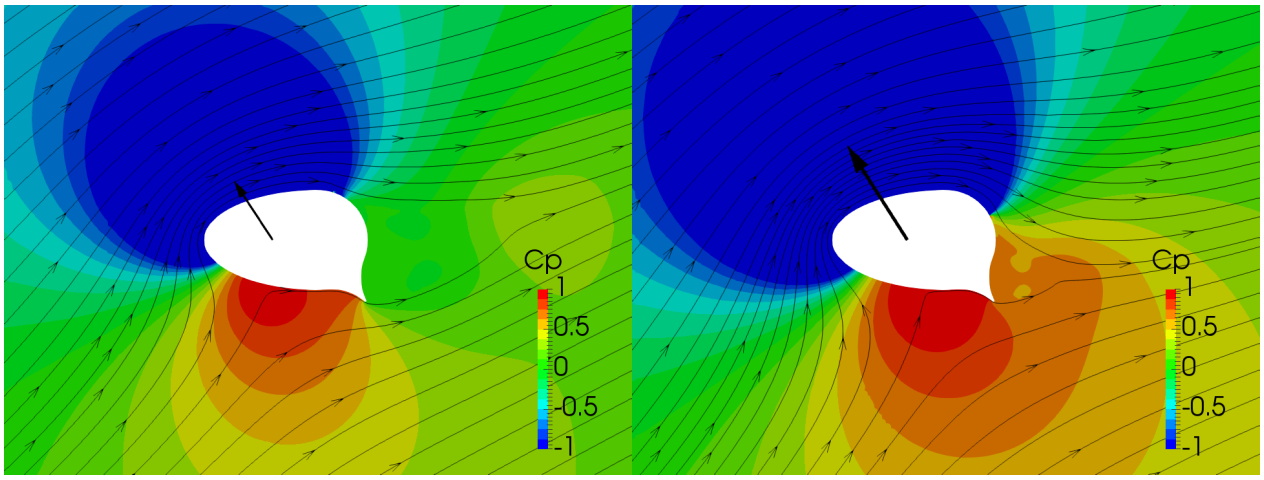

Figure 4.43: C_p contours, θ_m variation for $\alpha = 32°$ and $p_s = -320[Pa]$, Left: $\theta_m = 80°$, Right: $\theta_m = 36°$

4.5.8 Conclusions single parameter variation

The parametric variations shows the influence and sensitivity of section parameters on performance. Certain parameters have a more significant influence on performance. The influence of the section parameters can be used to increase the performance of a VentiFoil.
The position of the flap does not have a significant influence on performance as long as the flap angle is sufficient to cause separation behind the VentiFoil. The length of the flap has a clear influence on performance whereby the performance is increased by a longer flap. The shape of the leading edge has an influence on performance whereby a leading edge with smaller curvature provides better performance. A small gain in performance with respect to an elliptic leading edge can be made by reducing the maximum curvature of the leading edge. An increase in thickness ratio can increase the performance however because of the container limitations, the largest thrust from an eConowind unit can be obtained by fitting two VentiFoils with a maximum thickness ratio and no taper. The suction width has a small influence on performance but can help to increase performance at larger suction coefficients. The suction location is the most influential parameter whereby a more aft suction location provides a significant performance benefit provided that sufficient suction is applied.

Chapter 5

3D simulations

The 2D simulations do not capture vertical flow and therefore do not capture vertical effects in the flow. To evaluate the full flow around VentiFoils with a finite length, 3D CFD simulations are used. These simulations will be used to investigate tip effects and interaction between multiple VentiFoils. 3D simulations require significantly more computational effort because the grid must also be refined in vertical direction. Therefore the number of cells in the grid increases significantly.

5.1 Geometry

The 3D geometries are based on the the base geometry. The midsection profiles of this geometry is shown in Figure 1.13. The 3D profiles have a finite span and therefore also a top plate. The span of the full scale base geometry is 10.25[m] with a constant taper ratio of 0.727. The full scale base geometry is used for the investigation of the 3D computational domain size and the 3D grid sensitivity study.

5.2 Computational domain

The size of the 3D domain can influence the flow solution if the domain boundaries are not sufficiently far away from the VentiFoil. The shape of the domain is a box whereby the horizontal (xy)-plane is square and the height (z-direction) of the domain extends above the VentiFoil. For 3D simulations the height of the domain is also of importance because the top boundary condition must be sufficiently far away from the VentiFoil. Because the cells at the far field boundaries of the domain are coarse, increasing the size of the domain has a low impact on total number of cells and the required computational effort.

The influence of the domain size in horizontal plane and the height of the domain are evaluated separately such that the shape of the domain does not have to be a cube. The horizontal extend of the domain is investigated from 20 to 80 times the midsection chord length of the VentiFoil. A domain length and width of 80 times the chord length is selected because this appears to be close to the asymptotic value. The influence of the extend in horizontal plane is show in in Figure 5.1.

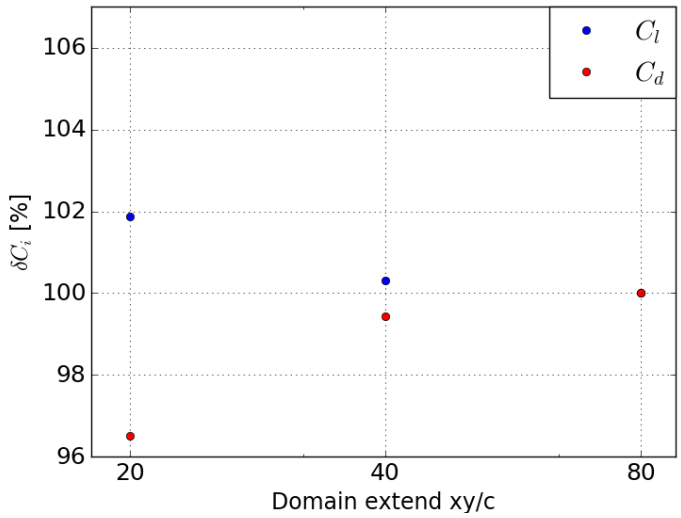

Figure 5.1: Investigation 3D domain extend in xy-plane

The vertical extend of the domain is investigated from 1.5 to 8 times the span of the VentiFoil. A domain height of 4 times the span is selected because this appears to be close to the asymptotic value. The influence of the height of the domain is show in in Figure 5.2. This figure shows that the results for lift are within 0.5% and for drag within 1% with respect to a domain extend of 8 times the span length.

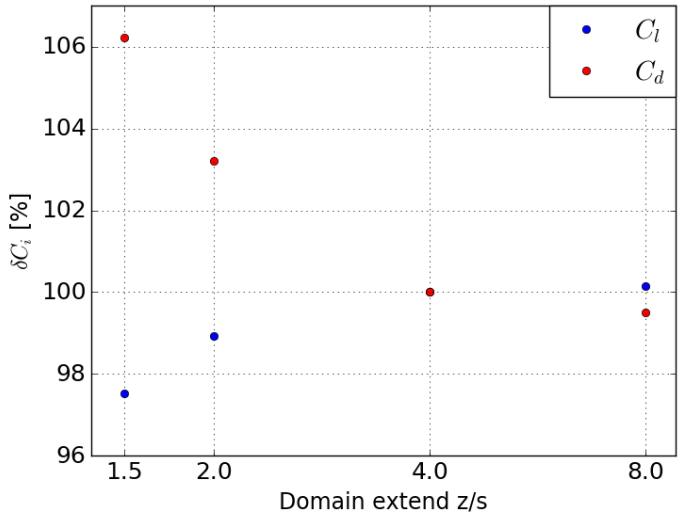

Figure 5.2: Investigation 3D domain extend in vertical direction

5.3 3D grid sensitivity

The required computational afford for 3D grids is significantly more compared to 2D grids. If the same grid refinement would be used in all directions, the number of grid cells from 2D to 3D will increase by a power of 3/2. To reduce the required computational effort, the influence of the vertical 3D grid parameters is investigated in this section. Two different grid parameters are evaluated over a range of settings to evaluate the effect on the resulting forces and select appropriate grid generation settings based on the variation in resulting forces and the required computational afford. The grid settings of the 3D grids in horizontal plane

are based on the grid sensitivity study from section 4.3 whereby the grid parameters are defined as the settings from the coarsest 2D grid from the similar grid series from subsection 4.3.4 as shown in Figure 4.8.

5.3.1 Initial vertical refinement

The initial vertical refinement defines the number of vertical cells at the edge of the domain. The influence of the initial cells over the height of the domain are shown in Figure 4.5. Based on the impact of the initial refinement on the required computational effort, 22 initial cells are selected whereby the deviation for lift is within 0.3% and drag within 1% as shown in figure Figure 5.3.

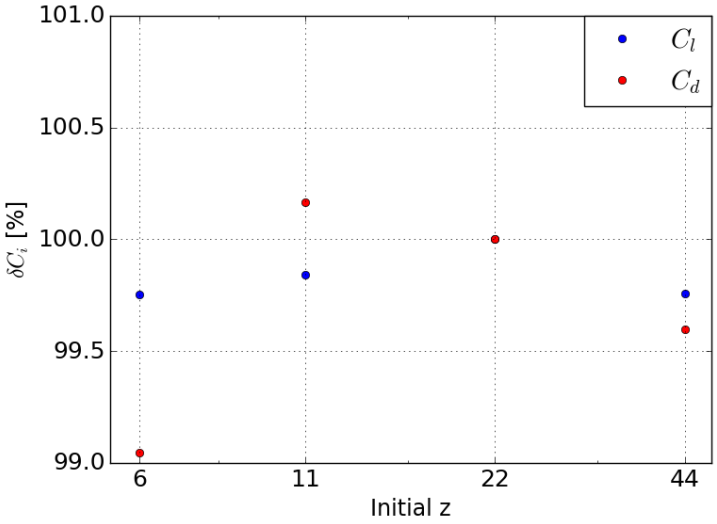

Figure 5.3: Investigation initial refinement in vertical direction

5.3.2 Maximum aspect ratio

In order to capture 3D effects, the grid is discretized in vertical direction. In order to reduce the total number of cells and therefore the required computational effort, the influence of the aspect ratio on the flow solutions is investigated. Increasing the maximum aspect ratio significantly reduces the required cells but also influences the ability of the grid to capture vertical flow effects. In order to capture vertical effects, a maximum aspect ratio of 2 is specified at the top of the VentiFoil where the most significant vertical effects are expected. Two grids with a different vertical refinement caused by different aspect ratio settings are shown in Figure 5.4 and Figure 5.5. Based on the results from Figure 5.6, an aspect ratio of 8 is selected. This aspect ratio provides results which are relatively close to the asymptotic value whereby the deviation for lift is within 0.4% and drag within 0.1% of the values for he most refined grid with an aspect ratio of 2. Therefore the results are not very sensitive for the aspect ratio. This is because the largest part over the span of the VentiFoil is not influenced by vertical flow and the region which is influenced by vertical flow close to the top of the VentiFoil contains additional refinement in vertical direction.

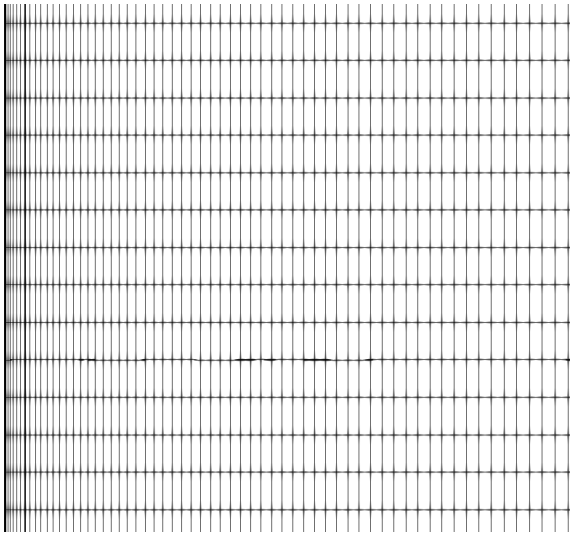

Figure 5.4: Side view leading edge grid, aspect ratio 2

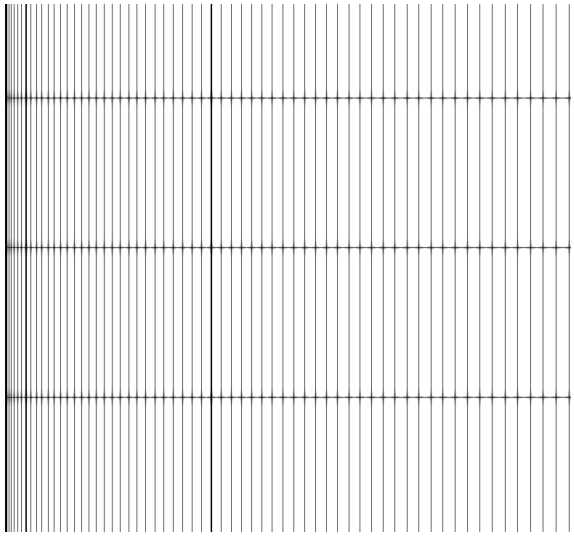

Figure 5.5: Side view leading edge grid, aspect ratio 8

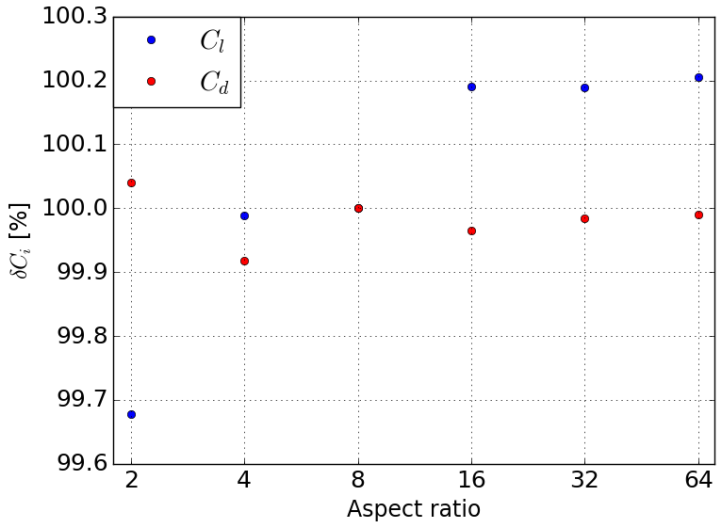

Figure 5.6: Investigation maximum aspect ratio

5.3.3 Selected grid parameters

Based on the 3D grid sensitivity study, grid parameters which result in a grid of approximately 5E6 cells without end plate and 7E6 with end plate are selected. The 3D results appear to be less sensitive for changes in the vertical grid refinement settings of the initial vertical refinement and the maximum aspect ratio. Therefore it appears that the grid refinement in horizontal plane has a more significant influence. An impression of a grid with the selected parameters is shown in Figure 5.7, Figure 5.8 and Figure 5.9.

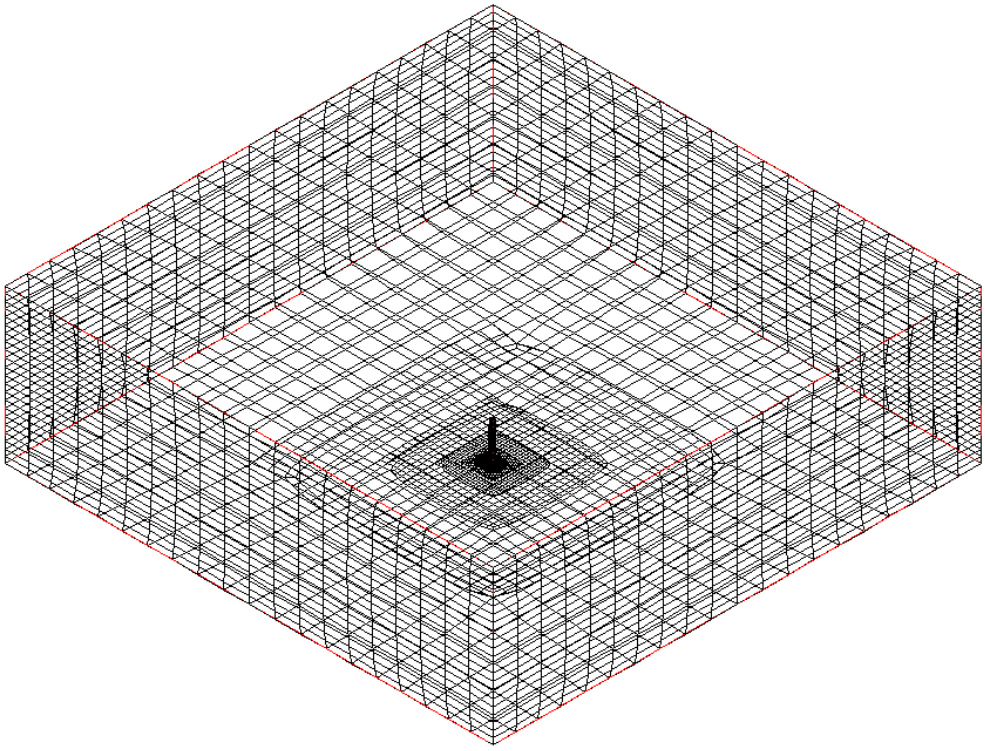

Figure 5.7: Impression 3D grid with selected parameter settings

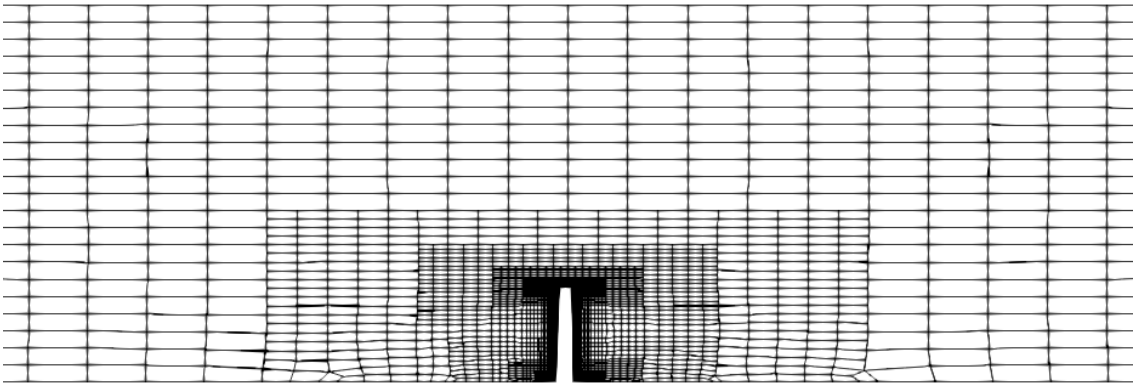

Figure 5.8: Slice of the 3D grid over xz-plane

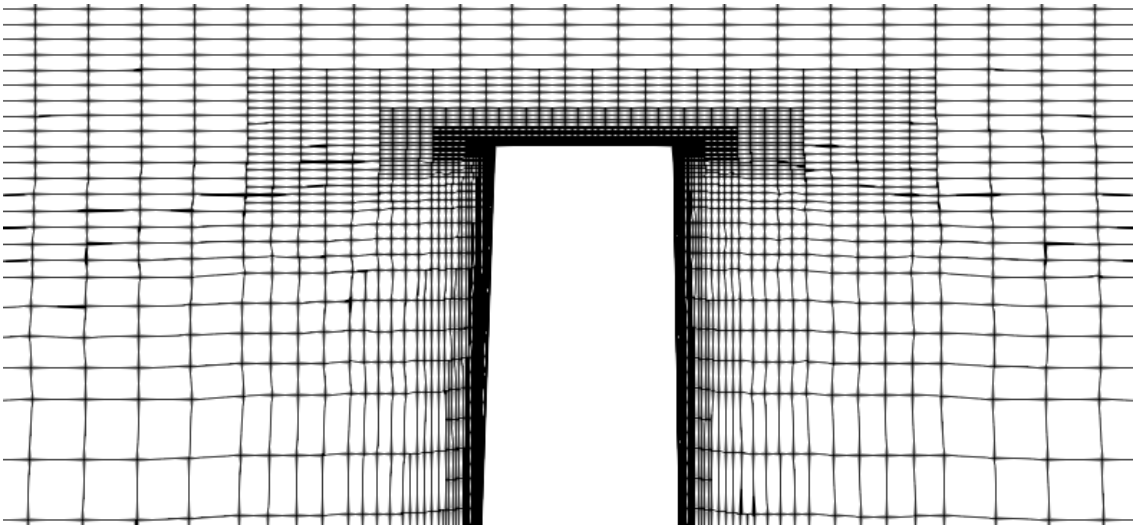

Figure 5.9: Slice of the 3D grid over xz-plane zoomed on the tip

5.4 Tip effects

Because the VentiFoils are of finite span, the influence of tip effects should be accounted for. Due to the pressure difference between the windward and leeward side, a vortex is developed at the top of the VentiFoil. This causes a loss of lift and an increase in drag and is therefore undesirable.

Tip vortices develop on the top as well as on the bottom of the VentiFoil close to the container. Due to the structure around the bottom of the VentiFoil, the losses at the bottom are assumed small compared to the losses at the top because the surrounding structure reduces the wind velocity at the bottom as previously explained in section 2.5.

The vertical velocity shows the tip vortex whereby the maximum velocity of the vortex is in the order of the far field reference velocity. An impression of the tip vortex for a VentiFoil without end plate is shown in Figure 5.13.

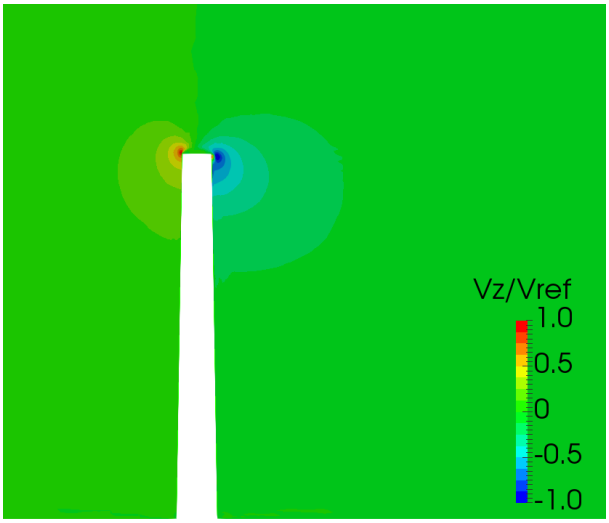

Figure 5.10: Front view slice of the relative vertical velocity at the widest point of the profile

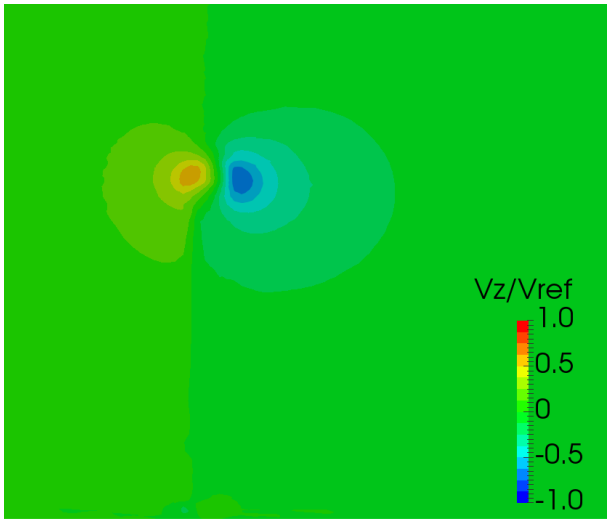

Figure 5.11: Front view slice of the relative vertical velocity 1[m] behind the trailling edge of the profile

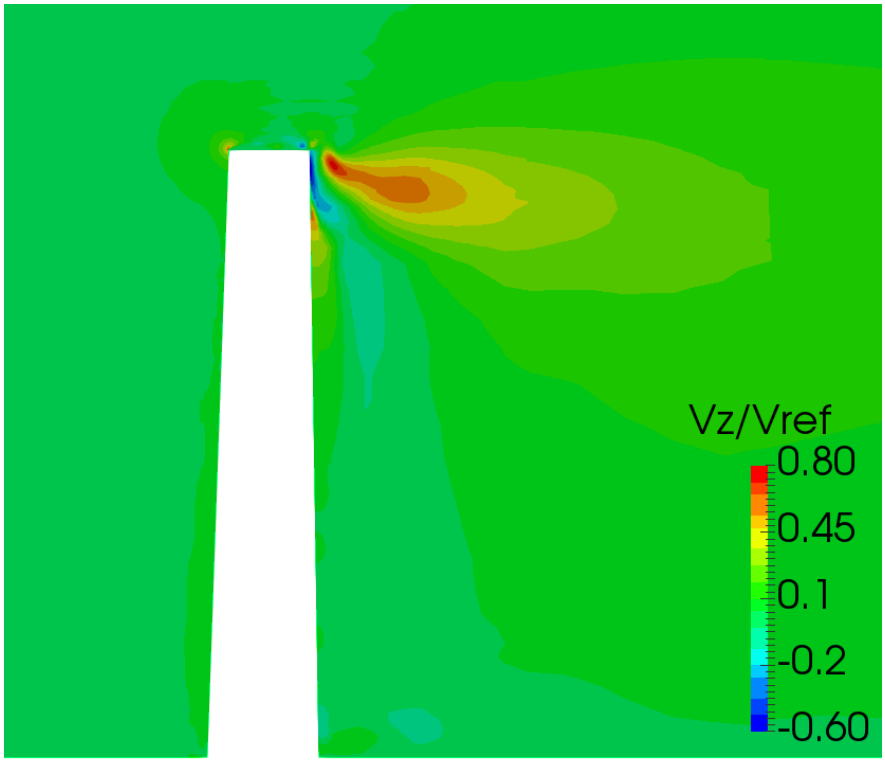

Figure 5.12: Side view slice of the relative vertical velocity over the middle of the profile

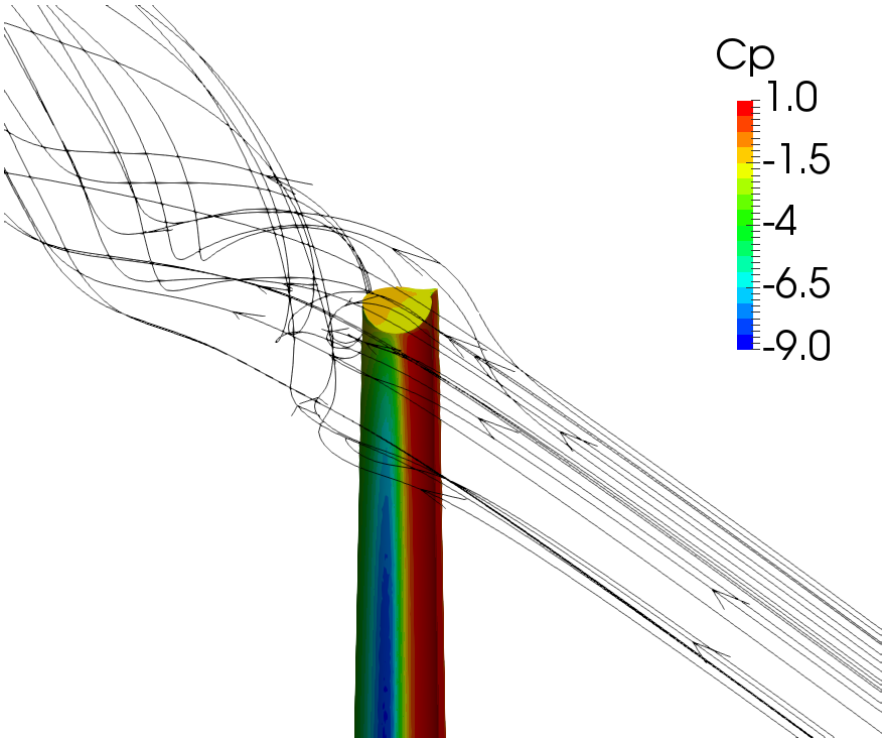

Figure 5.13: The tip vortex over the top of a VentiFoil without end plate visualized using streamlines

5.4.1 Span variation

The influence of the tip vortex is most significant on VentiFoils with a small span. This is because only the tip region is influenced by the end effects. In order to evaluate the significance of the tip effects and the influence of change in span, four different span lengths of 5[m], 10[m], 15[m] and 20[m] are evaluated.

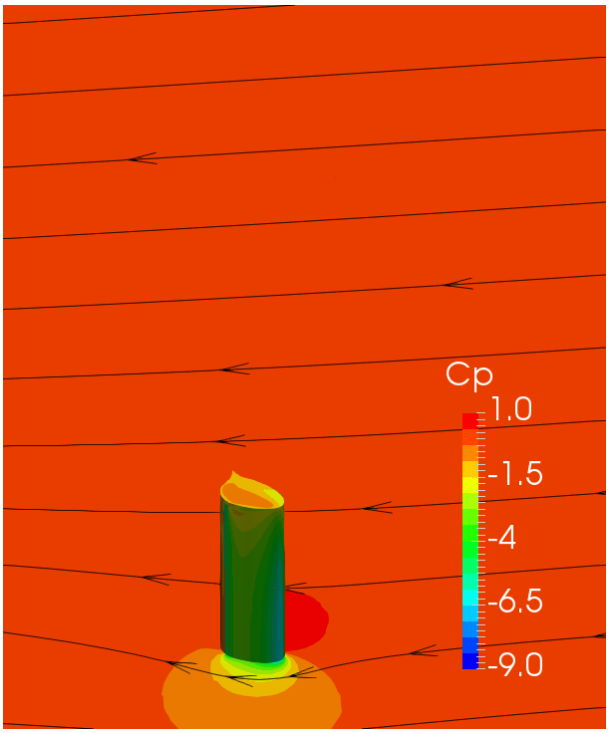

Figure 5.14: Pressure distribution for $s = 5[m]$

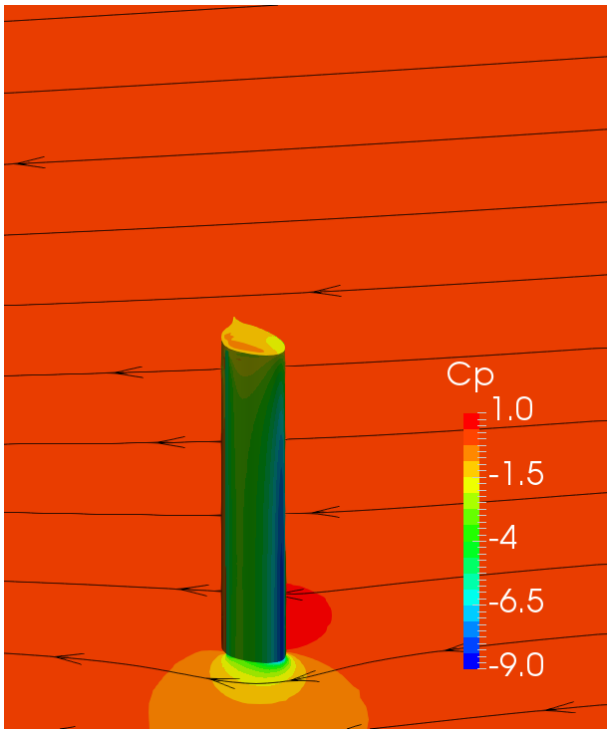

Figure 5.15: Pressure distribution for $s = 10[m]$

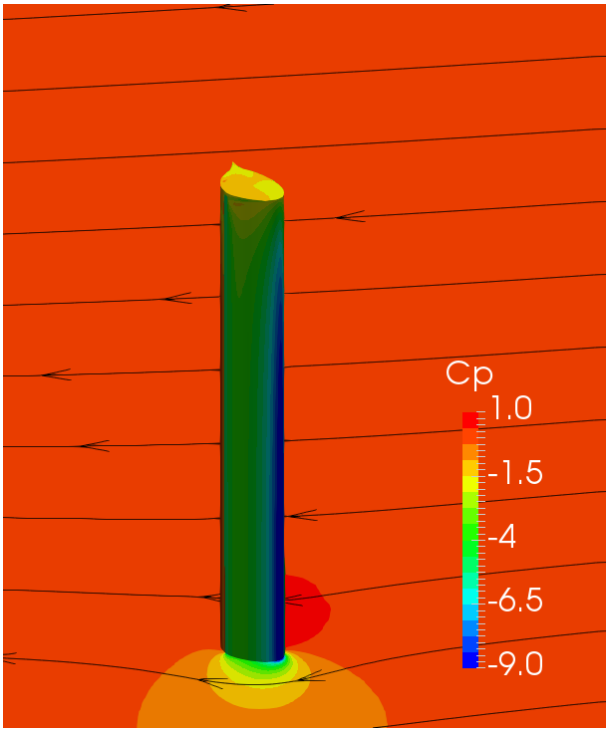

Figure 5.16: Pressure distribution for $s = 15[m]$

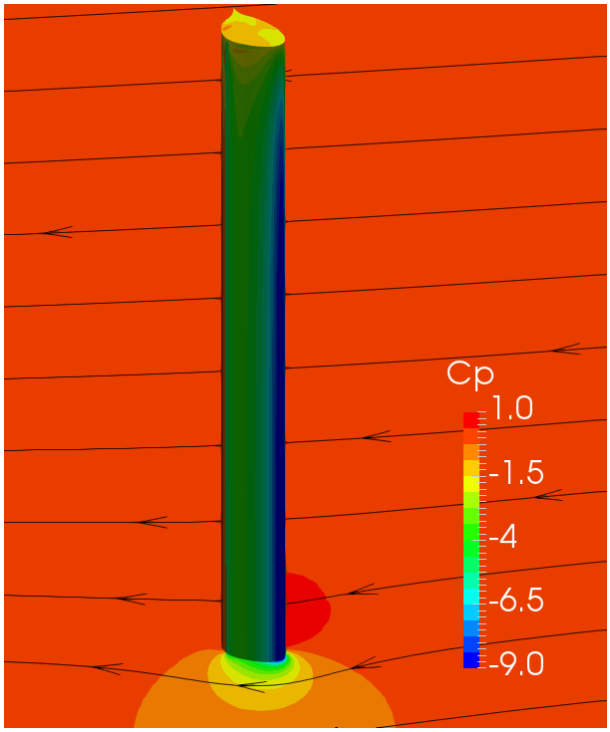

Figure 5.17: Pressure distribution for $s = 20[m]$

Figure 5.14 to Figure 5.17 show that the lowest pressure on the suction side close to the leading edge of the profiles with a short span is less significant. This indicates that these profiles are working less effectively. The influence on lift and drag is shown in Figure 5.18. This figure shows that a larger span results in a larger C_L and smaller C_D even though C_q is somewhat smaller. Therefore profiles with a larger span are more efficient.

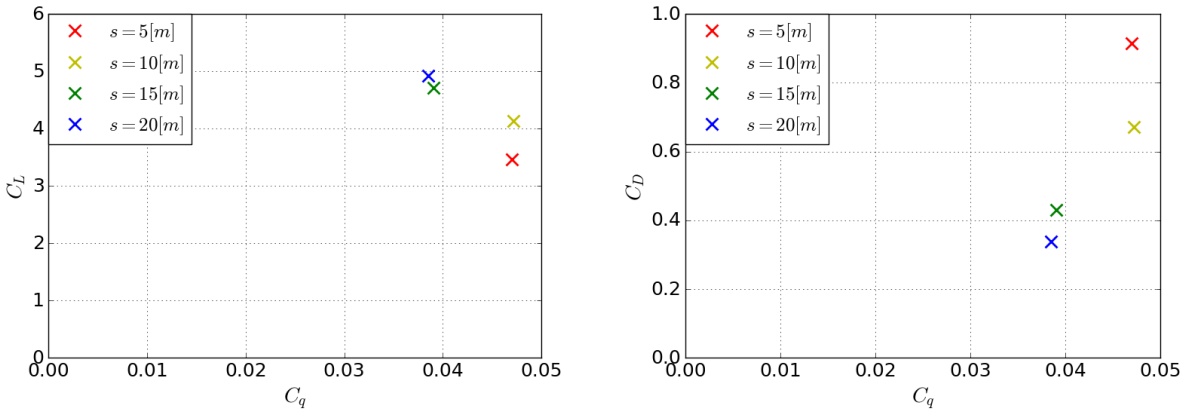

Figure 5.18: Influence of span on lift and drag

The lift and drag results are plotted in Figure 5.19 which provides a more clear trend of the influence of span on the lift and drag forces for C_q values around 0.042. This figure also shows that the lift and drag forces tend towards the results of 2D simulations with increasing span. This is because the influence of the tip effects become less significant for increasing span. The span of the VentiFoils applied in the eConowind unit is 10.25[m]. The tip effects have therefore a significant influence on the generated lift and drag forces which will negatively effect the performance of a VentiFoil.

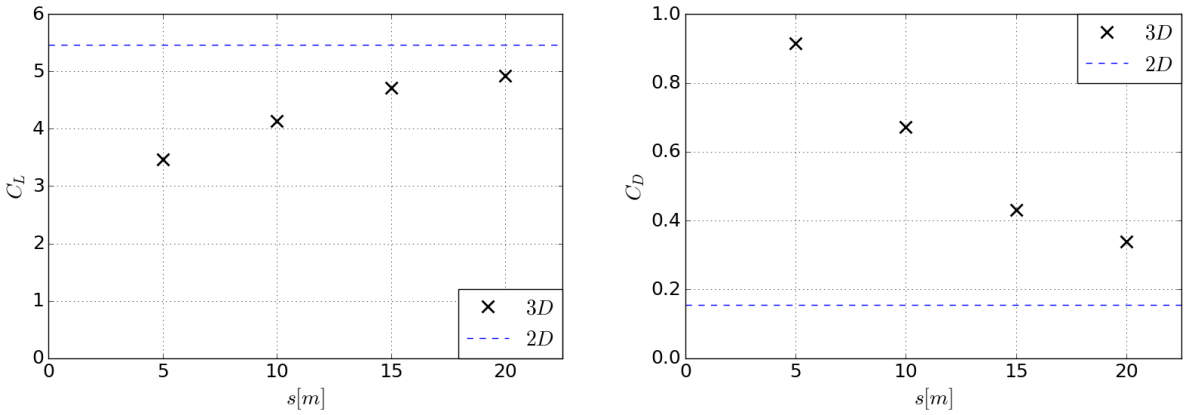

Figure 5.19: Influence of span on lift and drag for $C_q \approx 0.042$

5.4.2 End plate geometry

The tip vortex losses at the top can be reduced by applying an end-plate at the top as used by [1]. The geometry of the end plate is such that the vortex roll-up is disturbed by separating the low pressure region on the suction side and the high pressure region on the pressure side.

The width and the height of the end plate is limited because the end plate has to fit within the thickness and chord dimensions of the top in order to be able to fold inside the container. When tacking, the plate can then rotate to the other side, just as the flap rotates to the other side when tacking. In order to allow the end plate to work effectively, the end plate is able to rotate off center line to both sides. The center of rotation is near the leading edge of the VentiFoil as shown in Figure 5.20.

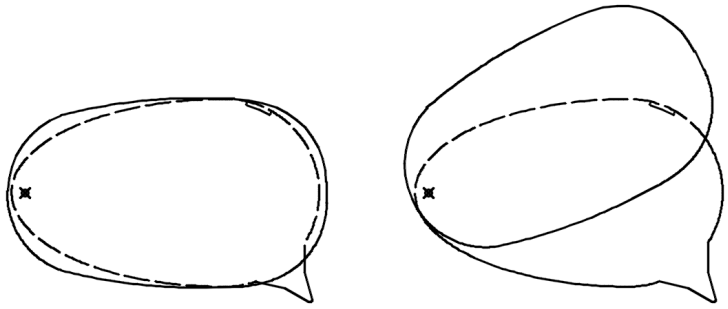

Figure 5.20: Rotatable end plate geometry

5.4.3 End plate position

In order to evaluate the effect of the end plate position on the generated forces, the VentiFoil with end plate is simulated in four different conditions including the condition without end plate as a baseline case.

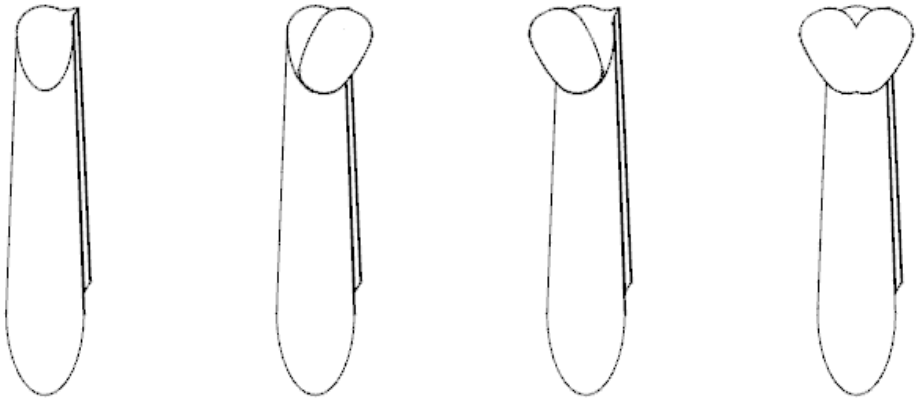

Figure 5.21: End plate configurations, from left to right: no end plate, windward end plate, leeward end plate, end plate on both sides

The position of the end plate should be such that the low pressure side on leeward is covered at the top. This should allow the low pressure region to extend further upwards and therefore the span of the VentiFoil will be more efficiently used. This is shown in pressure plots whereby the low pressure region is reduced at the top for Figure 5.22 and Figure 5.23 compared to the configurations where the end plate covers the low pressure area as shown in Figure 5.24 and Figure 5.25. Therefore the configurations whereby the end plate is located on the leeward side provides the largest benefit from the end plate. This is shown in Table 5.1.

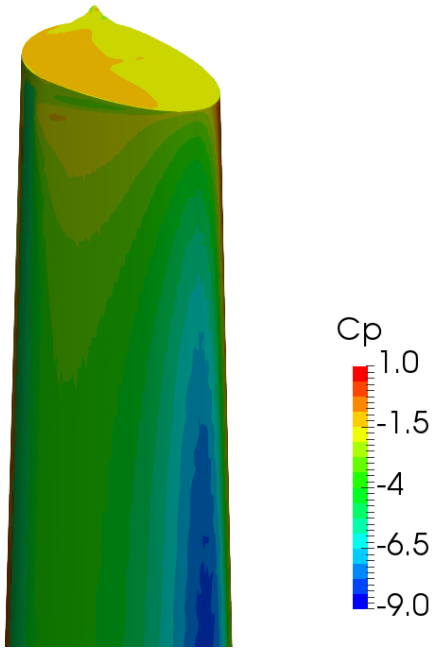

Figure 5.22: Pressure distribution on the suction side without end plate

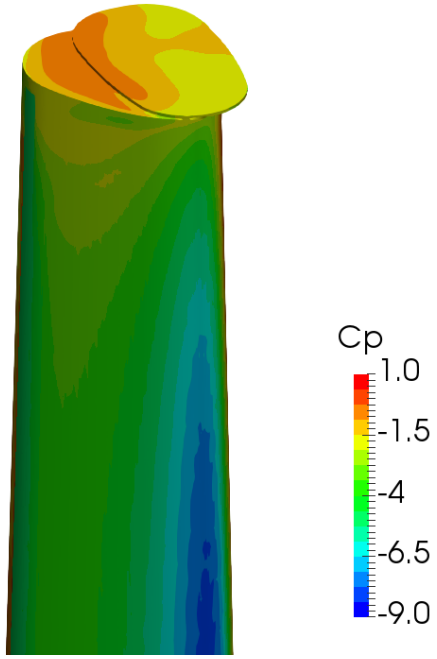

Figure 5.23: Pressure distribution on the suction side with a windward end plate

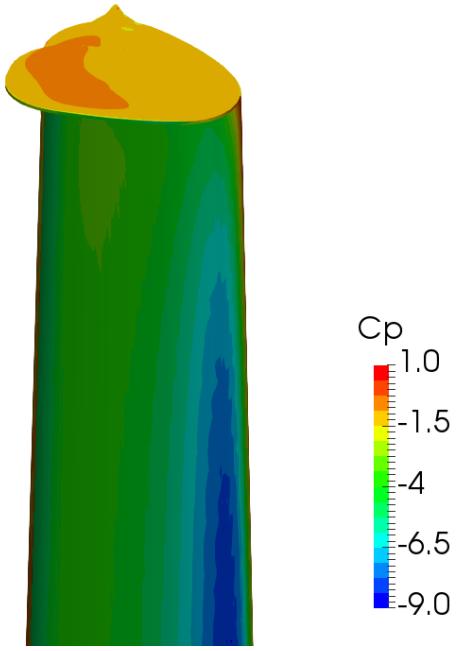

Figure 5.24: Pressure distribution on the suction side with a leeward end plate

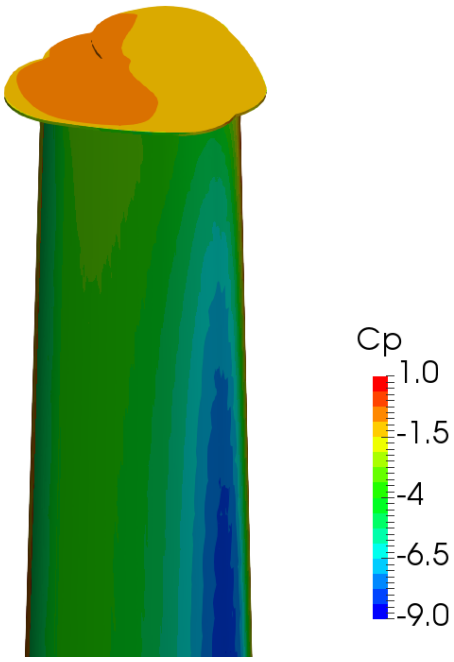

Figure 5.25: Pressure distribution on the suction side with two end plates on both windward and leeward

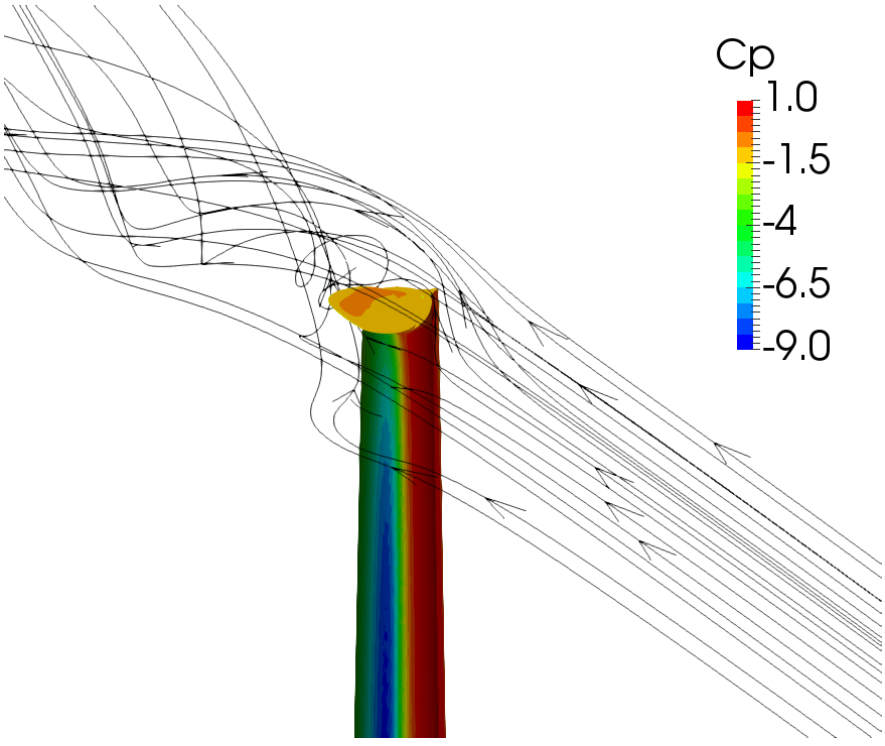

Figure 5.26: The tip vortex over the top of a VentiFoil with a leeward end plate visualized using streamlines

Table 5.1: Lift and drag coefficients for different end plate configurations

Configuration	No end plate	Windward	Leeward	Two end plates
C_L	4.84	4.85	5.02	5.01
C_L difference [%]	0	0.229	3.77	3.54
C_D	0.838	0.835	0.809	0.806
C_D difference [%]	0	-0.328	-3.47	-3.88
C_L/C_D	5.77	5.81	6.21	6.22
C_L/C_D difference [%]	0	0.559	7.50	7.72

5.5 Interaction

Because two VentiFoils are fitted inside a eConowind unit, the VentiFoils are close together and will interact because both VentiFoils disturb the flow. The downwind VentiFoil will be influenced most because of the wake from the windward VentiFoil. Therefore the interaction is worst when the apparent wind angles are small when sailing upwind or when the angles are large when sailing downwind. Because the VentiFoils are fitted diagonally inside the eConowind unit, the influence of interaction will be more significant for apparent wind from starboard for the current configuration.

5.5.1 Grid refinement

The grids around the VentiFoils use the same settings as the 3D grid parameters as determined in section 5.3. In order to accurately capture the interaction of the two VentiFoils, the grid in the wake of the leading airfoil is refined. This results in a grid with a total of 1.3E7 cells for the simulation of two VentiFoils. An indication of the refinement between the VentiFoils is shown in Figure 5.27.

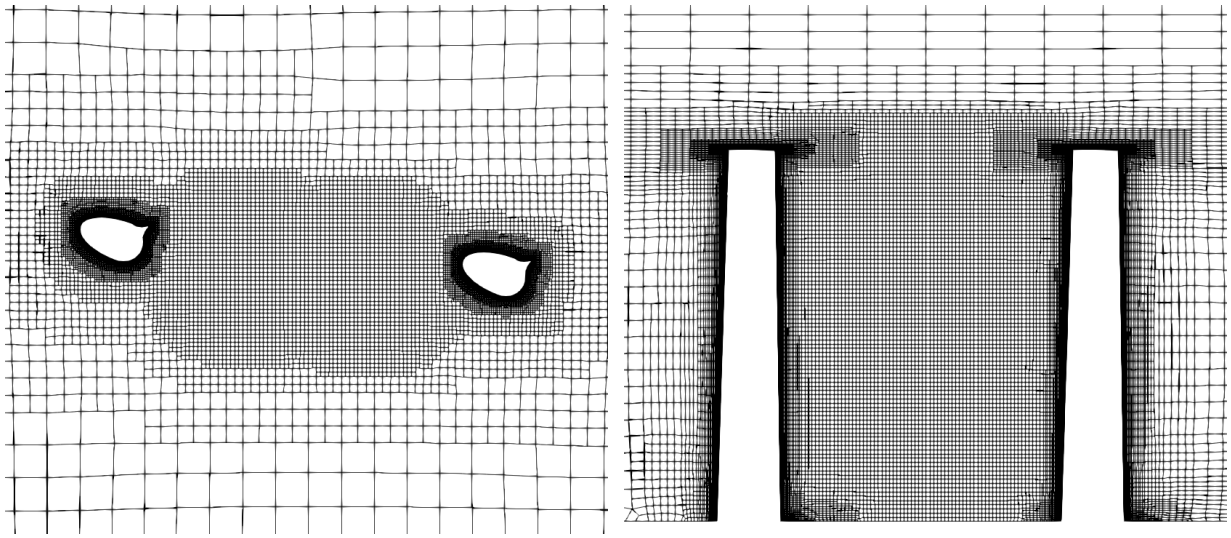

Figure 5.27: Grid refinement sectors between the VentiFoils

5.5.2 Interaction influence on forces

The interaction of two Ventifoils depends on the apparent wind direction, therefore interaction is simulated for three different apparent wind angles (β_a) of 30°, 50° and 70° which are respectively shown in Figure 5.28, Figure 5.29 and Figure 5.30. The angle of attack of the VentiFoils is kept constant at 30°. The simulations show that the windward VentiFoil causes the flow to be deflected as shown by the streamlines. This causes

the angle of attack of the downwind VentiFoil to decrease. This leads to a reduction in lift and an increase in drag. These effects are more significant for small apparent wind angles because the wake of the windward VentiFoil is closer to the downwind VentiFoil in these conditions. These results are shown in Table 5.2.

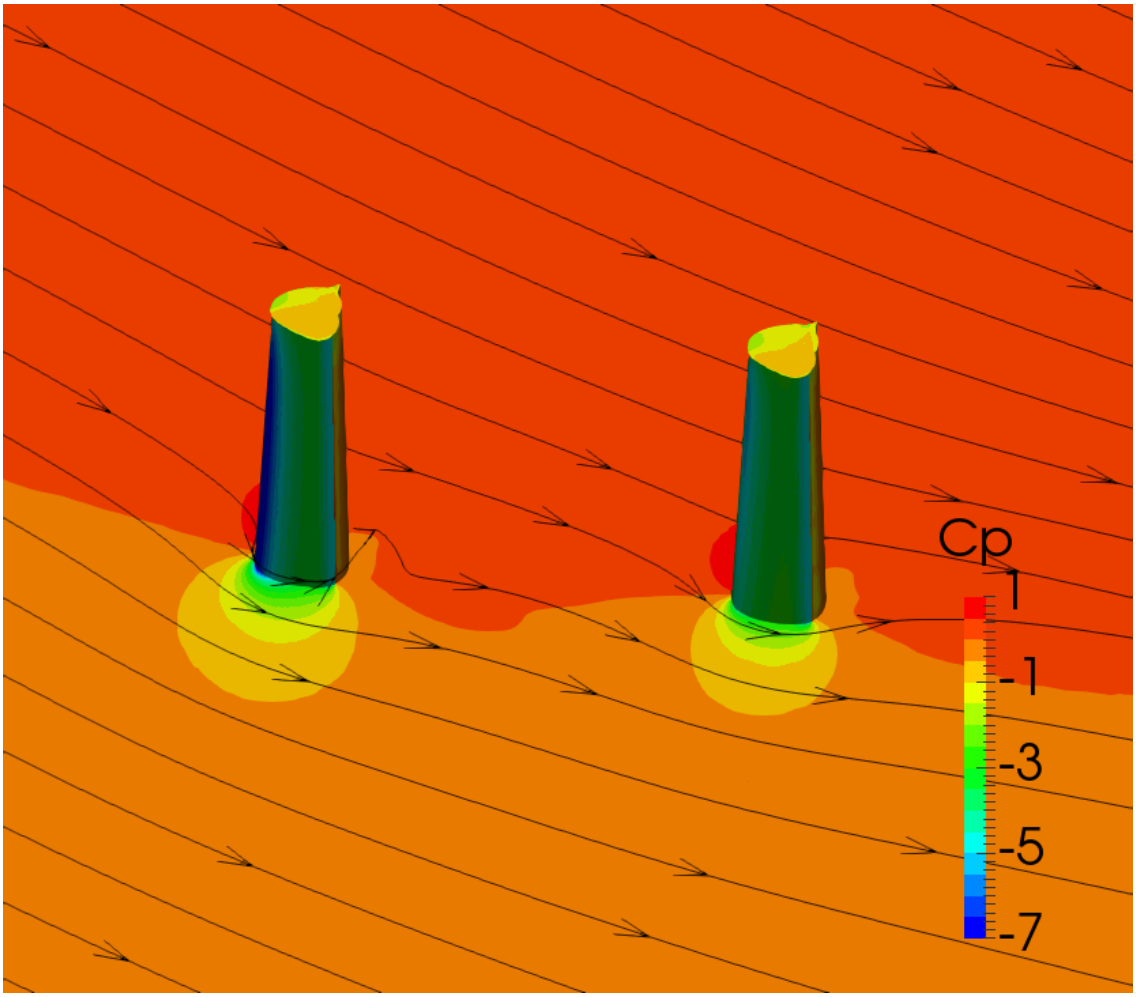

Figure 5.28: Interaction between two VentiFoils at $\alpha = 30°$ and $\beta_a = 30°$, the ship is moving left

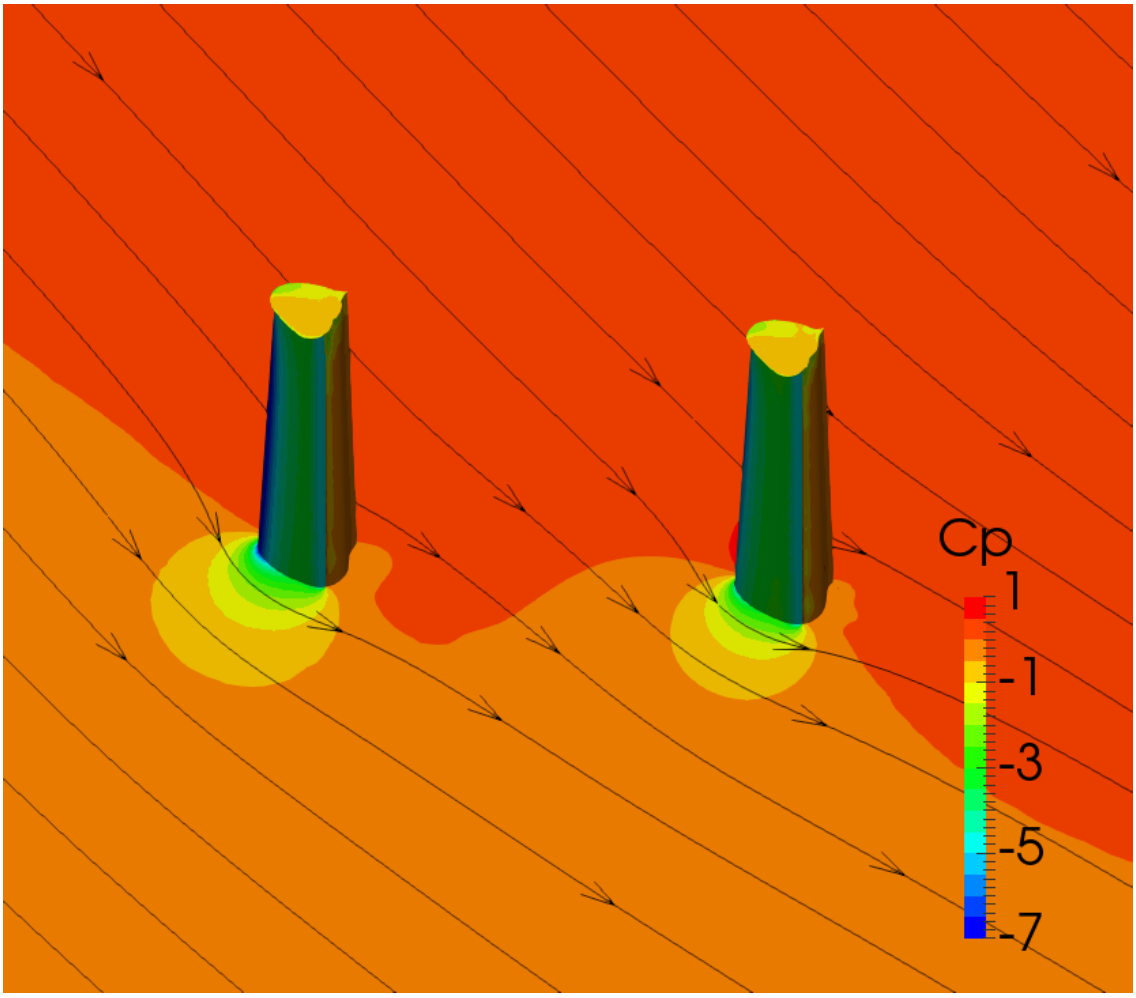

Figure 5.29: Interaction between two VentiFoils at $\alpha = 30°$ and $\beta_a = 50°$, the ship is moving left

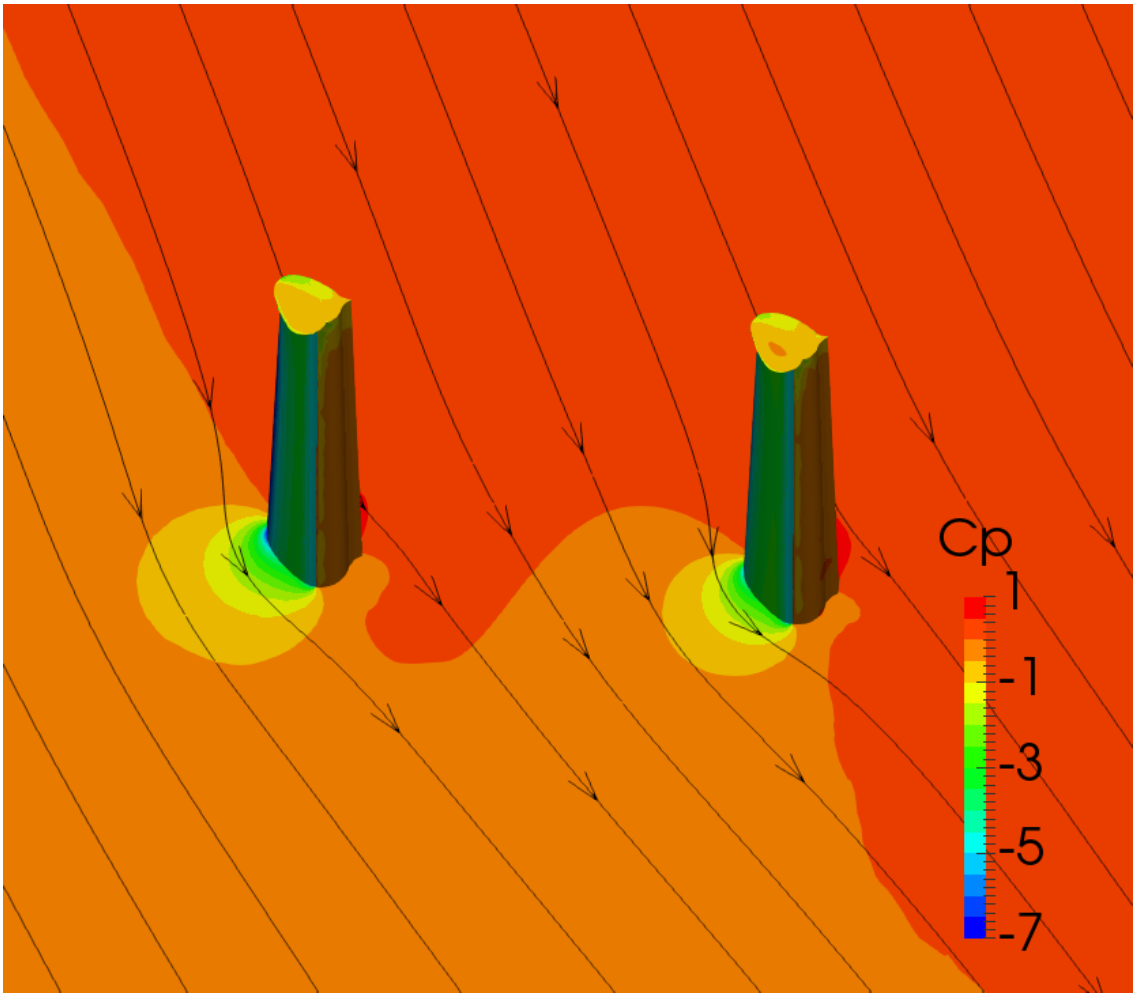

Figure 5.30: Interaction between two VentiFoils at $\alpha = 30°$ and $\beta_a = 70°$, the ship is moving left

Table 5.2: Results of lift and drag coefficients for different apparent wind angles, not all C_q values are the same, $C_q \approx 0.054$

β_a [°]	30		50		70	
	C_L	C_D	C_L	C_D	C_L	C_D
Windward	4.53	0.96	4.58	1.02	4.52	1.05
Downwind	3.77	1.29	3.93	1.23	3.95	1.13
difference [%]	-16.7	34.7	-14.3	20.8	-12.6	7.7

Chapter 6

Improved configuration

Based on the knowledge gained in the 2D parameter variation of chapter 4 and the 3D simulations of chapter 5, a best guess estimate is made to improve the geometry of the VentiFoil in order to obtain more performance. This improved geometry is compared to the base geometry.

6.1 Geometry changes

The changes of the geometry are based on the investigated parameters from chapter 4 and chapter 5 and the evaluated pressure profiles around the VentiFoil. These chapters describe geometry variations and their corresponding effect on the performance of a VentiFoil. Changes to the section profile are used to improve the geometry.

6.1.1 Flap

As evaluated in subsection 4.5.1, the influence of the flap angle at a suction coefficient of 0.04 is small for flap angles from 28.5 to 57 degrees. Based on the results from Figure 4.18, a flap angle of 45[°] is selected for the improved geometry. This flap angle performs good at angles suction coefficients above 0.4 and does not significantly reduce in performance for lower suction coefficients.

As evaluated in subsection 4.5.2, an increase of the flap length provides a clear improvement of the performance for all suction coefficients. Because the VentiFoils has to be able to fold inside the 40[ft] container, the dimensions of the flap are limited and cannot be increased with respect to the full scale base geometry. Therefore the length of the flap is unchanged.

The geometry of the flap of the base geometry consists of multiple straight sections. In order to improve the curvature on the windward side of the flap, the flap geometry is changed to the shape of a circle segment.

6.1.2 Leading edge shape

As evaluated in subsection 4.5.3, the application of a leading edge with the shape of a cubic Bezier curve with smaller curvature provides a slight improvement in performance for all suction coefficient compared to an elliptical leading edge. The performance increase is largest at larger suction coefficients .

6.1.3 Thickness ratio and taper

The effect of the thickness ratio and taper is evaluated in subsection 4.5.4 and subsection 4.5.5. This study concluded that the performance of the eConowind unit can be improved by applying less taper. To be able to do this and fit both VentiFoils in the container, the thickness ratio should be reduced.

In order to provide a fair comparison with the base geometry, the thickness ratio and taper are not changed for the improved geometry.

6.1.4 Suction

The suction width is investigated in subsection 4.5.6. This study shows that a larger suction extend improves the performance at suction coefficients above 0.4. Therefore a suction width of 20[°] is selected for the improved geometry.

The location of the suction region is investigated in subsection 4.5.7. This investigation shows that the location of the suction region has the most significant influence on performance. Moving the suction region further towards the trailling edge can lead to significant performance increases. When the suction region is too close to the trailling edge, the VentiFoil becomes sensitive to stalling. To prevent the VentiFoil from stalling at these large angles, large suction coefficients are required. A suction location of 45[°] is selected for the improved geometry. This suction location should increase the produced forces and is located at the same position of the flap such that the windward suction region is sealed.

6.1.5 End plate

In order to make a fair comparison between both configurations, the end plate geometry is not changed.

The end plate position is studied in subsection 5.4.3. This investigation shows that the best location to apply the end plate is above the suction side to seal the low pressure region. Therefore the location for the improved configuration is also at the leeward side.

6.1.6 Improved geometry

The changes of the improved configuration with respect to the base geometry are only changes of the section profile. The parameters of the base and improved geometries are shown in Table 6.1. These changes are also shown in Figure 6.1.

Table 6.1: Parameters of the base and improved geometry

geometry	Base	Improved	Unit
s	10.25	10.25	m
c_{top}	1.372	1.372	m
c_{bottom}	1.887	1.887	m
h/t	ellipse	0	-
t/c	0.609	0.609	-
L_F/c	0.145	0.145	-
β	52	45	°
θ	14	24	°
θ_m	68.8	45	°

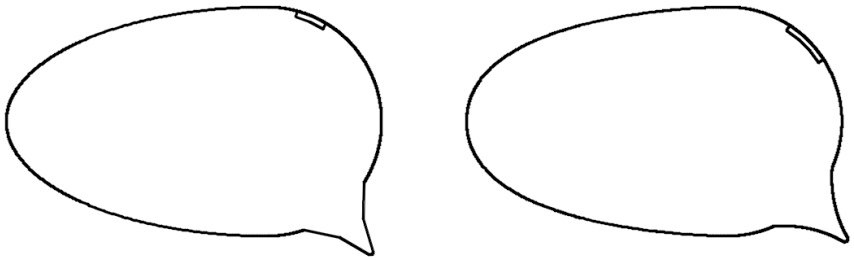

Figure 6.1: Midsections of the base geometry left and the improved geometry on the right

6.2 Forces

The base and improved configuration are compared based on the resulting forces for the same suction coefficient. The lift and drag forces are used to calculate the thrust and average thrust in order to make a performance comparison between the configurations.

6.2.1 Lift and drag

The results of the improved geometry are compared with the original full scale base geometry. The difference in results is shown in Figure 6.2. This shows that the improved geometry generates more lift and drag. This is mainly due to the change in suction location which is moved further aft for the improved geometry. Because the low pressure region now extends further along the suction side, the pressure in this region contributes to the increase in lift and drag.

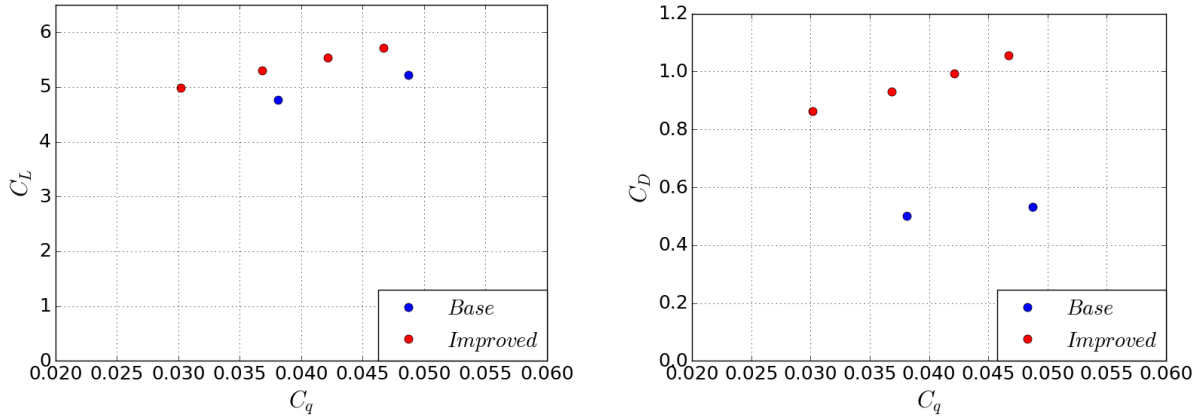

Figure 6.2: Lift and drag force coefficients

To fairly compare both configurations, the lift and drag at C_q of 0.04, obtained by linear interpolation of the results shown Figure 6.2. This results in the force coefficients as shown in Table 6.2.

Table 6.2: Lift and drag coefficients for the base and improved geometries ar $C_q = 0.04$

Geometry	Base	Improved	Increase %
C_L	4.85	5.44	12.2
C_D	0.507	0.969	91.1
C_T	4.87	5.52	13.3

6.2.2 Thrust

To evaluate which geometry provides more thrust in different apparent wind directions, the thrust coefficient is plotted against the apparent wind angle as shown in Figure 6.3. This figure shows that the original base geometry provides more thrust for small apparent wind angles and from 37.8 [°], the improved geometry provides more thrust. The maximum absolute increase in thrust for the improved geometry is at 128[°] with an increase in thrust coefficient of 0.751. The maximum relative increase is at 180[°] with 91% more thrust because in this condition only the drag force provides thrust.

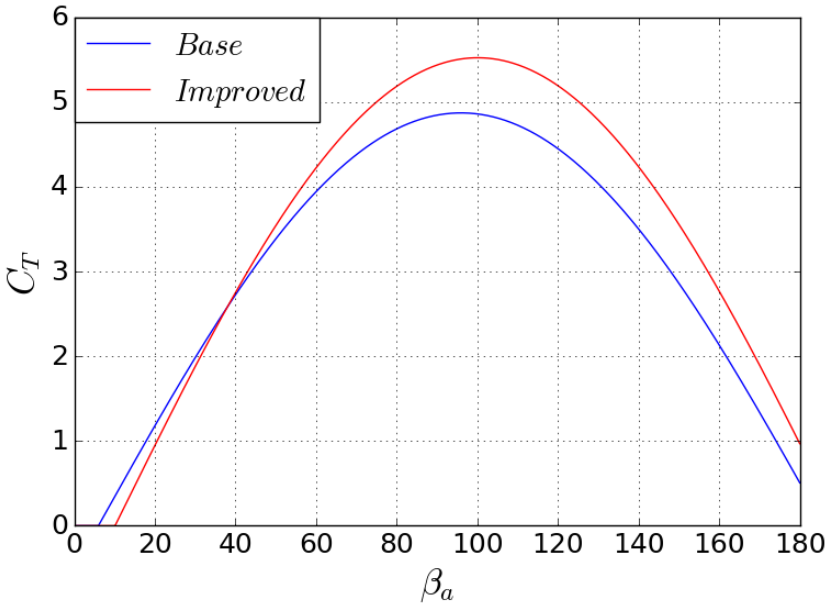

Figure 6.3: Thrust coefficient for all apparent wind angles

6.2.3 Average thrust

To provide a fair comparison, the average thrust is evaluated based on the thrust coefficient multiplied with the probability of occurrence of a certain apparent wind angle as also used in section 4.4. These results are shown in Figure 6.4.

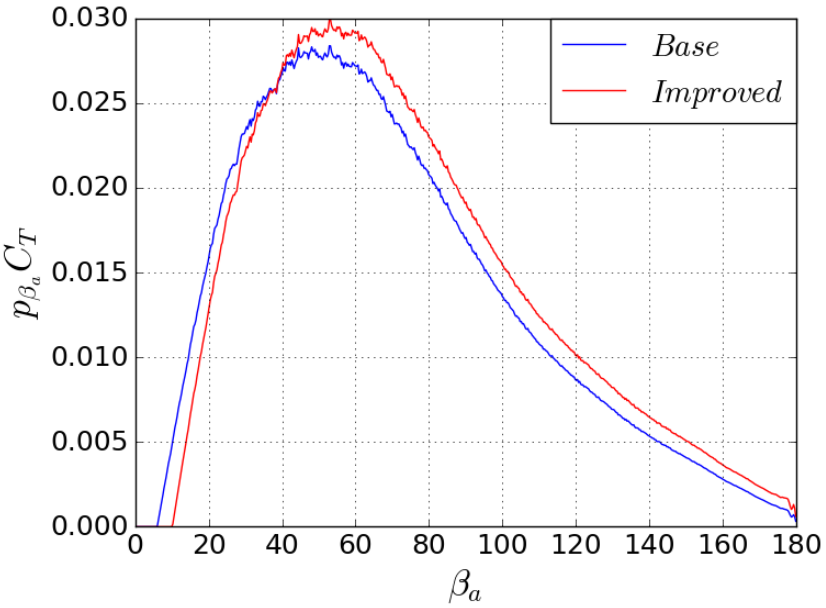

Figure 6.4: Thrust coefficient multiplied with the probability of occurrence of apparent wind angles for all apparent wind angles

Integration of Figure 6.4 results in the average thrust coefficients which is a good parameter to compare the performance. The average thrust obtained from the base geometry is 2.49, the average thrust obtained from the improved geometry is 2.54. Therefore the improved geometry will on average produce 5.2% more thrust compared to the base geometry.

6.3 Conclusion

By making a best guess estimate for an improved geometry, the lift and the drag of the VentiFoil are increased. This results in an average performance increase of 5.2%. At apparent wind angles below 37.8 [°], the thrust of the improved geometry is less than the thrust provided by the base geometry. This is more than compensated by the increased thrust at apparent wind angles larger than 37.8 [°].

Chapter 7

Conclusions and recommendations

The working principles and performance of VentiFoil wind propulsion has been investigated using 2D and 3D steady RANS CFD simulations to investigate the influence of geometric VentiFoil parameters variations on performance. This chapter describes theconclusions of this investigation and provides recommendations for the design of the VentiFoils and for further research.

7.1 Conclusions

The investigation of VentiFoil wind propulsion has lead to a better understanding of the VentiFoil concept and the insight that the application of boundary layer suction is the most significant parameter.

The section shape has been investigated to provide insight into the influence and significance of geometric section parameters.
This has lead to the observations that the larger flap angles are generally better although the significance of the flap angle is small provided that the flap angle is sufficient to induce separation at the tip.
The length of the flap has been found to have a more significant influence on performance whereby larger flap lengths provide more performance. The shape of the leading edge turns out to have a slight influence on performance whereby leading edges with a larger minimum curvature perform better. When the minimum curvature at the leading edge is large, the VentiFoil becomes more sensitive to stall.
A larger thickness ratio has been found to have a significant positive influence on performance. However because the total VentiFoil surface area fitted inside an eConowind unit has a more significant influence in performance. The best performance can be achieved by fitting VentiFoils with maximum with and without taper in the eConowind unit.
The width of the suction turns out to have a slight influence on performance whereby a larger suction width provides more performance.
The location of the suction region has been found to have a significant influence on performance whereby moving the suction region further aft has a positive influence on performance however this also makes the VentiFoil more susceptible for stall when the applied suction is insufficient.

The influence of the tip effects has been investigated in order to provide insight in the tip losses and the effect of an end plate on the generated forces.
In order to evaluate the influence losses due to tip effects, a span variation study is conducted. This study provided the insight that the 3D results tend towards the 2D results for increasing span.
The application of an end plate can be used to reduce tip losses but because the size limitations of the end plate in order to be folded inside the container, the advantage of the evaluated end plate configurations is limited. The location of the end plate has been investigated. This investigation shows that the application of the end plate on leeward side has the largest benefit to increase the lift and reduce the drag. The application of two end plates on leeward and windward provides slightly lower drag but does not provide a significant advantage compared to only one plate on leeward.

The interaction investigation found that the influence of the windward VentiFoil has a significant influence

on the downwind VentiFoil due to the deflected airflow in the wake of the Windward VentiFoil. This effect has been found to be most significant for small apparent wind angles because the wake of the windward VentiFoil is closer to the downwind VentiFoil.

7.2 VentiFoil recommendations

Based on the investigation of the performance of VentiFoils, recommendations can be made to improve the the VentiFoil design. A best guess improved geometry is investigated in chapter 6 which provided a performance increase of 5.2% on the average produced thrust. This performance increase case for this configuration is based on the change of section profile parameters. When other parameters are adjusted, the VentiFoil performance can be increased even more.

The end plate configuration covers the leeward side with the center of rotation close behind the leading edge. This provides only a small overhang of the end plate at the location of lowest pressure. The efficiency of the end plate could possibly be increased if the end plate would extend further over the low pressure region. This can be achieved without increasing the size of the end plate by placing the rotation closer towards the trailling edge. This provides an interesting configuration to investigate.

This study is conducted with the assumption that the VentiFoils are fitted inside an eConowind unit, therefore the VentiFoils have to be able to fold inside a 40 foot container. This results in some geometric limitations for the thickness ratio, the flap size and the end plate geometry. If these limitations would be removed, a possible increase in performance can be realized. If there were no container limitations, the length of the flap, the thickness ratio and taper ratio, the span and the size of the end plate could be increased. All these changes can contribute to an increase of performance and without container limitations. This would allow for the application of VentiFoil propulsion on a larger scale. Therefore this provides an interesting case to investigate.

7.3 Recommendations for further research

This study concluded that the location of the suction region has a significant influence on the generated forces and therefore on the performance. The suction location also determines the required suction intensity in order to prevent stall. Because the influence of the suction location is significant, this provides an interesting parameter for further investigation because the potential performance gains are significant.

For continuation of the VentiFoil research there are uncertainties about the correlation between the results from the CFD simulations and the experimental results. Therefore validation of the results with experimental test data would be an important next step.

The generated forces as well as the required suction coefficients and the relation with stall provide interesting parameters to investigate experimentally.

The relation between the suction coefficients and the required suction power also provides an interesting relation to investigate. This can be used to provide a performance evaluation where the required suction power is included in the performance evaluation. The performance can then be evaluated based on the net propulsive power instead of on the average thrust coefficient which does not include the required fan power.

The suction is the essential working principle of the VentiFoil. Therefore the application of suction provides an interesting parameter to investigate. The size and configuration of the holes could influence performance. Because the fan is located at the bottom, the suction pressure will not be distributed exactly evenly over the span of the VentiFoil due to pressure losses. This can therefore have an influence on the suction coefficient over the height. The influence of this effect is assumed small because the resistance of the flow through the inside of the VentiFoil is small with respect to the resistance over the holes. This effect might have some influence and can be interesting to investigate.

Bibliography

[1] J. Cousteau A. Daïf L. Malavard Y. Quinio B. Charrier, J. Constans. Fondation cousteau and windship propulsion. *Journal of Wind engineering and Industrial Aerodynamics*, 20:39–60, 1985.

[2] A. Molland B. Moat, M. Yelland. Quantifying the airflow distortion over merchant ships. part ii: Application of the model results. *American Meteorological Society*, 2006.

[3] B. Kamoun D. Afungchui C. Hcini, E. Abidi. Numerical prediction for the aerodynamic performance of turbosail type wind turbine using a vortex model. *Energy*, 109:287–293, 2016.

[4] B. Kamoun D. Afungchui C. Hcini, E. Abidi. A turbosail profile analysis code based on the panel method. *Energy*, 118:147–155, 2017.

[5] R. Eppler. Airfoils with boundary layer suction, design and off-design cases. *Aerospace Science and Technology*, 3(7):403–415, 1999.

[6] S. Winoto H. Low, S. Luo. Flow past a wind-assisted ship propulsion device. *Ocean Engng*, 18(6):555–565, 1991.

[7] Stefan Hickel. Cfd for aerospace engineers. Lecture slides, 2017.

[8] K. Ma J. Wang, J. Hu. Wind speed probability distribution estimation and wind energy assessment. *Renewable and Sustainable Energy Reviews*, 60:881–899, 2016.

[9] A. Kisjes. Wind propulsion for merchant vessels. Master's thesis, Delft University of Technology, the Netherlands, 2017.

[10] M. Hoekstra L. Eça. A procedure for the estimation of the numerical uncertainty of cfd calculations based on grid refinement studies. *Journal of Computational Physics*, 262:104–130, 2014.

[11] L. Malavard. Un nouveau propulseur éolien de navire. *Comptes rendus*, tome 1(1):57–72, 1984.

[12] A. Hamdouni O. Guerri, E. Liberge. Study of the turbulent flow aruond a turbosail. *Congrès Français de Mécanique*, 21, 2013.

[13] A. Hamdouni O. Guerri, E. Liberge. Numerical simulation of the turbulent flow around an oval-sail. *Journal of Applied Fluid Mechanics*, 9:2009–2023, 2016.

[14] D. Bridges R. Wahidi. Effects of distributed suction on an airfoil at low reynolds number. *Fluid Dynamics Conference and Exhibit*, 40, 2010.

[15] D. Gilhousen S. Hsu, E. Meindl. Determining the power-law wind-profile exponent under near-neutral stability conditions at sea. *American Meteorological Society*, 1994.

[16] T.W. Sederberg. *Computer aided geometric design*. Brigham Young University, Department of Computer Science, 1016.

[17] A. Fujii T. Shiii, H. Yagi. Wind tunnel study of column-type circular cylinder propulsion assistance system (c-pas) for ships. *The Fourth International Symposium on Computational Wind Engineering*, 2006.

[18] Z. Chen Q. Tang W. Zhang, Z. Zhang. Main characteristics of suction control of flow separation of an airfoil at low reynolds numbers. *European Journal of Mechanics B/Fluids*, 65:88–97, 2017.

Appendices

Appendix A

Container fit

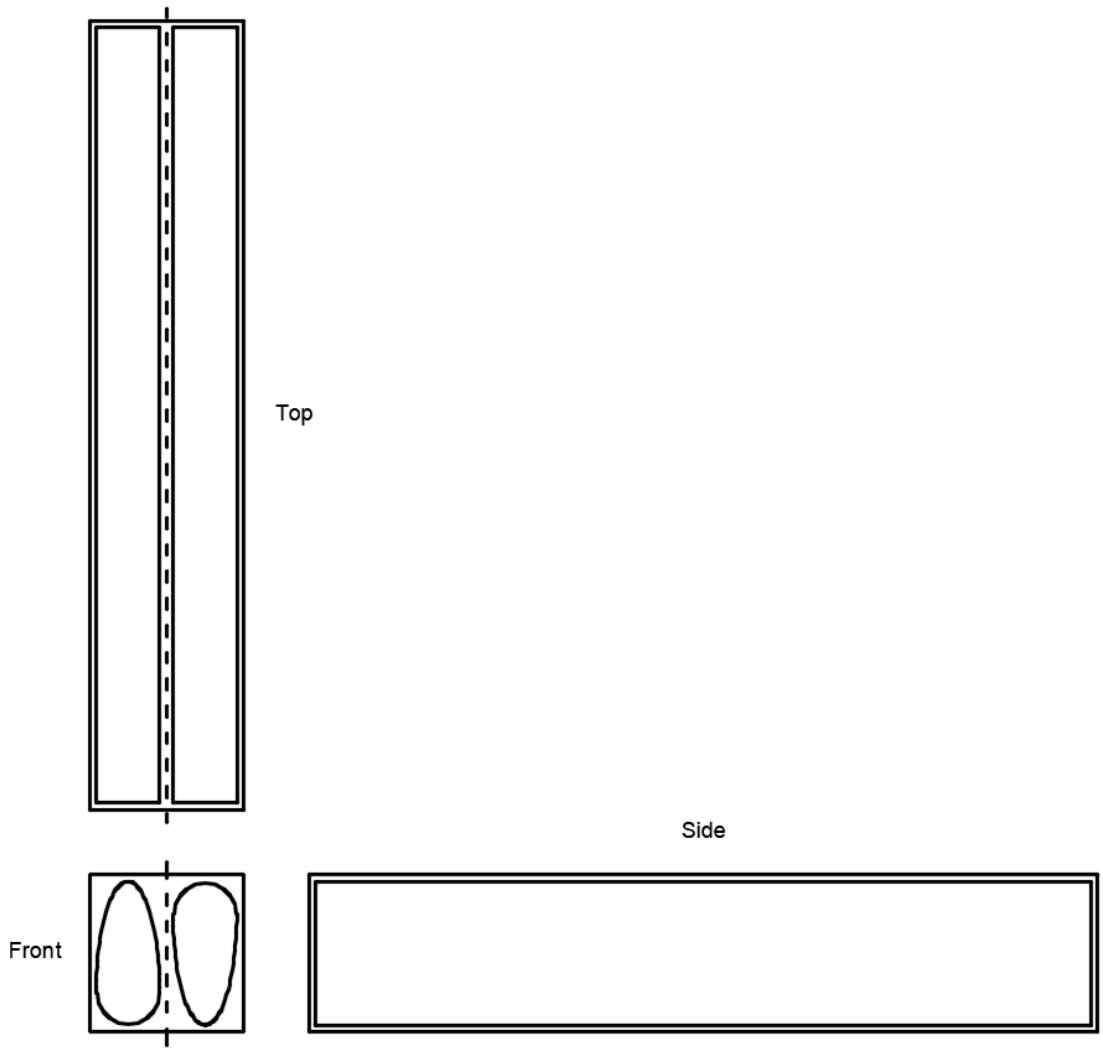

Figure A.1: Schematic container fit $\frac{t}{c} = min$

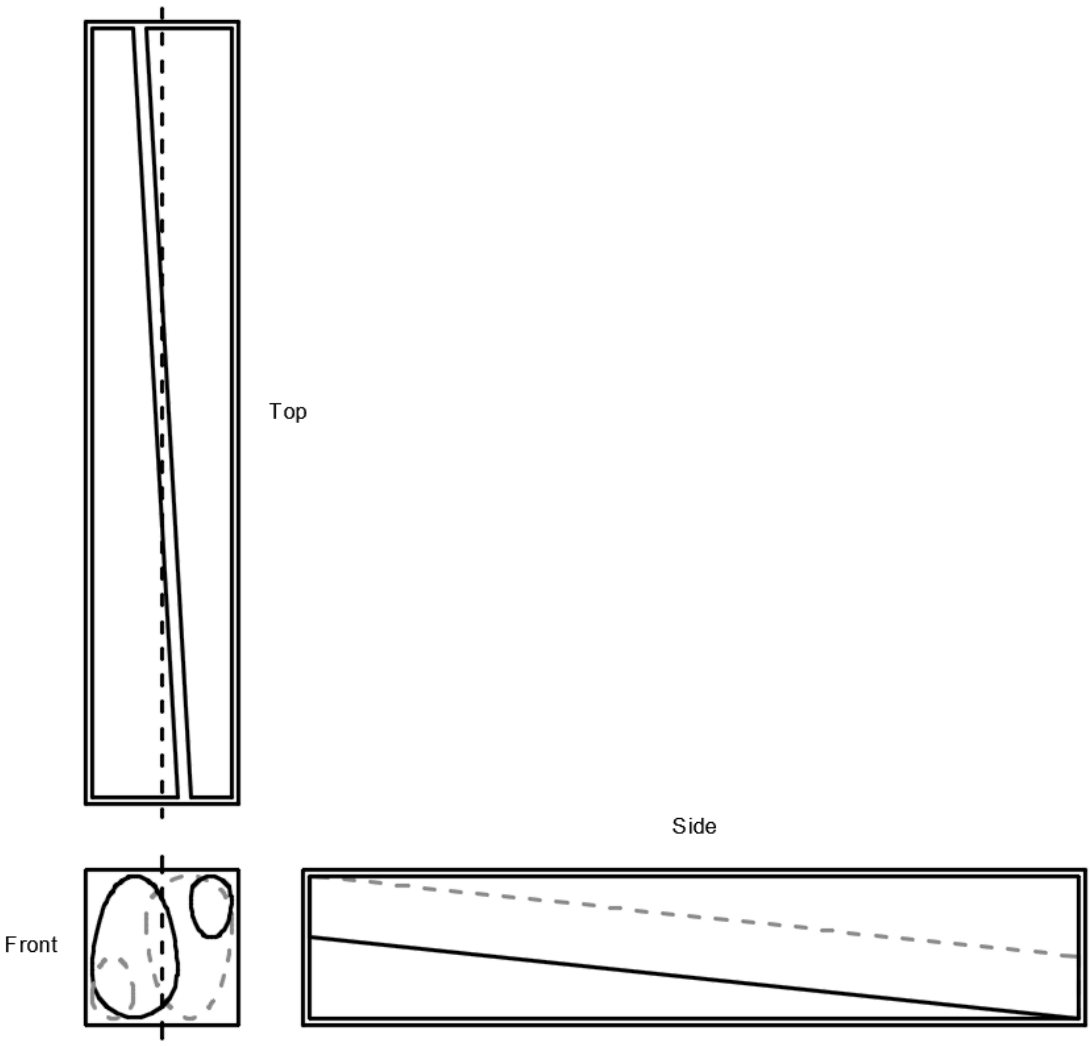

Figure A.2: Schematic container fit $\frac{t}{c} = 0.6$

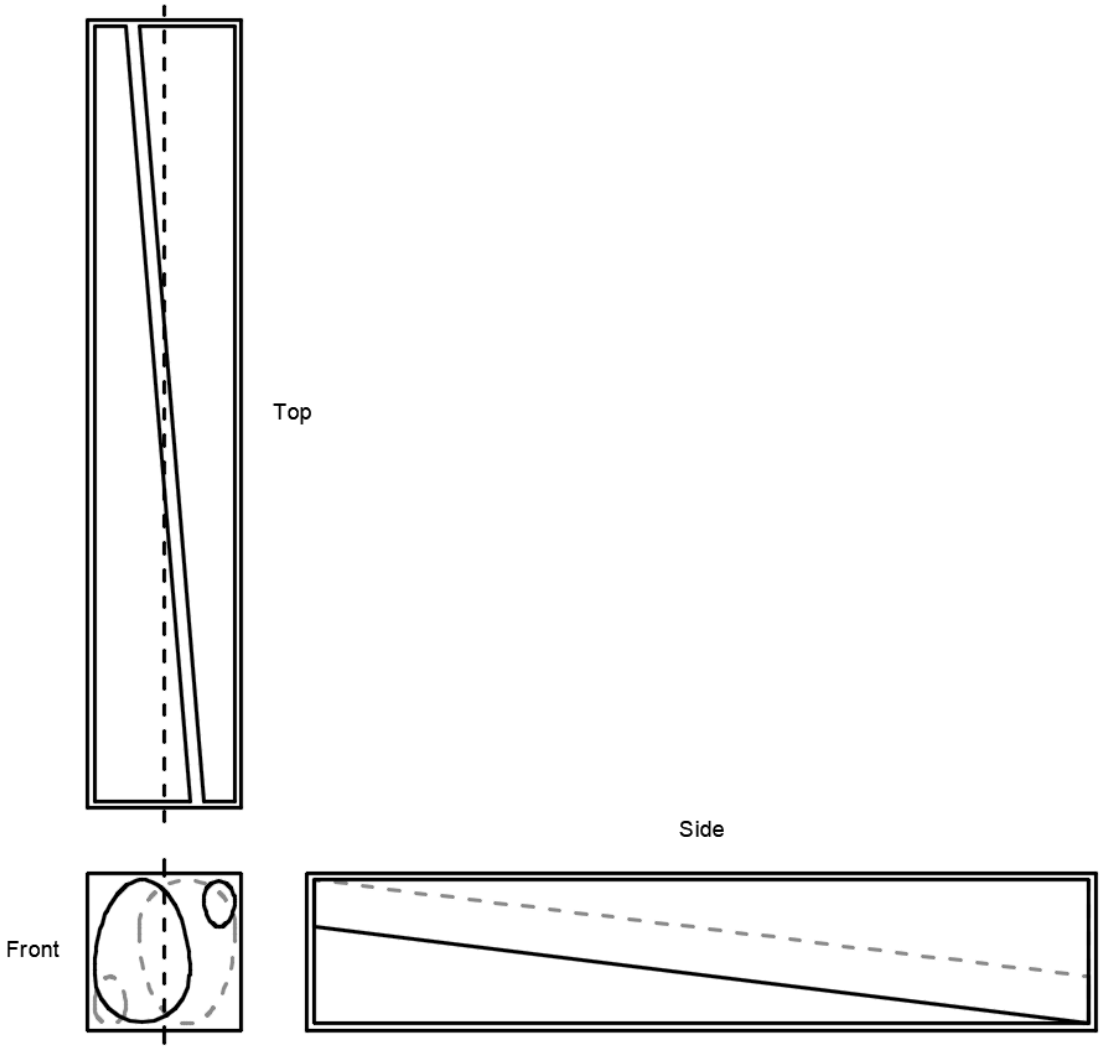

Figure A.3: Schematic container fit $\frac{t}{c} = 0.67$

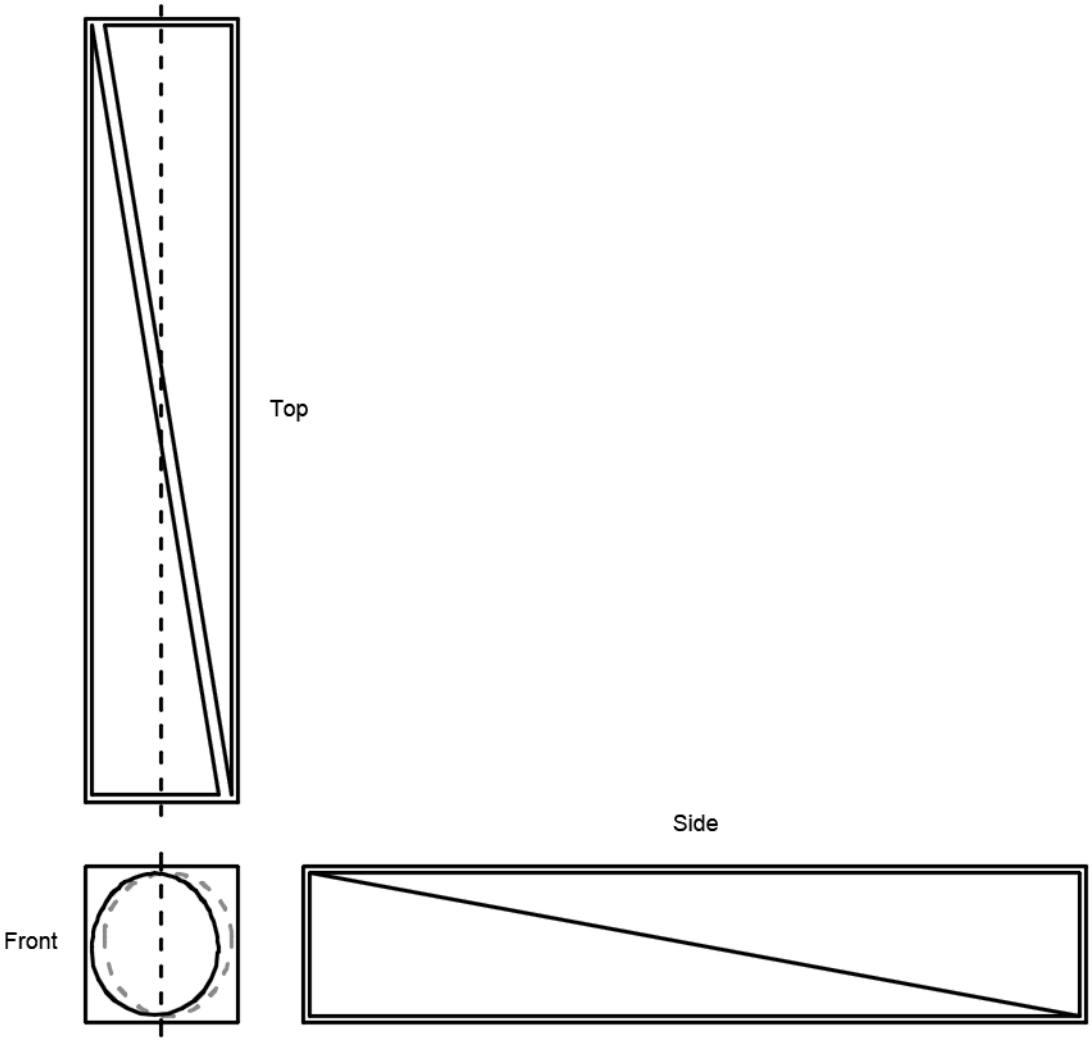

Figure A.4: Schematic container fit $\frac{t}{c} = max$

Appendix B

Geometrically similar grids

B.1 Full grids

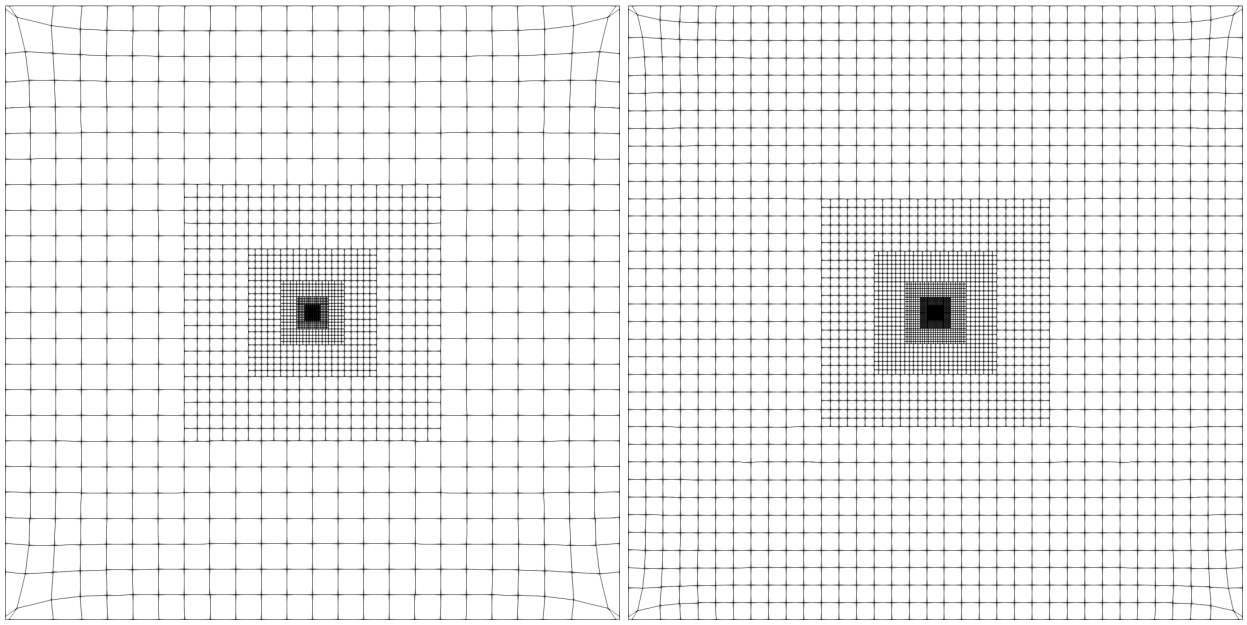

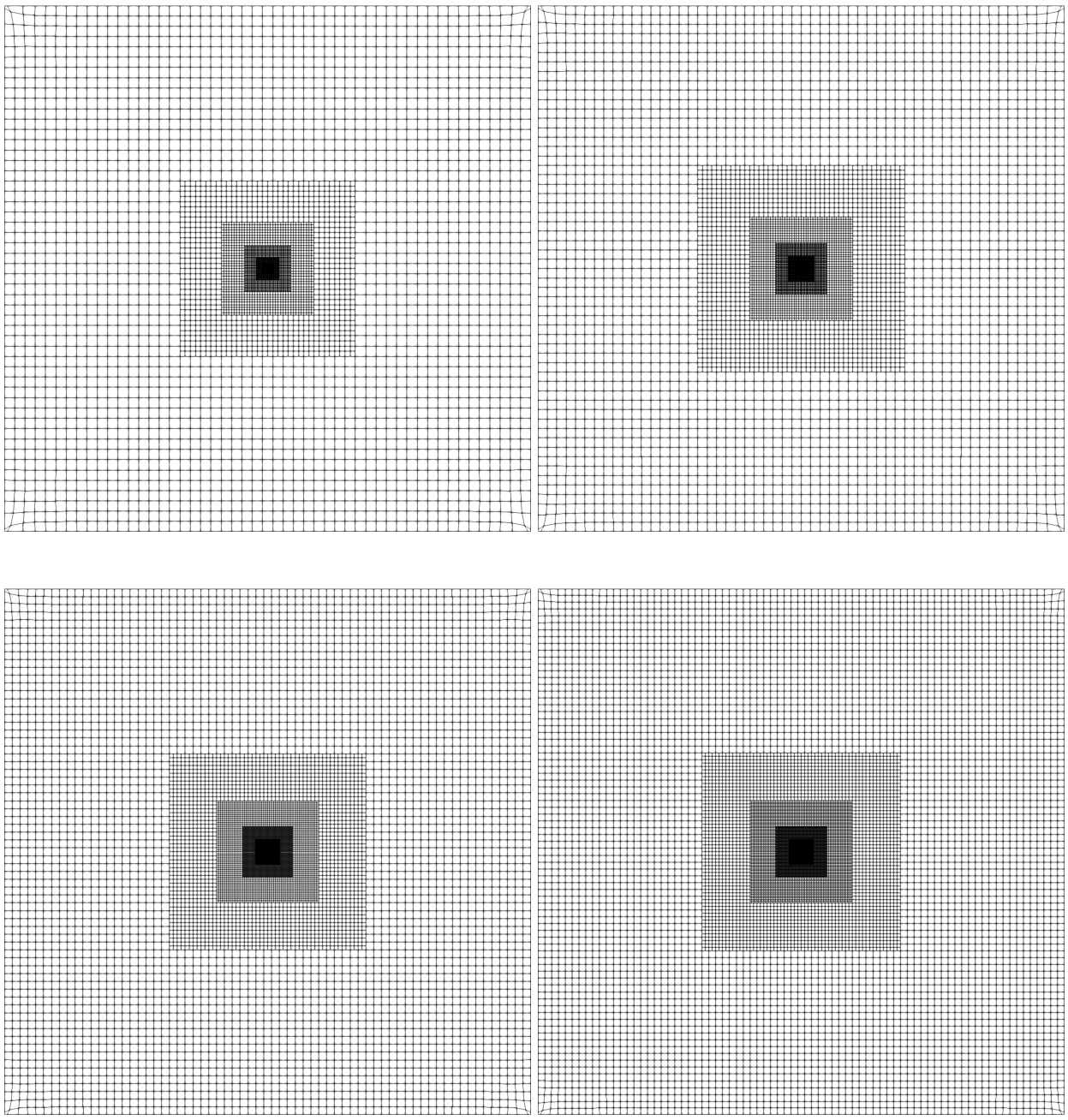

Figure B.1: Full overview of geometrically similar grids with different refinement

B.2 Zoomed grids

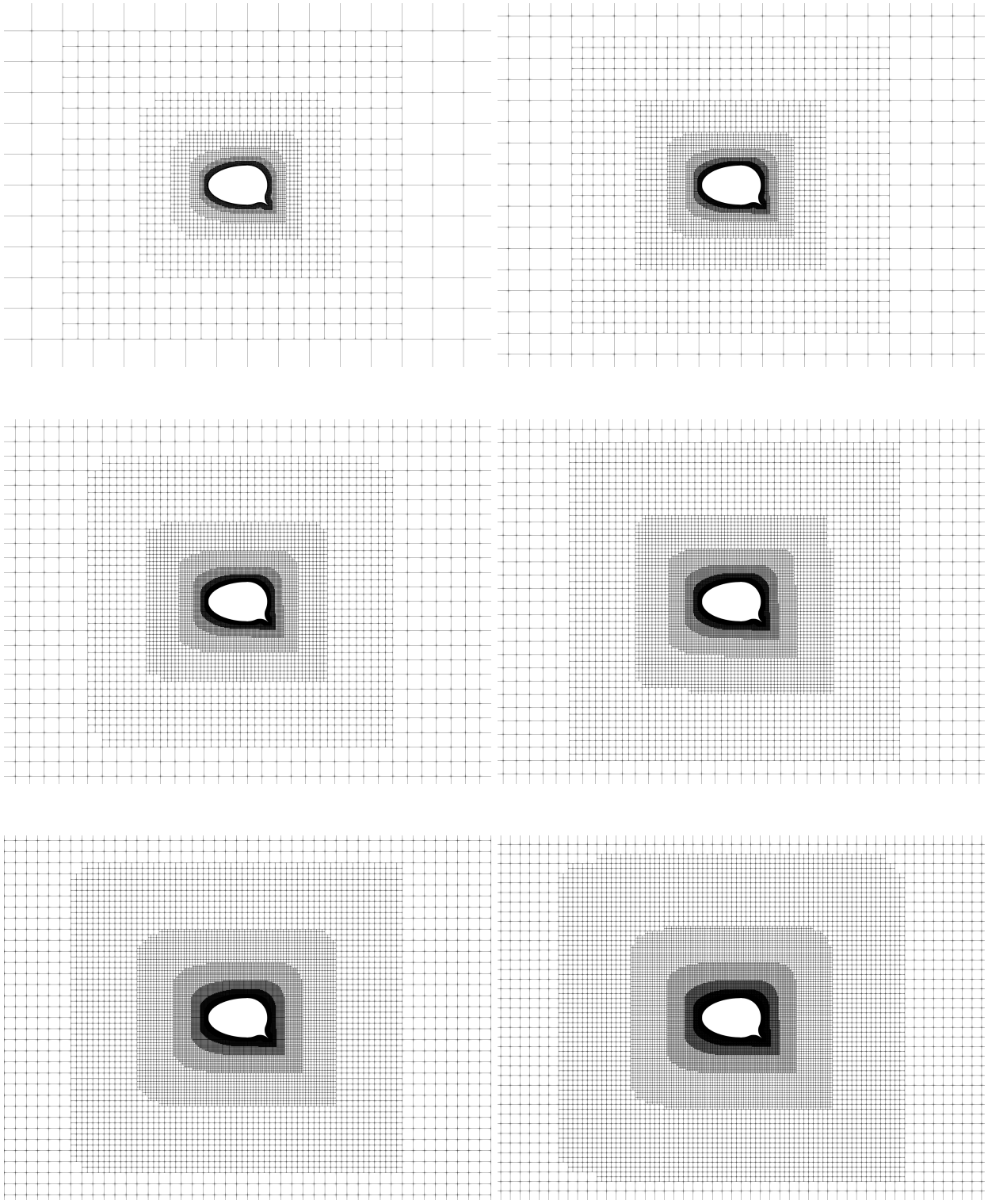

Figure B.2: Zoomed view of geometrically similar grids with different refinement

B.3 Boundary layers refinements

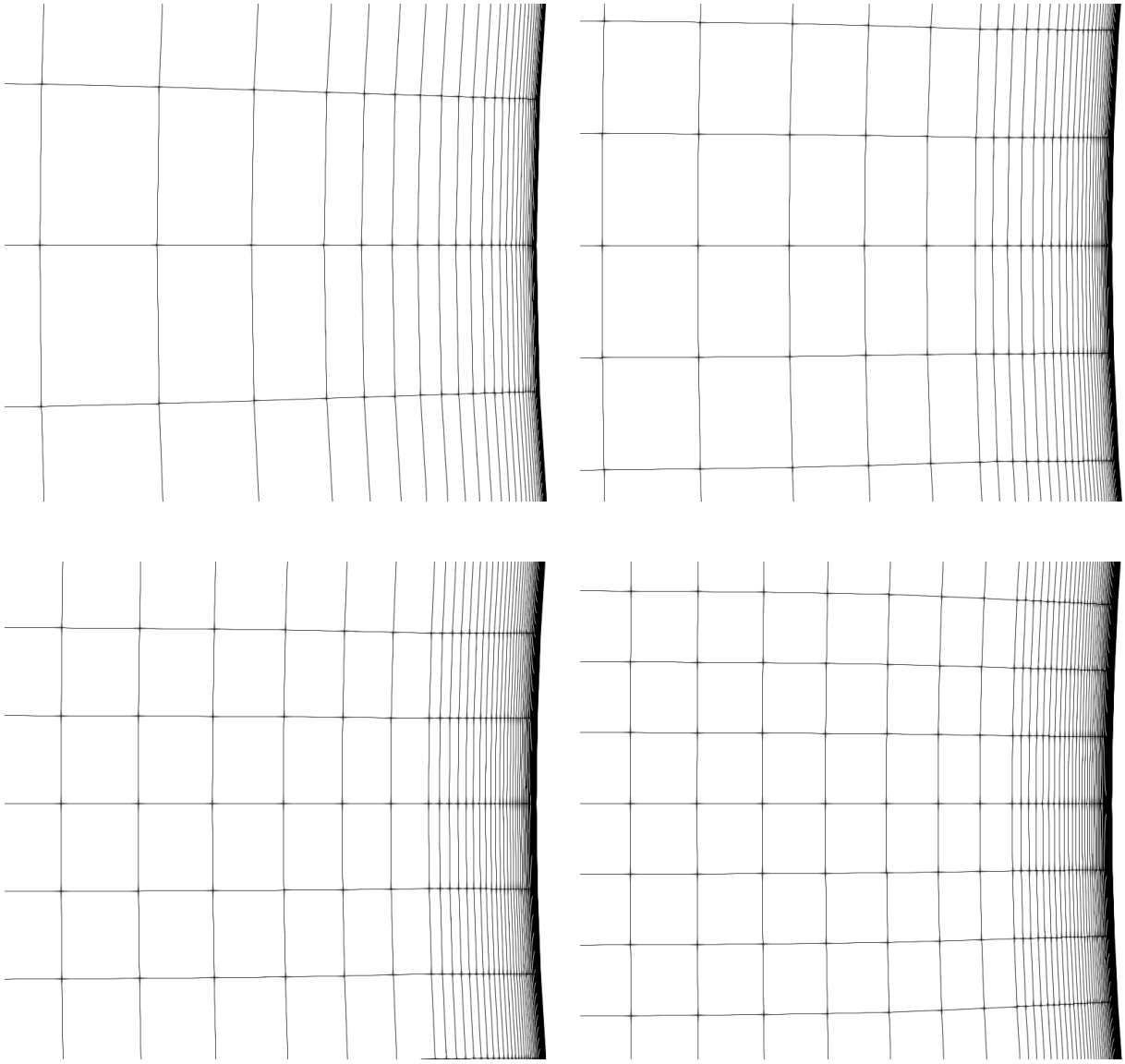

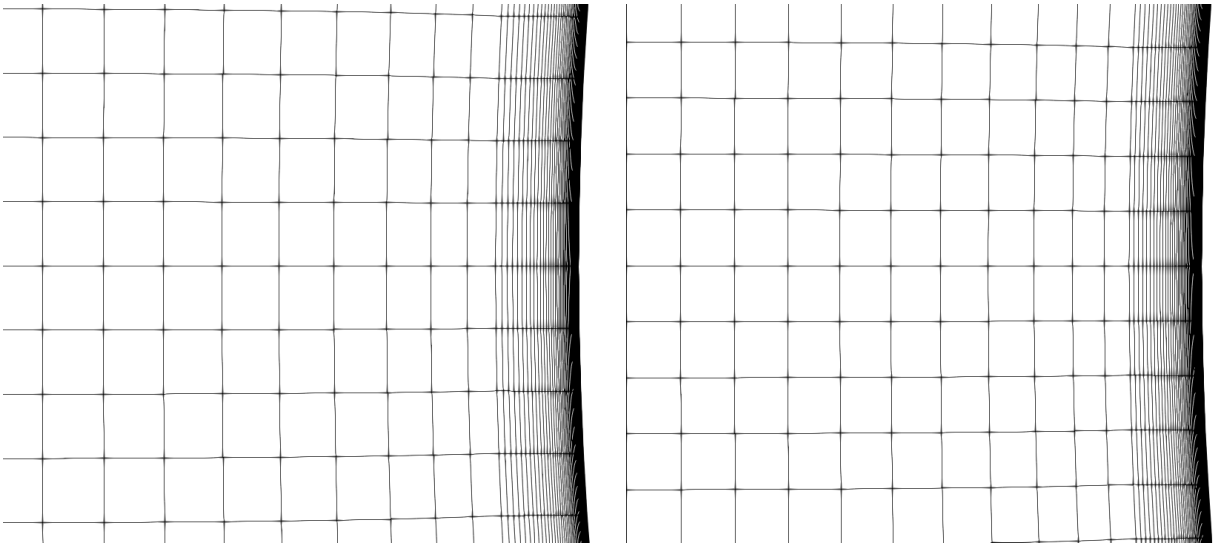

Figure B.3: Boundary layer refinement of geometrically similar grids with different refinement

Appendix C

Fitted force surfaces

The results of all evaluated 2D geometries in 36 different operating conditions are used to fit an analytically described quadratic surface which is used to compare the performance of different geometries. As specified in section 4.1. The section parameters of the geometries are specified using the code as shown in Figure C.1 whereby each number refers to a parameter setting. All geometries have a chord length of 1.63[m] as specified by the midsection of the base geometry in Table 1.3. Therefore the characteristic area (A) of all profiles is the same. The thickness of the tip of the flap is also kept constant at $t_{tip}/c = 0.0128$ which approximately corresponds to a thickness of 2[cm]. For every section in this appendix, one section parameter is varied while the rest of the parameters remains unchanged.

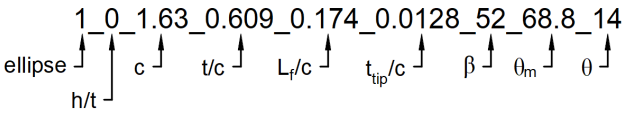

Figure C.1: Shape parameters of the 2D base geometry

C.1 Flap angle variation

Variation in β.

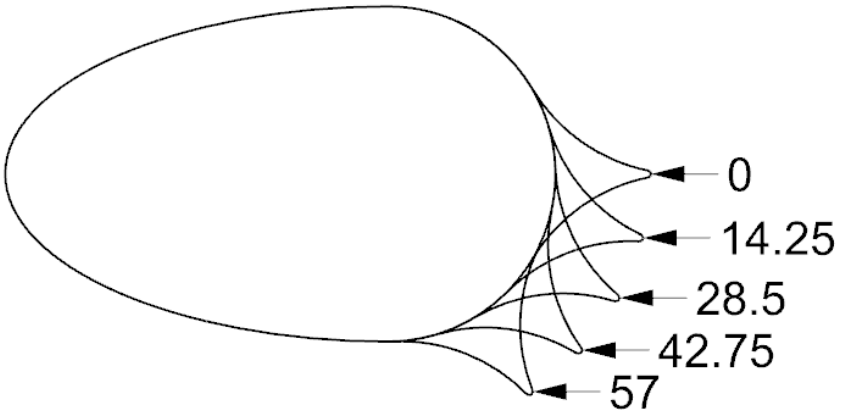

Figure C.2: Configurations β variation

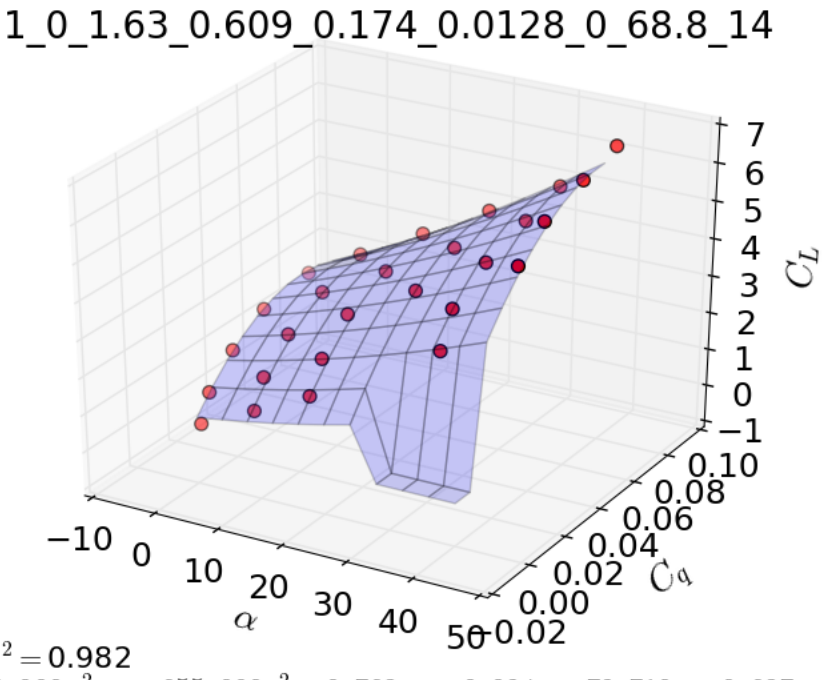

$R^2 = 0.982$

$C_L(x, y) = 0.000x^2 + -655.090y^2 + 0.763xy + 0.024x + 72.710y + 0.637$

Figure C.3: Surface fit C_L for β=0

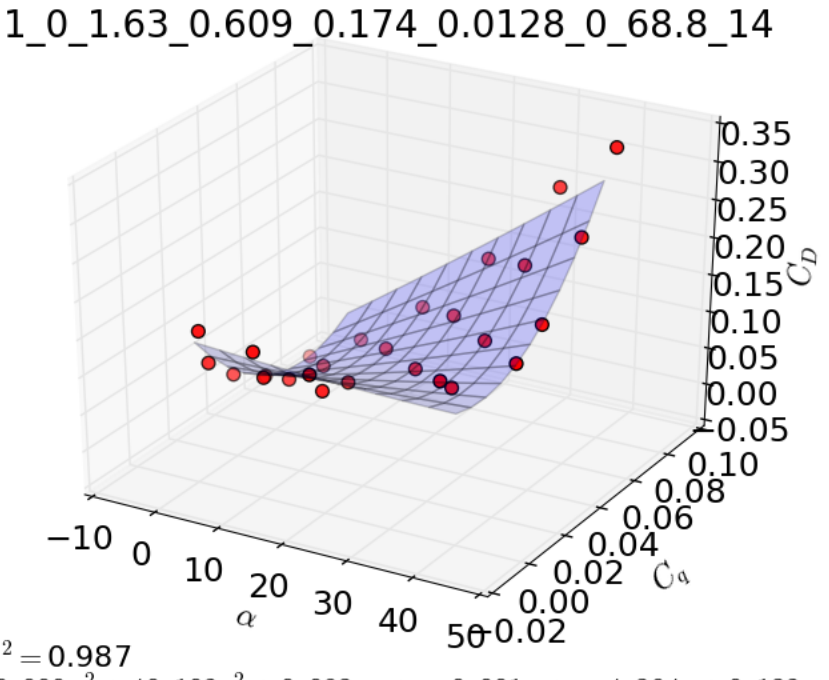

$R^2 = 0.987$

$C_D(x, y) = 0.000x^2 + 40.102y^2 + 0.083xy + -0.001x + -4.394y + 0.132$

Figure C.4: Surface fit C_D for β=0

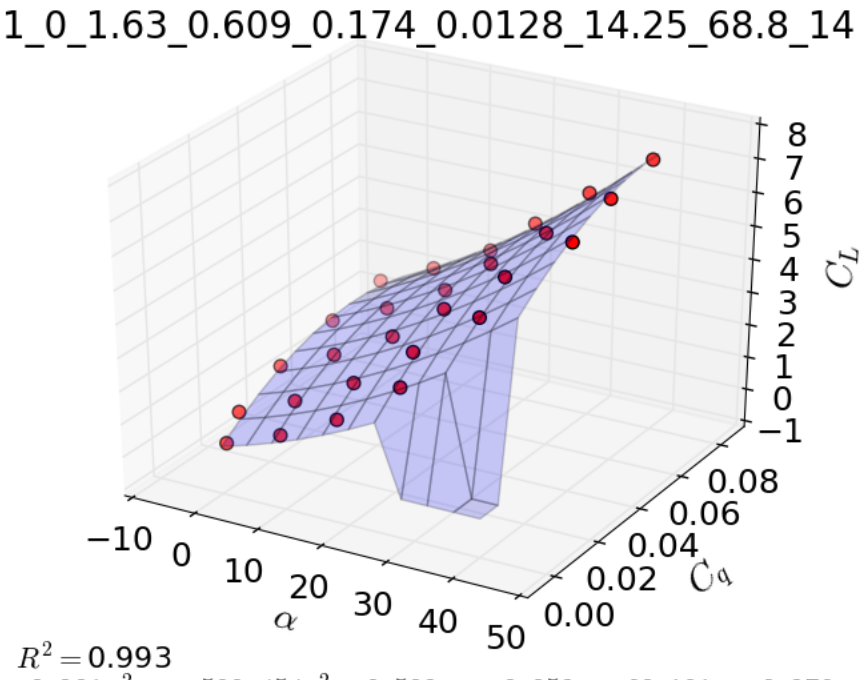

$R^2 = 0.993$

$C_L(x, y) = 0.001x^2 + -509.454y^2 + 0.502xy + 0.052x + 60.181y + 0.276$

Figure C.5: Surface fit C_L for β=14.25

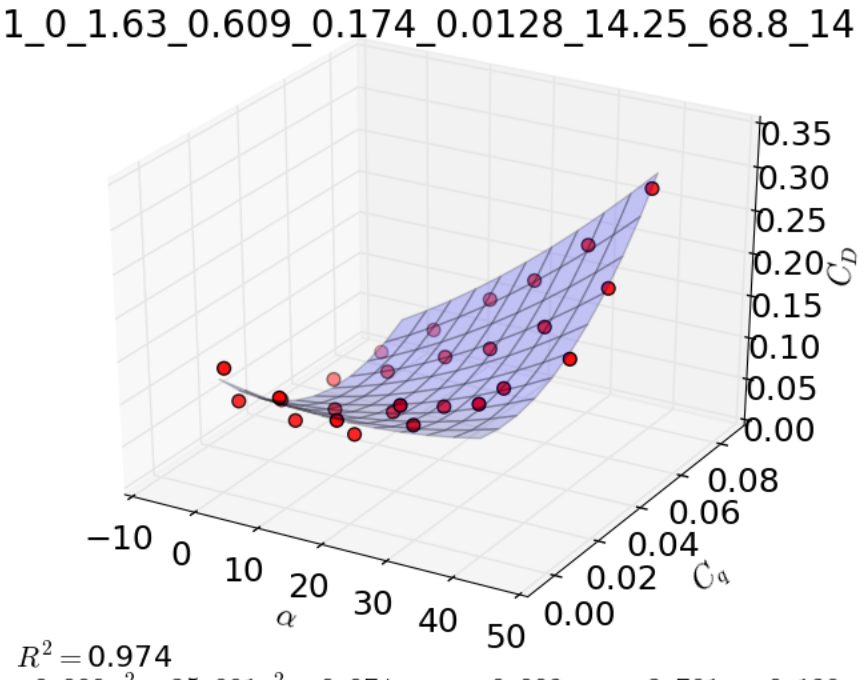

$R^2 = 0.974$

$C_D(x, y) = 0.000x^2 + 35.991y^2 + 0.074xy + -0.002x + -3.781y + 0.128$

Figure C.6: Surface fit C_D for β=14.25

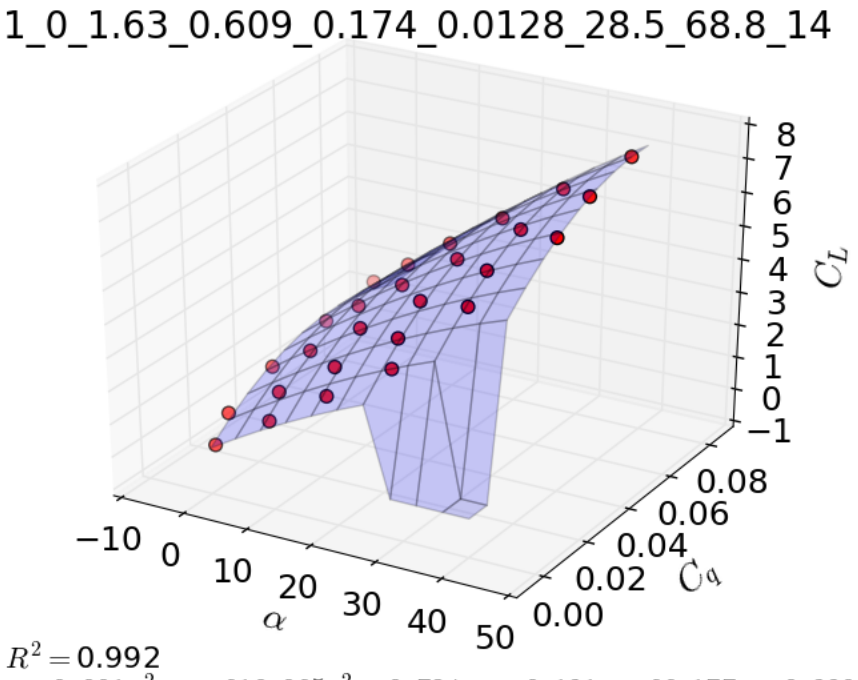

$R^2 = 0.992$

$C_L(x, y) = -0.001x^2 + -618.065y^2 + 0.734xy + 0.121x + 66.177y + 0.229$

Figure C.7: Surface fit C_L for β=28.5

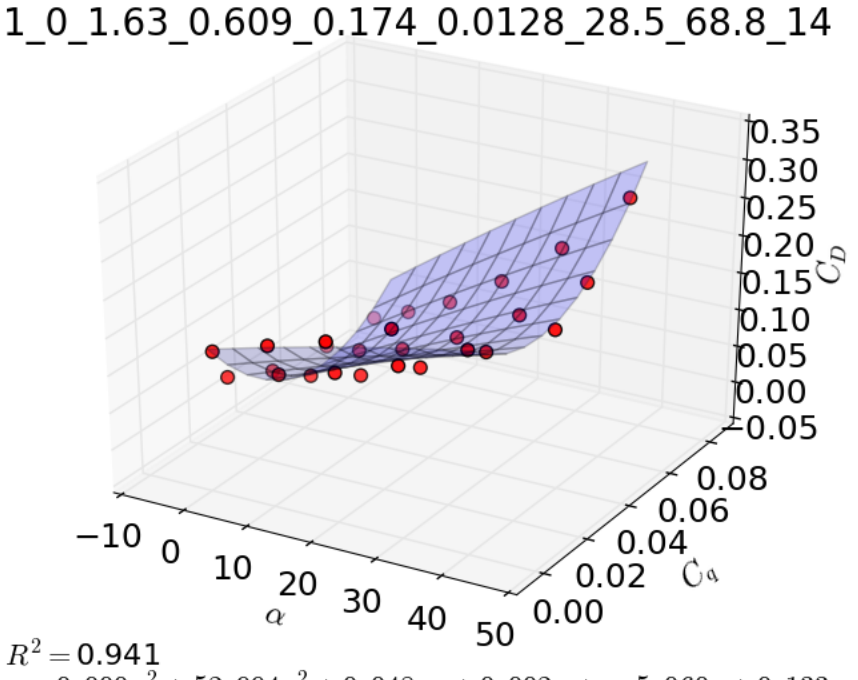

$R^2 = 0.941$

$C_D(x, y) = -0.000x^2 + 52.994y^2 + 0.048xy + 0.002x + -5.060y + 0.133$

Figure C.8: Surface fit C_D for β=28.5

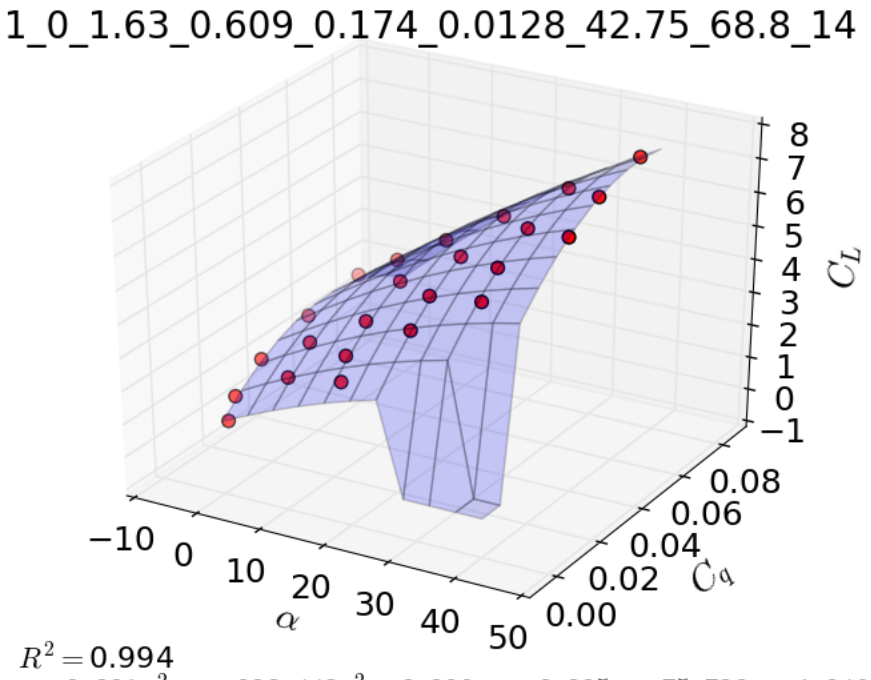

$R^2 = 0.994$

$C_L(x, y) = -0.001x^2 + -823.443y^2 + 0.986xy + 0.095x + 75.738y + 1.046$

Figure C.9: Surface fit C_L for β=42.75

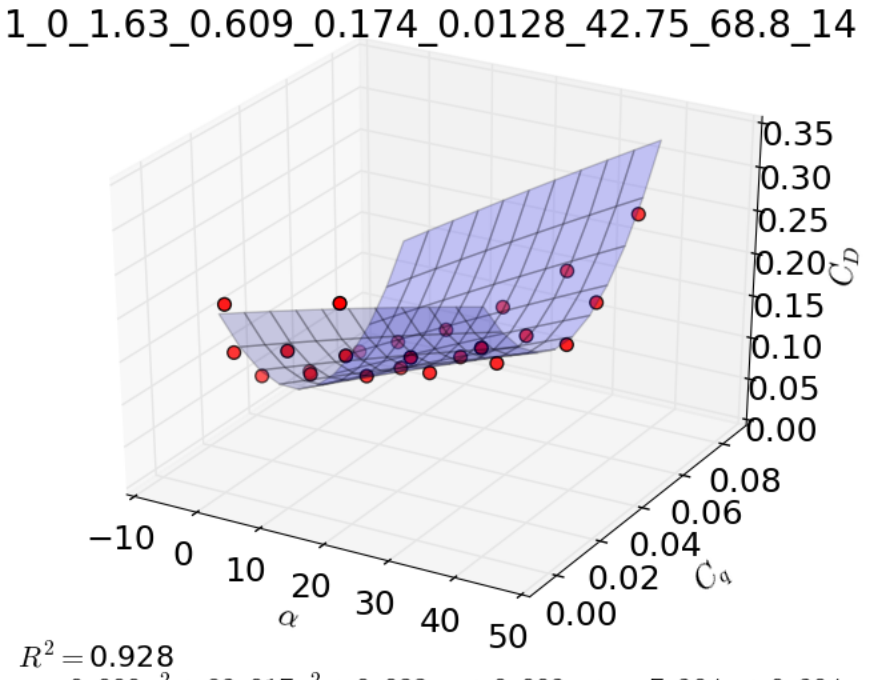

$R^2 = 0.928$

$C_D(x, y) = -0.000x^2 + 82.017y^2 + 0.033xy + 0.002x + -7.204y + 0.204$

Figure C.10: Surface fit C_D for β=42.75

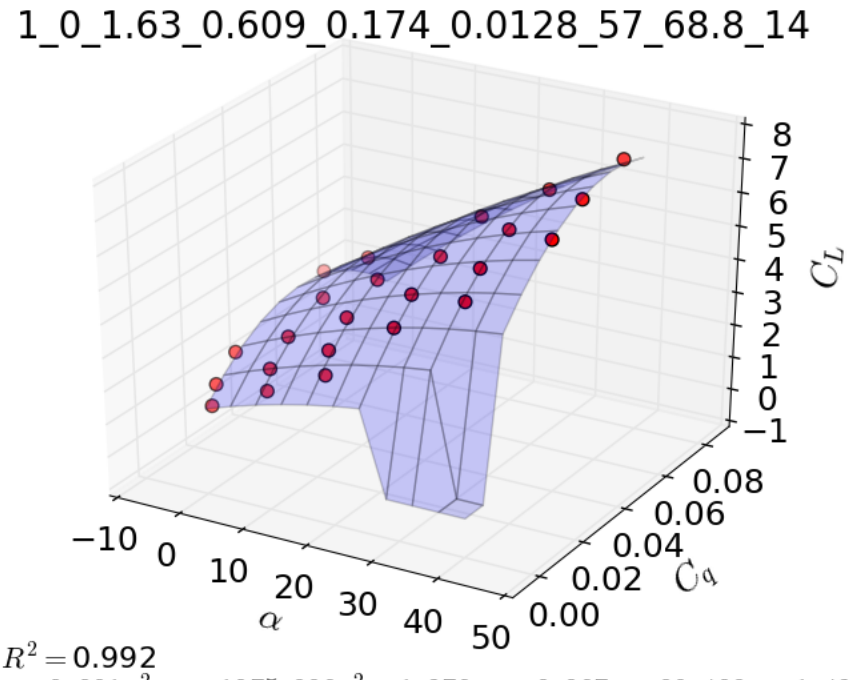

$R^2 = 0.992$

$C_L(x, y) = -0.001x^2 + -1075.896y^2 + 1.276xy + 0.067x + 89.408y + 1.425$

Figure C.11: Surface fit C_L for β=57

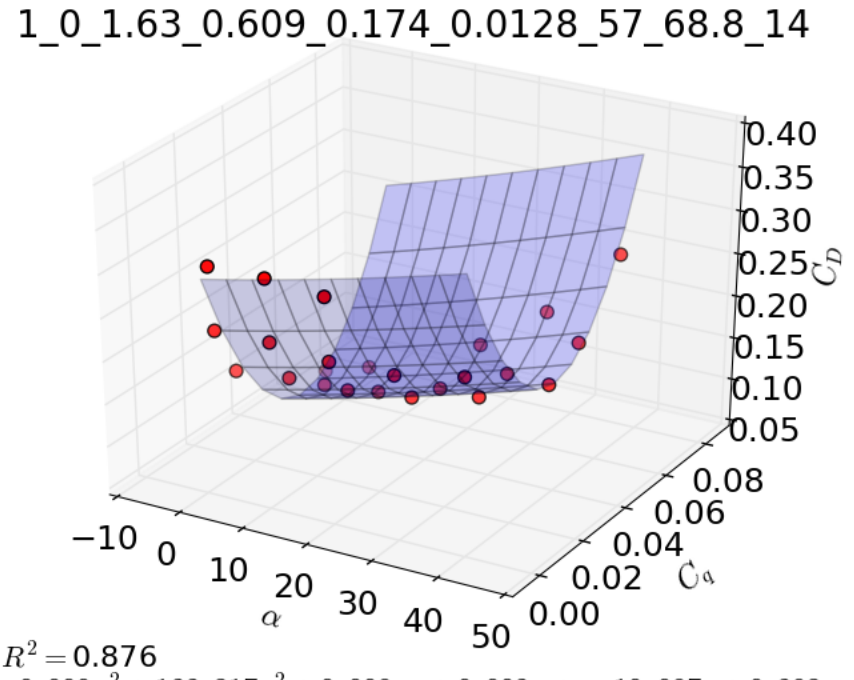

$R^2 = 0.876$

$C_D(x, y) = 0.000x^2 + 122.317y^2 + 0.008xy + 0.002x + -10.087y + 0.293$

Figure C.12: Surface fit C_D for β=57

C.2 Flap length variation

Variation in L_F/c.

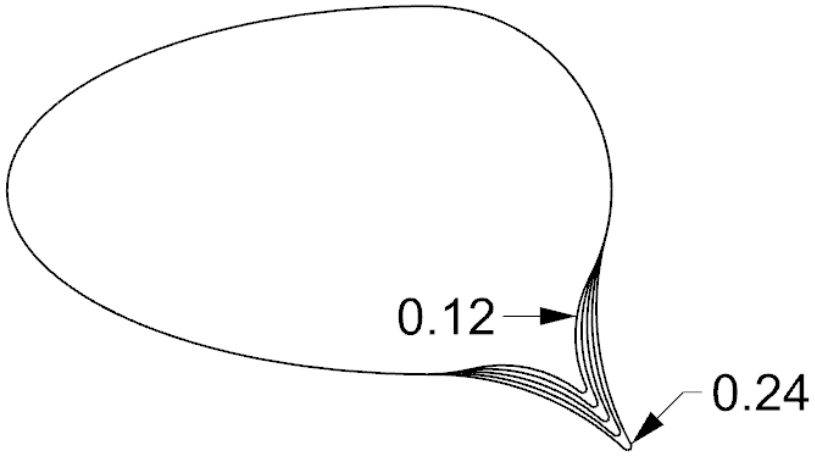

Figure C.13: Configurations L_F/c variation

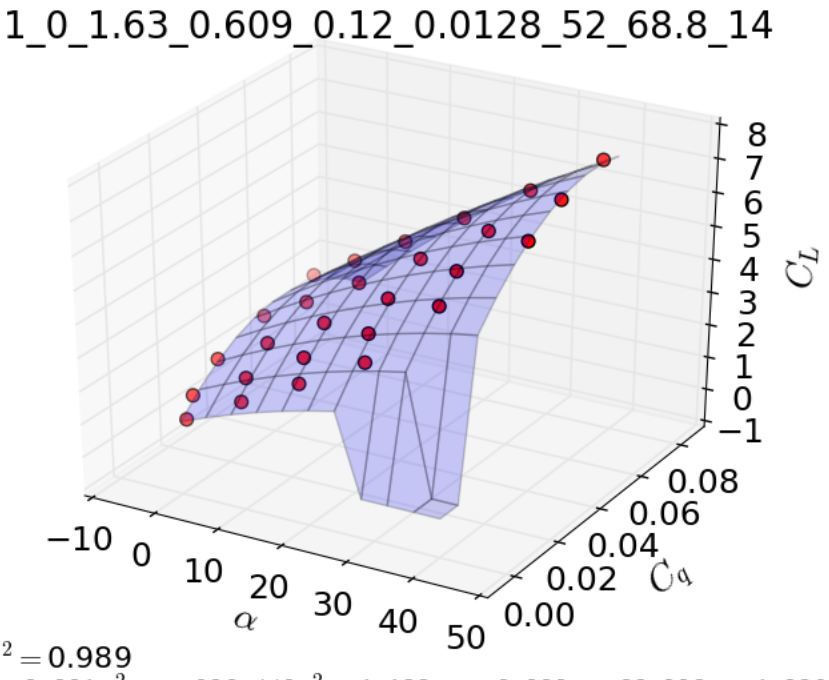

$R^2 = 0.989$

$C_L(x, y) = -0.001x^2 + -928.440y^2 + 1.133xy + 0.080x + 82.003y + 1.036$

Figure C.14: Surface fit C_L for L_F/c=0.12

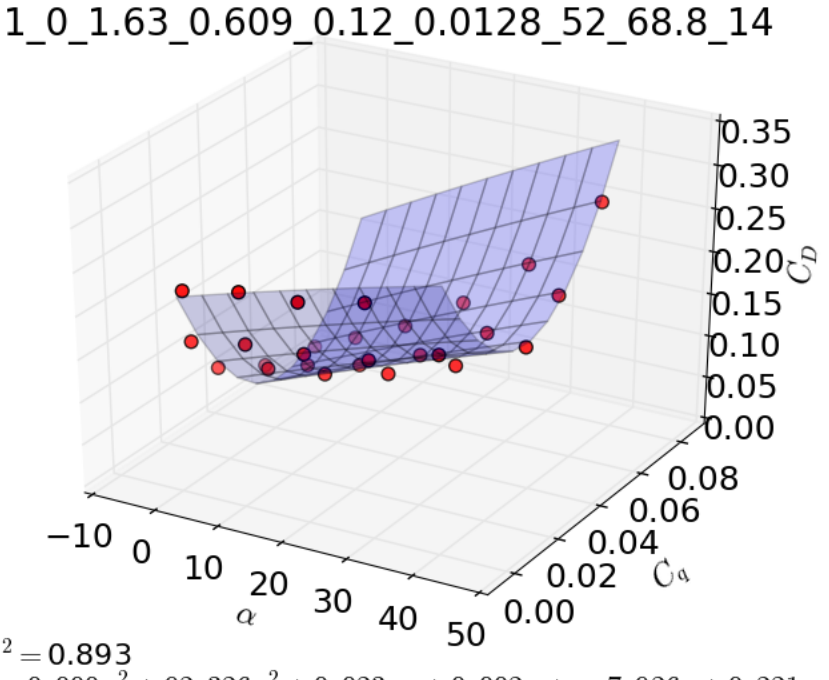

$R^2 = 0.893$

$C_D(x, y) = -0.000x^2 + 92.326y^2 + 0.023xy + 0.002x + -7.926y + 0.221$

Figure C.15: Surface fit C_D for L_F/c=0.12

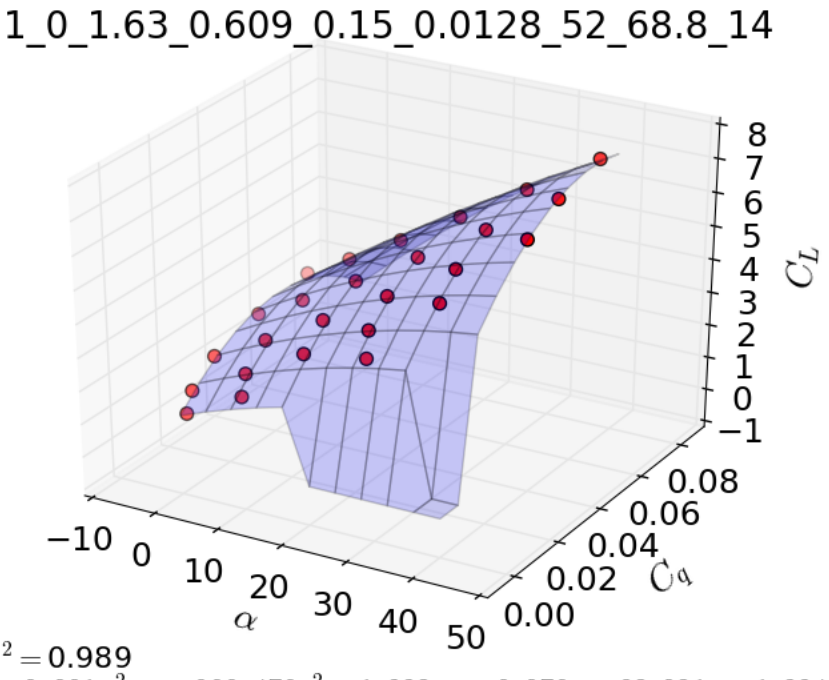

$R^2 = 0.989$

$C_L(x, y) = -0.001x^2 + -969.476y^2 + 1.223xy + 0.076x + 83.031y + 1.224$

Figure C.16: Surface fit C_L for L_F/c=0.15

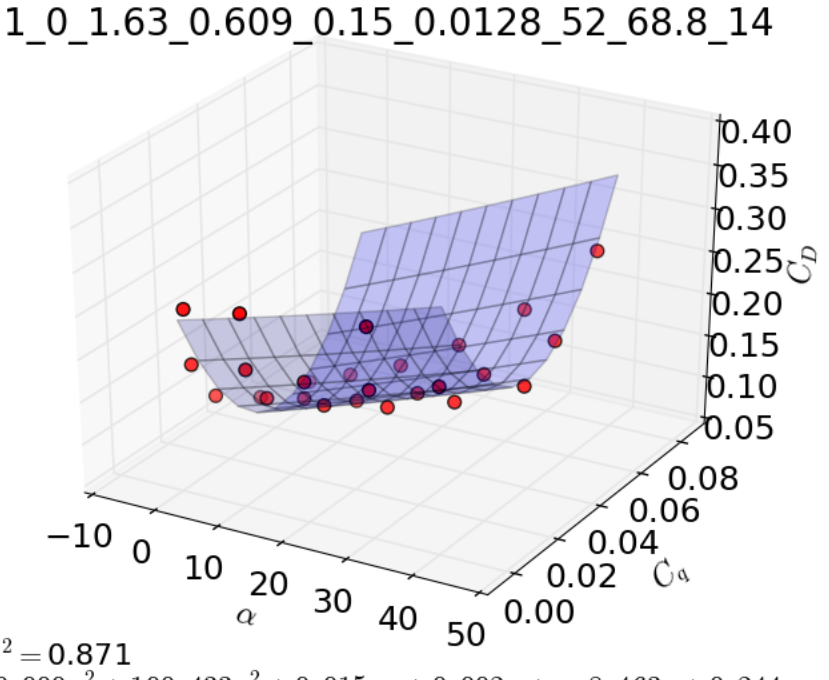

$R^2 = 0.871$

$C_D(x, y) = 0.000x^2 + 100.433y^2 + 0.015xy + 0.002x + -8.463y + 0.244$

Figure C.17: Surface fit C_D for L_F/c=0.15

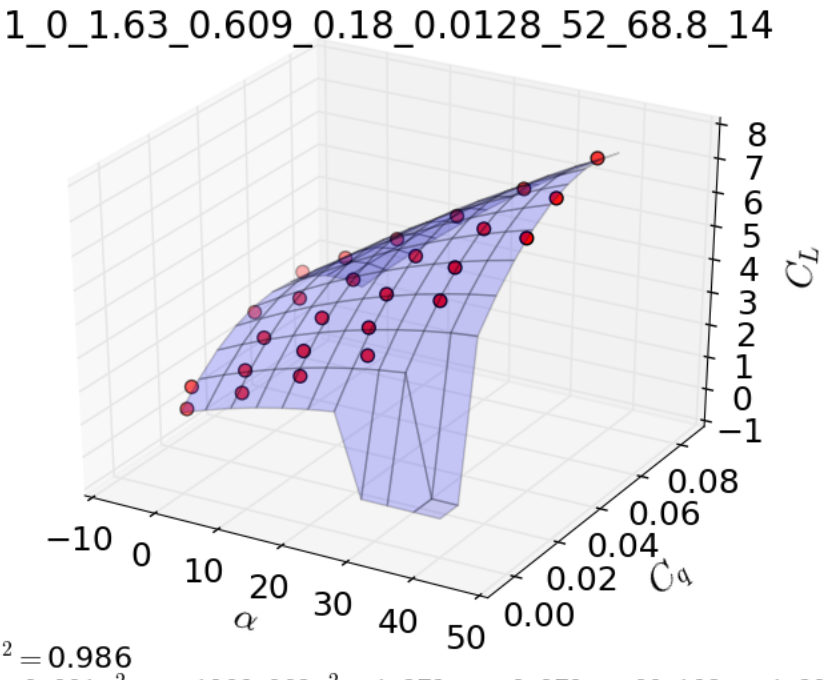

$R^2 = 0.986$

$C_L(x, y) = -0.001x^2 + -1082.963y^2 + 1.372xy + 0.070x + 89.123y + 1.307$

Figure C.18: Surface fit C_L for L_F/c=0.18

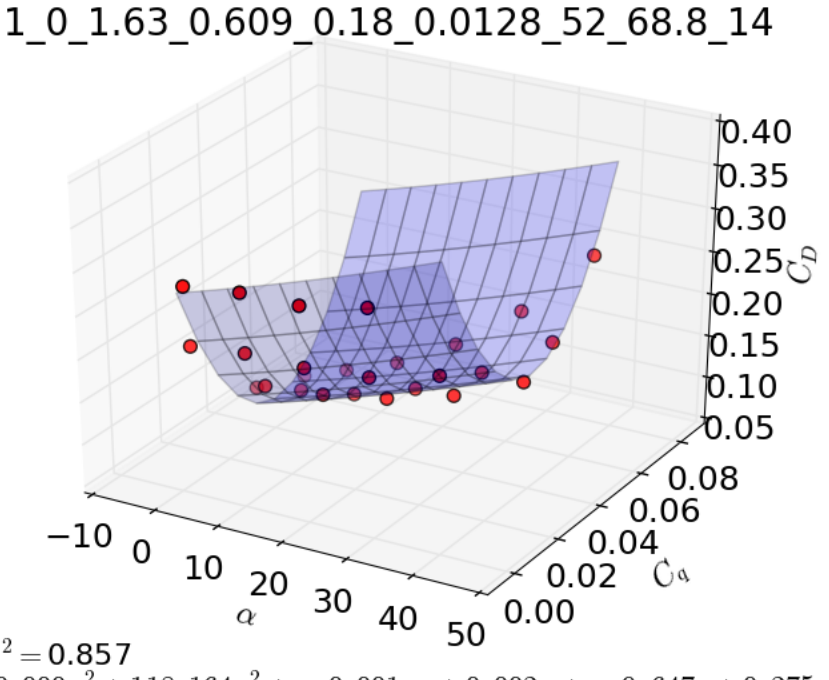

$R^2 = 0.857$

$C_D(x, y) = 0.000x^2 + 118.164y^2 + -0.001xy + 0.002x + -9.647y + 0.275$

Figure C.19: Surface fit C_D for L_F/c=0.18

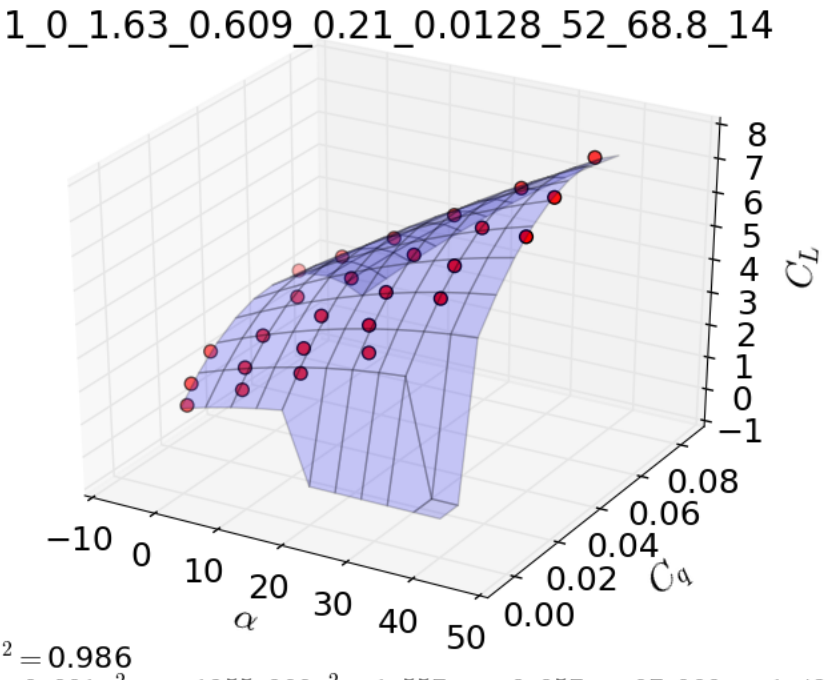

$R^2 = 0.986$

$$C_L(x, y) = -0.001x^2 + -1255.866y^2 + 1.557xy + 0.057x + 97.989y + 1.434$$

Figure C.20: Surface fit C_L for L_F/c=0.21

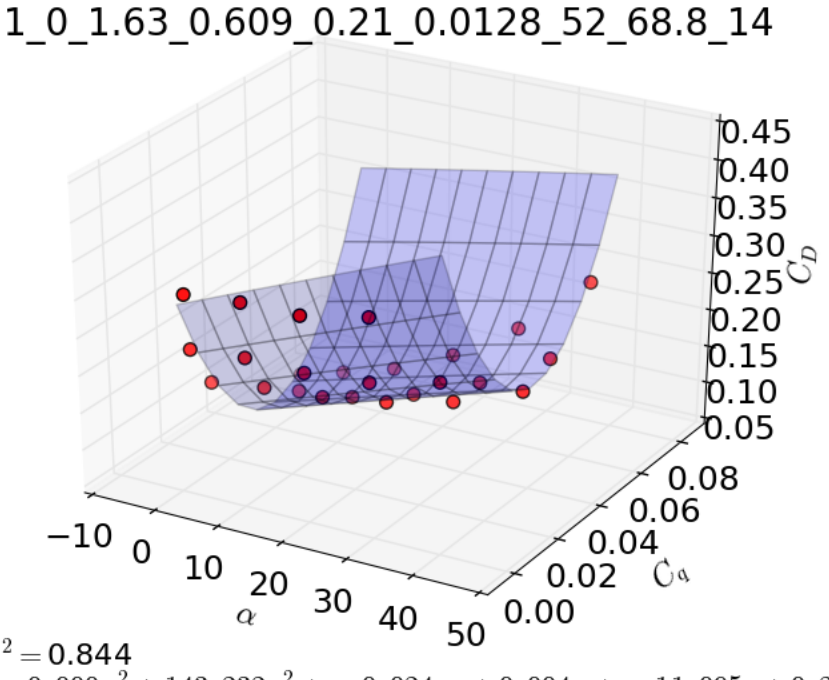

$R^2 = 0.844$

$$C_D(x, y) = -0.000x^2 + 143.232y^2 + -0.024xy + 0.004x + -11.095y + 0.292$$

Figure C.21: Surface fit C_D for L_F/c=0.21

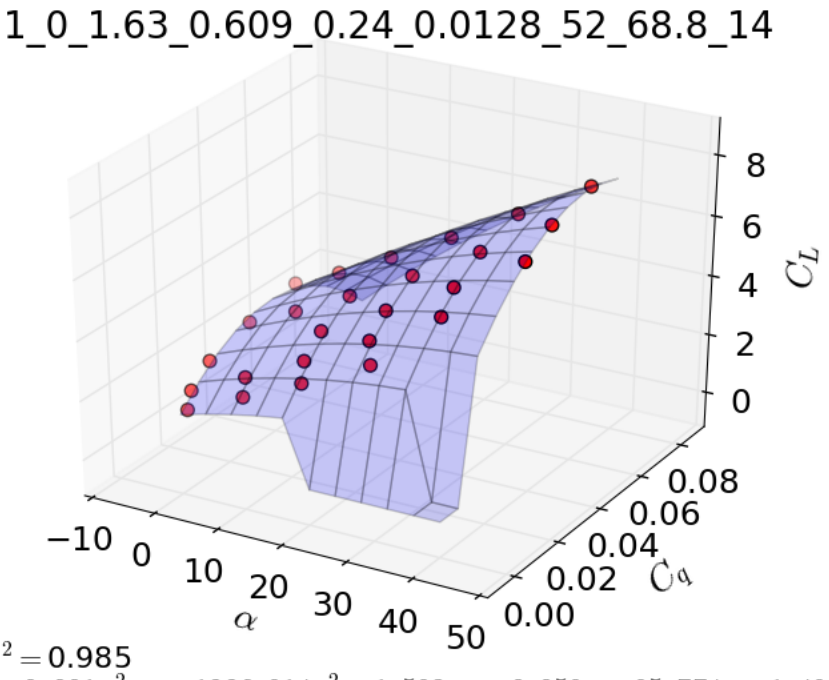

$R^2 = 0.985$

$C_L(x, y) = -0.001x^2 + -1226.914y^2 + 1.593xy + 0.059x + 95.774y + 1.498$

Figure C.22: Surface fit C_L for L_F/c=0.24

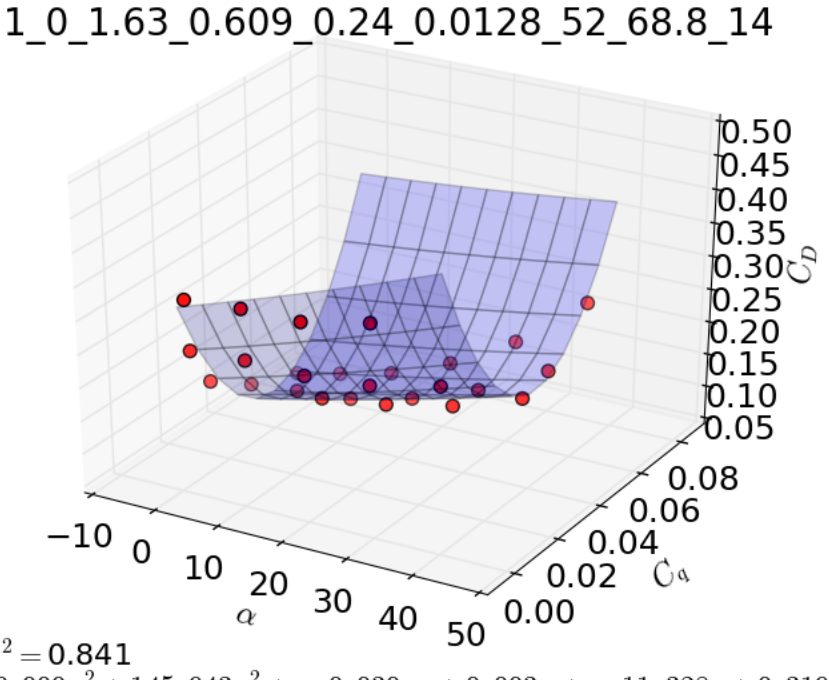

$R^2 = 0.841$

$C_D(x, y) = 0.000x^2 + 145.943y^2 + -0.030xy + 0.003x + -11.328y + 0.319$

Figure C.23: Surface fit C_D for L_F/c=0.24

C.3 Leading edge variation

Variation in h/t.

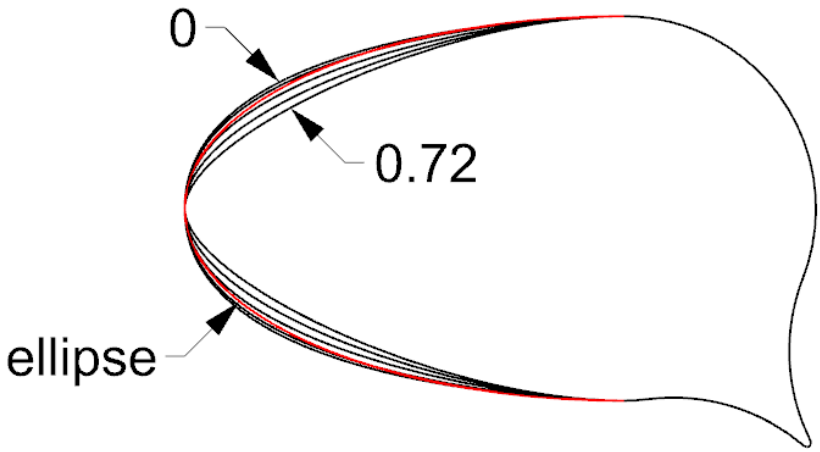

Figure C.24: Configurations h/t variation

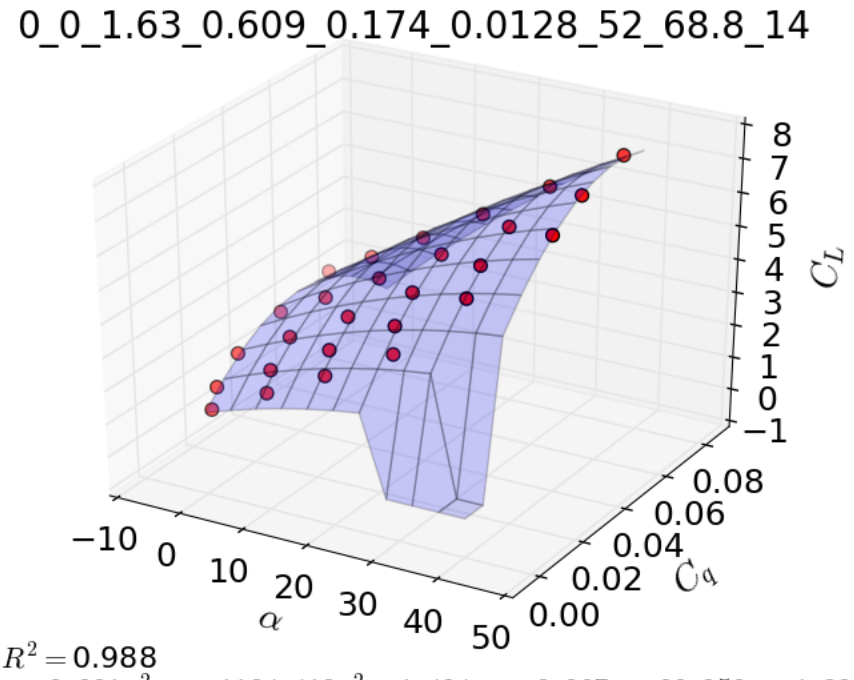

$R^2 = 0.988$

$C_L(x, y) = -0.001x^2 + -1104.410y^2 + 1.424xy + 0.067x + 90.250y + 1.307$

Figure C.25: Surface fit C_L for h/t=0

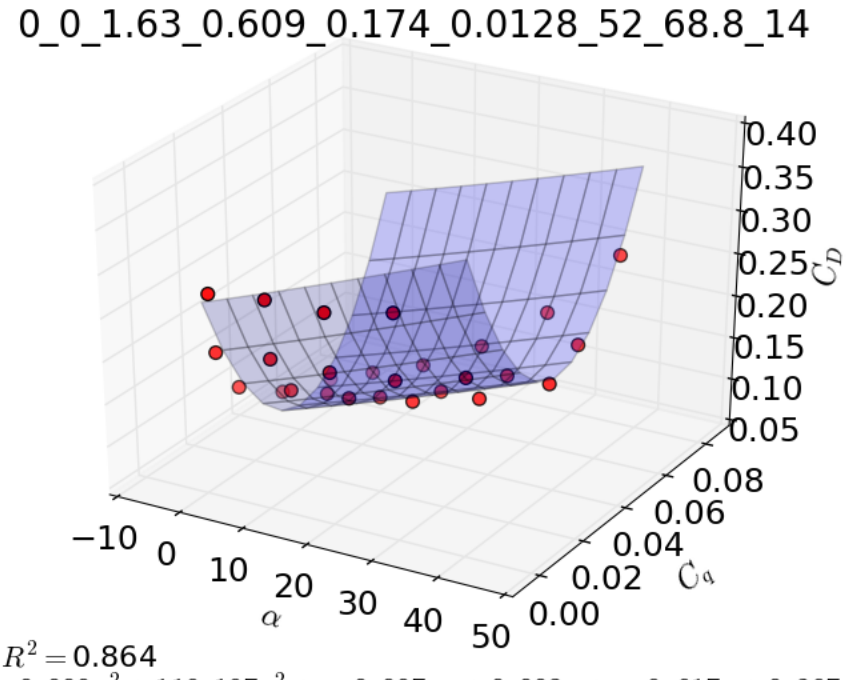

$R^2 = 0.864$

$C_D(x, y) = 0.000x^2 + 119.197y^2 + -0.007xy + 0.003x + -9.617y + 0.267$

Figure C.26: Surface fit C_D for h/t=0

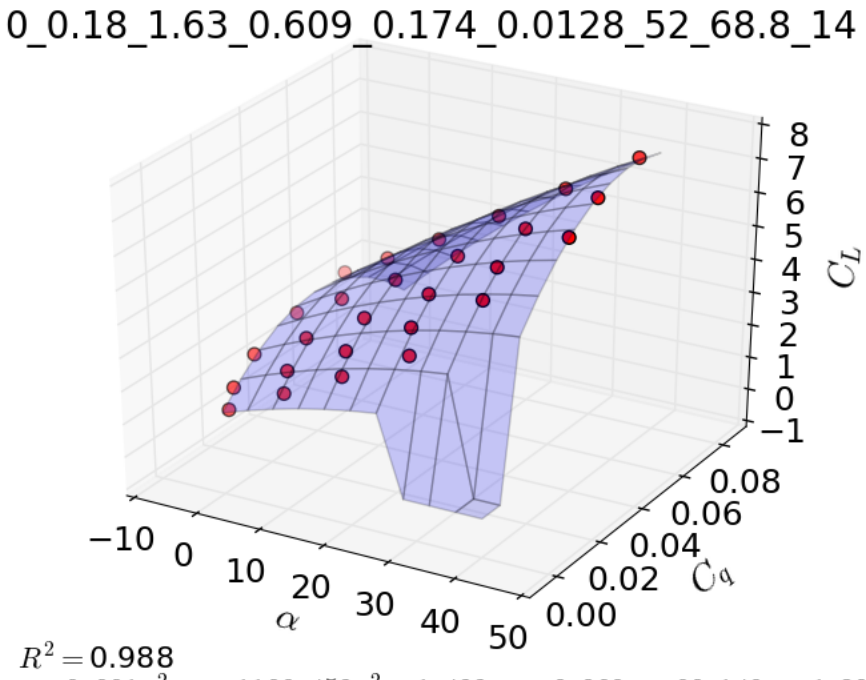

$R^2 = 0.988$

$C_L(x, y) = -0.001x^2 + -1109.452y^2 + 1.422xy + 0.068x + 90.149y + 1.302$

Figure C.27: Surface fit C_L for h/t=0.18

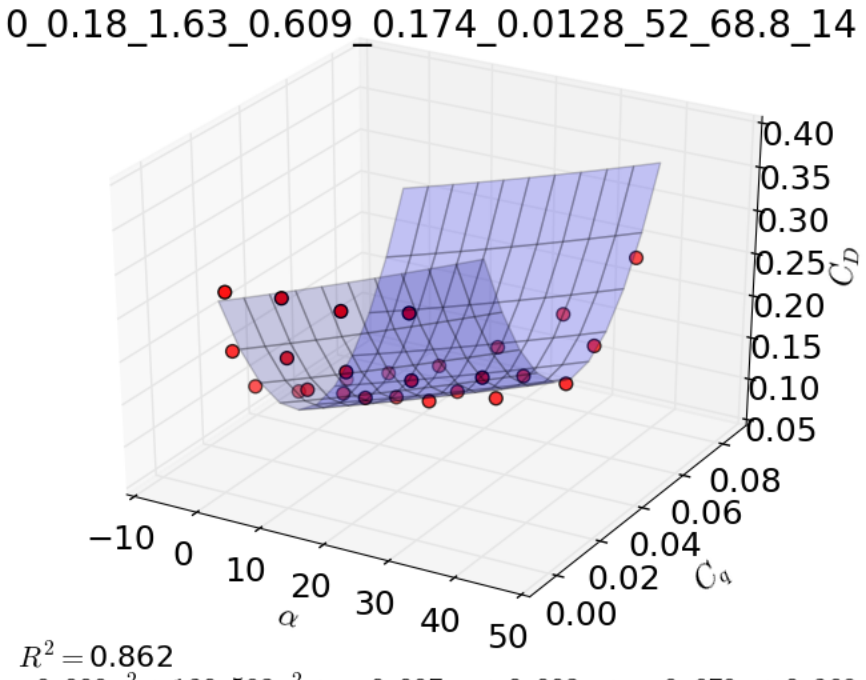

$R^2 = 0.862$

$C_D(x, y) = 0.000x^2 + 120.593y^2 + -0.007xy + 0.003x + -9.679y + 0.268$

Figure C.28: Surface fit C_D for h/t=0.18

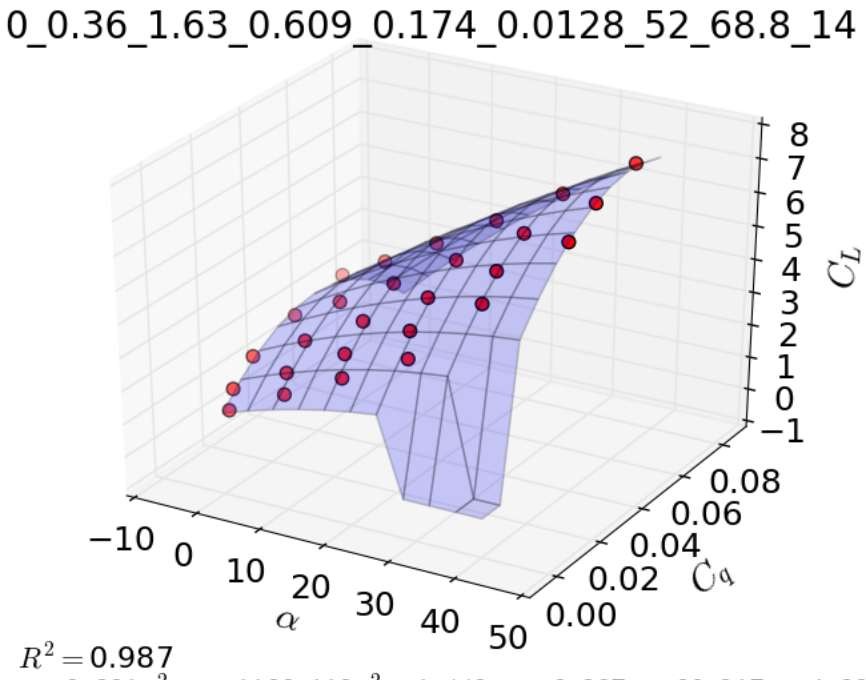

$R^2 = 0.987$

$C_L(x, y) = -0.001x^2 + -1120.119y^2 + 1.440xy + 0.067x + 89.817y + 1.291$

Figure C.29: Surface fit C_L for h/t=0.36

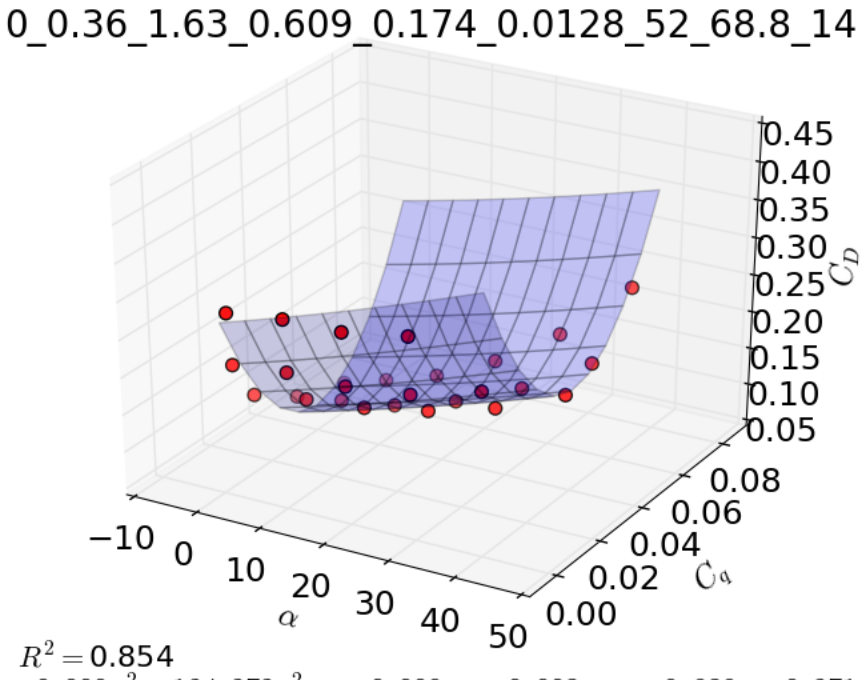

$R^2 = 0.854$

$C_D(x, y) = 0.000x^2 + 124.272y^2 + -0.009xy + 0.003x + -9.839y + 0.271$

Figure C.30: Surface fit C_D for h/t=0.36

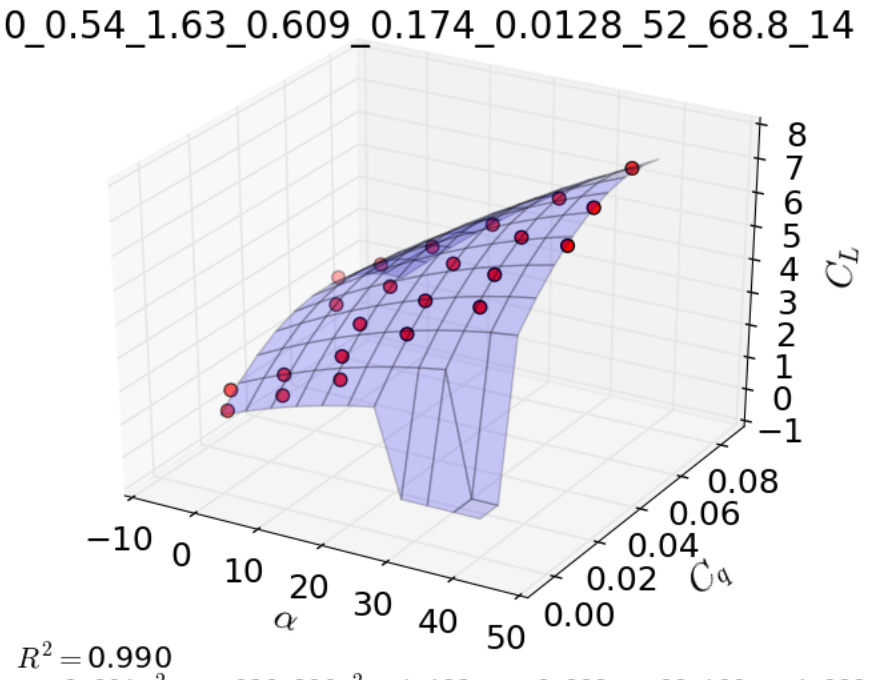

$R^2 = 0.990$

$C_L(x, y) = -0.001x^2 + -939.396y^2 + 1.122xy + 0.080x + 82.162y + 1.233$

Figure C.31: Surface fit C_L for h/t=0.54

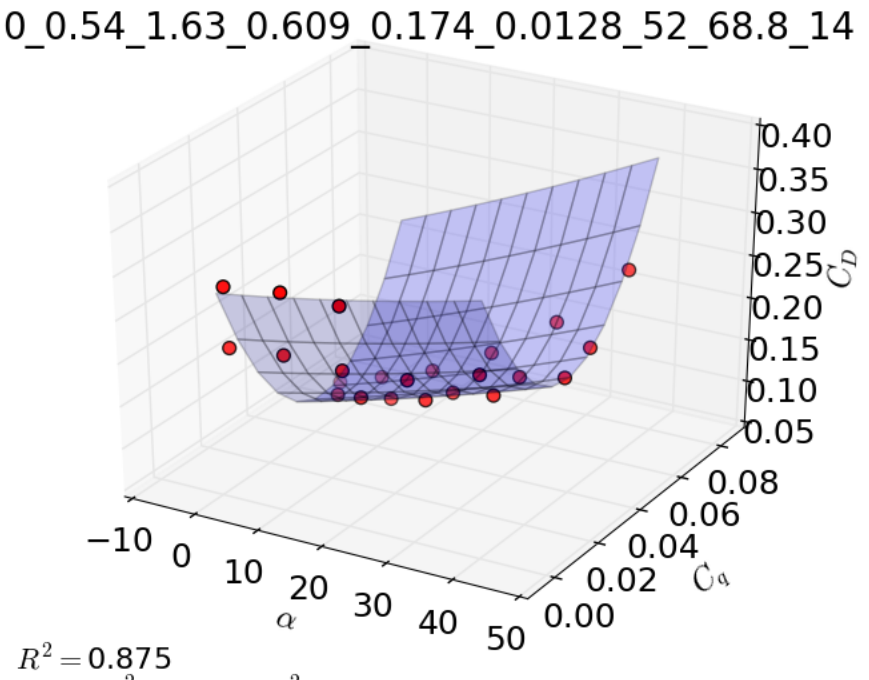

$R^2 = 0.875$

$C_D(x, y) = 0.000x^2 + 107.496y^2 + 0.024xy + 0.001x + -9.222y + 0.280$

Figure C.32: Surface fit C_D for h/t=0.54

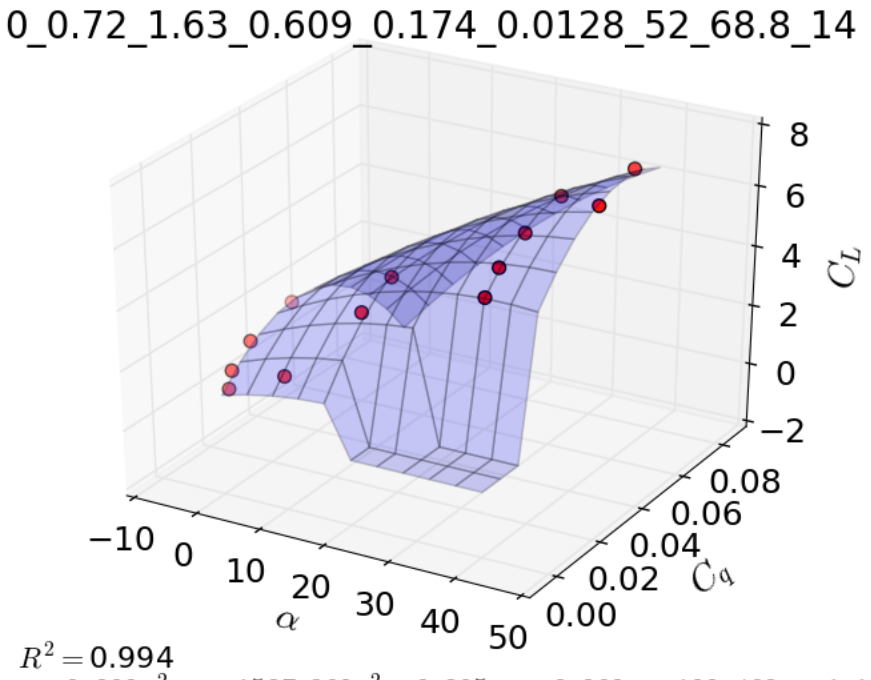

$R^2 = 0.994$

$C_L(x, y) = -0.002x^2 + -1537.360y^2 + 2.385xy + 0.062x + 100.463y + 1.153$

Figure C.33: Surface fit C_L for h/t=0.72

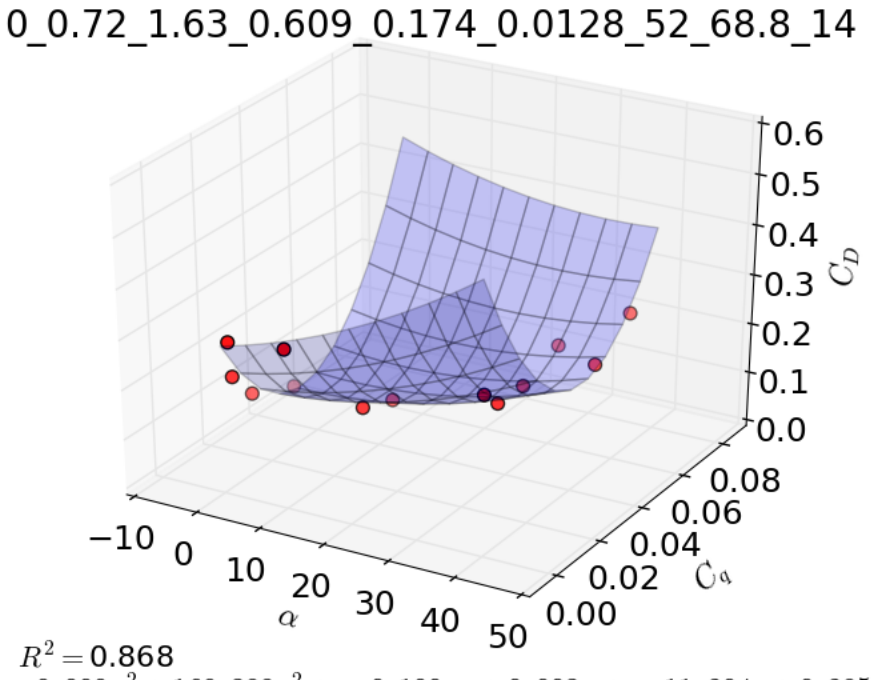

$R^2 = 0.868$

$C_D(x, y) = 0.000x^2 + 169.388y^2 + -0.100xy + 0.003x + -11.204y + 0.285$

Figure C.34: Surface fit C_D for h/t=0.72

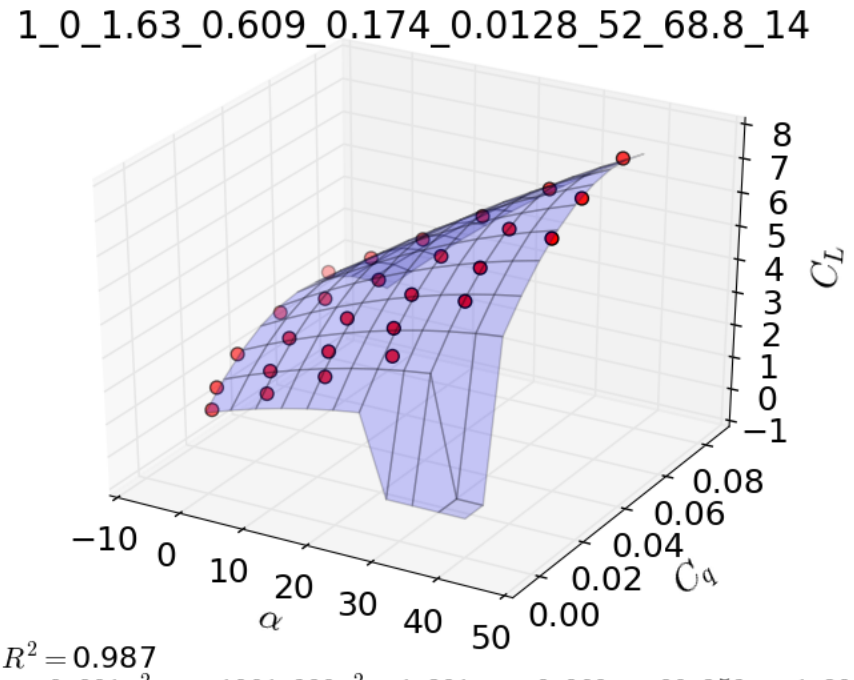

$R^2 = 0.987$

$C_L(x, y) = -0.001x^2 + -1091.289y^2 + 1.381xy + 0.068x + 89.352y + 1.304$

Figure C.35: Surface fit C_L for an ellipse

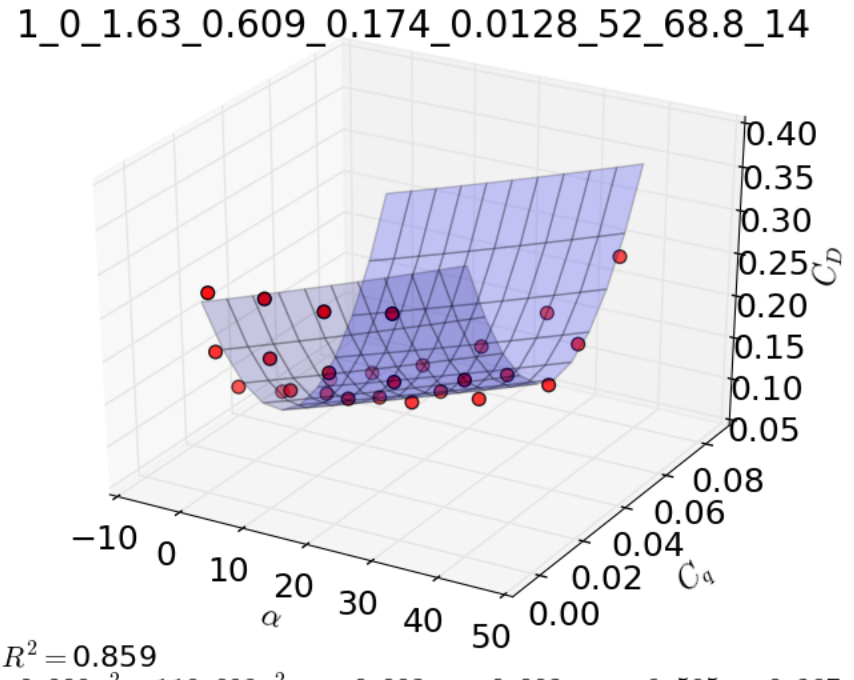

$R^2 = 0.859$

$C_D(x, y) = 0.000x^2 + 118.698y^2 + -0.003xy + 0.003x + -9.595y + 0.267$

Figure C.36: Surface fit C_D an ellipse

C.4 Thickness variation

Variation in t/c.

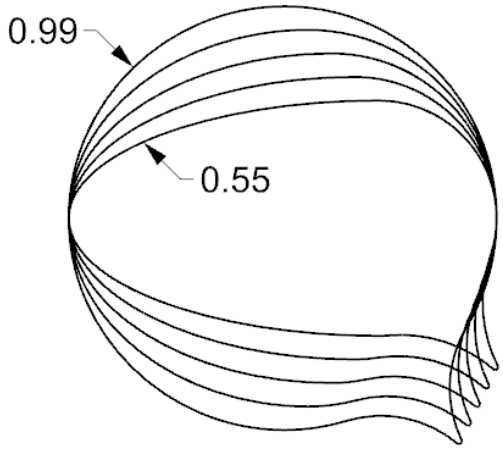

Figure C.37: Configurations t/c variation

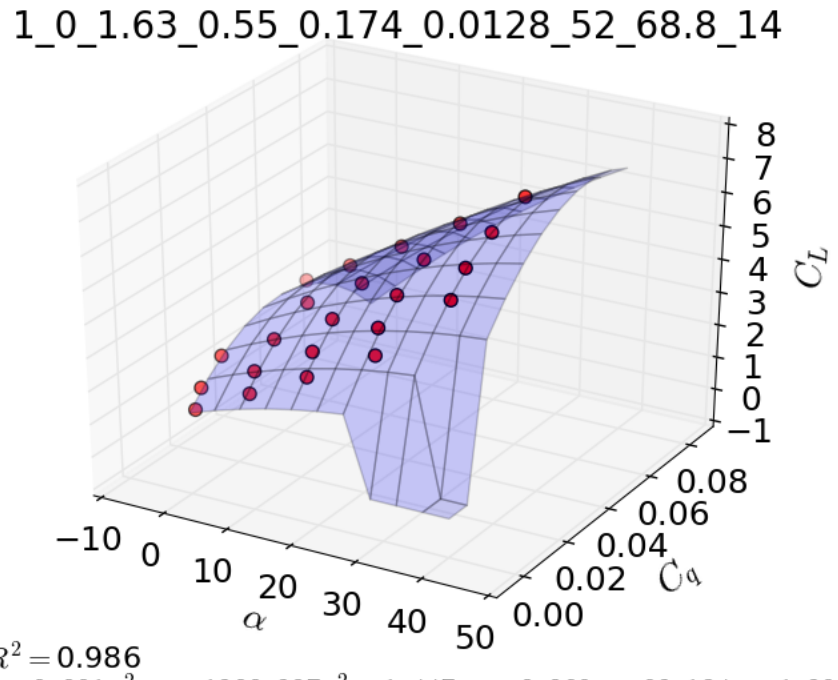

$R^2 = 0.986$

$C_L(x, y) = -0.001x^2 + -1200.287y^2 + 1.447xy + 0.069x + 92.134y + 1.298$

Figure C.38: Surface fit C_L for t/c=0.55

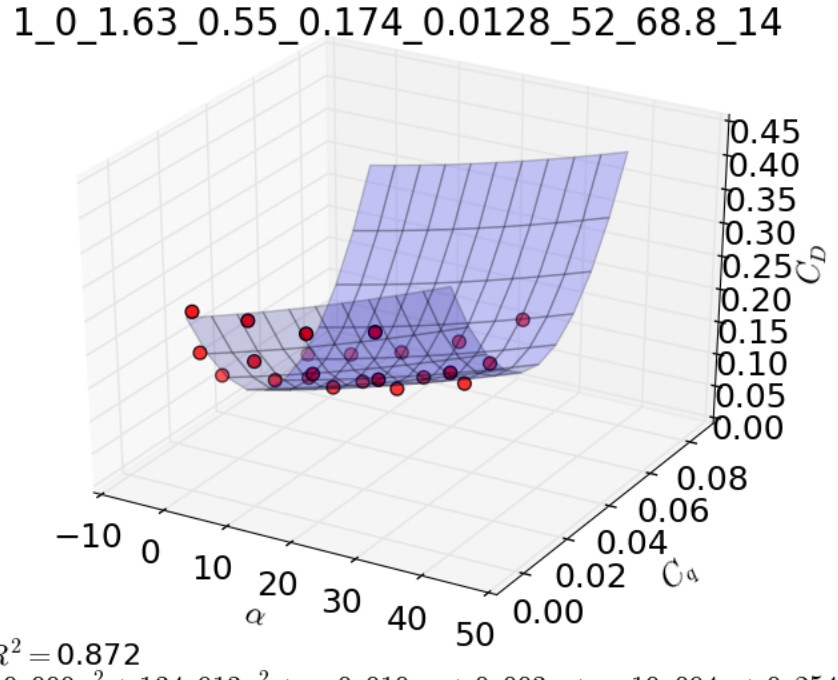

$R^2 = 0.872$

$C_D(x, y) = 0.000x^2 + 134.913y^2 + -0.010xy + 0.003x + -10.094y + 0.254$

Figure C.39: Surface fit C_D for t/c=0.55

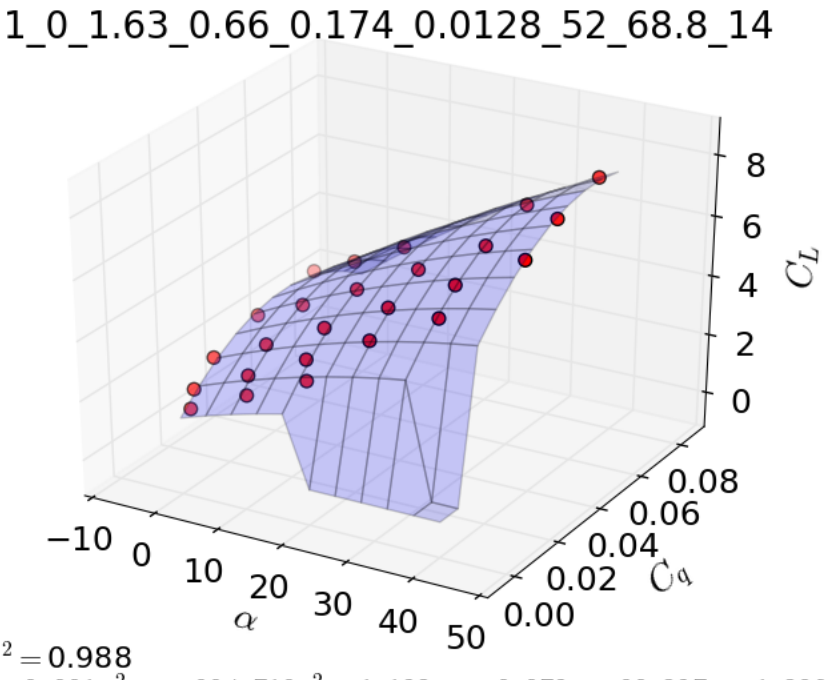

$R^2 = 0.988$

$$C_L(x, y) = -0.001x^2 + -994.719y^2 + 1.123xy + 0.072x + 90.327y + 1.386$$

Figure C.40: Surface fit C_L for t/c=0.66

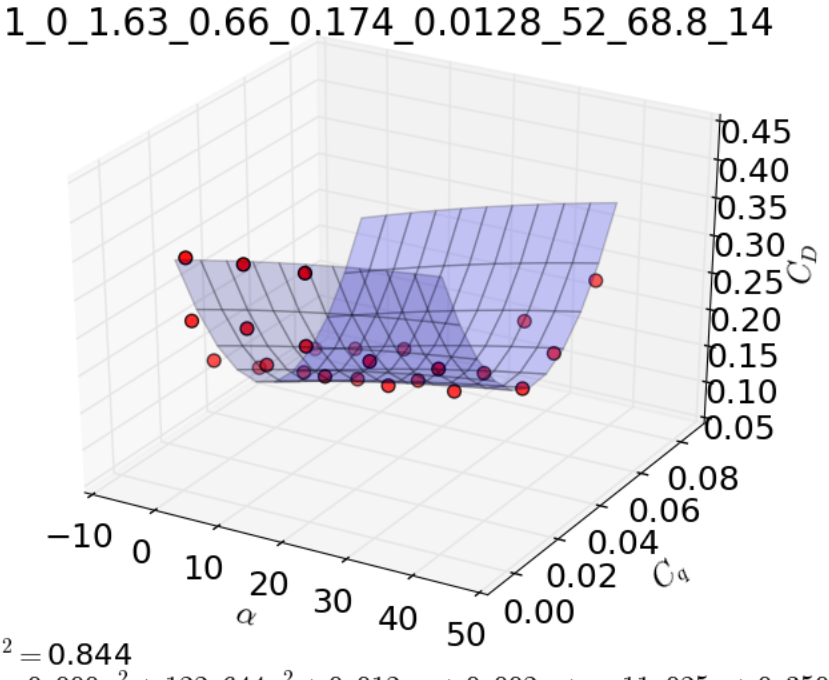

$R^2 = 0.844$

$$C_D(x, y) = -0.000x^2 + 122.644y^2 + 0.012xy + 0.002x + -11.025y + 0.350$$

Figure C.41: Surface fit C_D for t/c=0.66

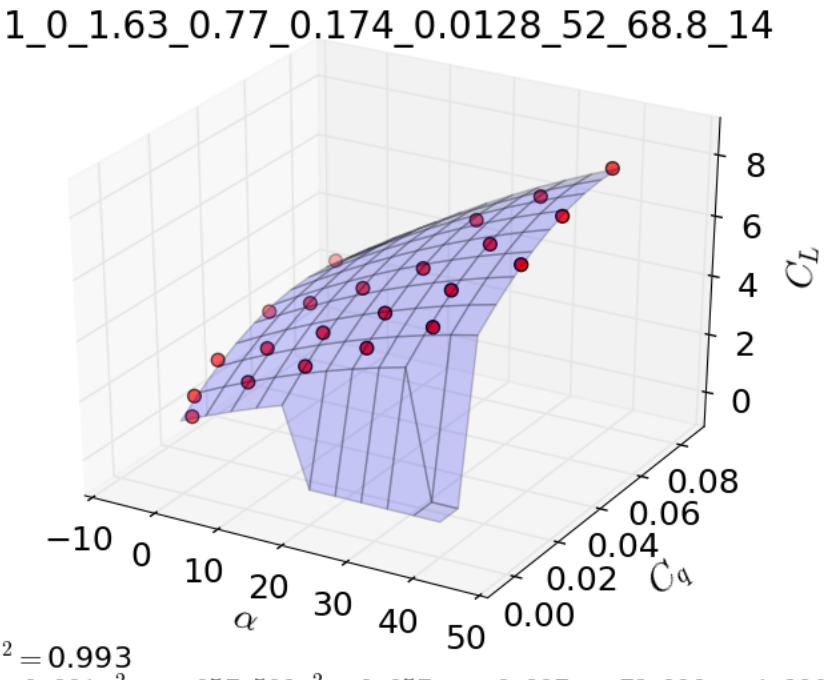

$R^2 = 0.993$

$C_L(x, y) = -0.001x^2 + -657.502y^2 + 0.657xy + 0.097x + 73.022y + 1.286$

Figure C.42: Surface fit C_L for t/c=0.77

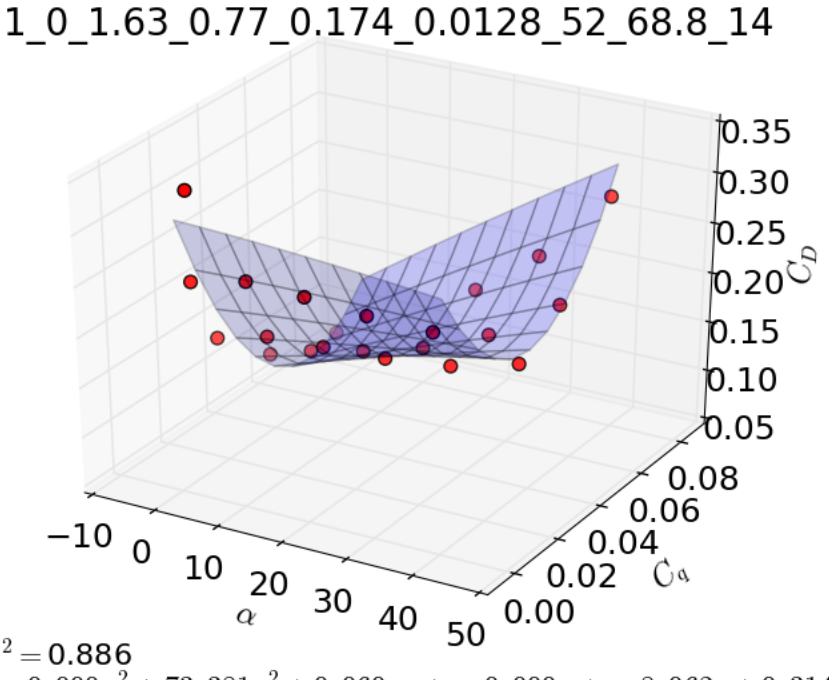

$R^2 = 0.886$

$C_D(x, y) = -0.000x^2 + 73.381y^2 + 0.060xy + -0.000x + -8.062y + 0.314$

Figure C.43: Surface fit C_D for t/c=0.77

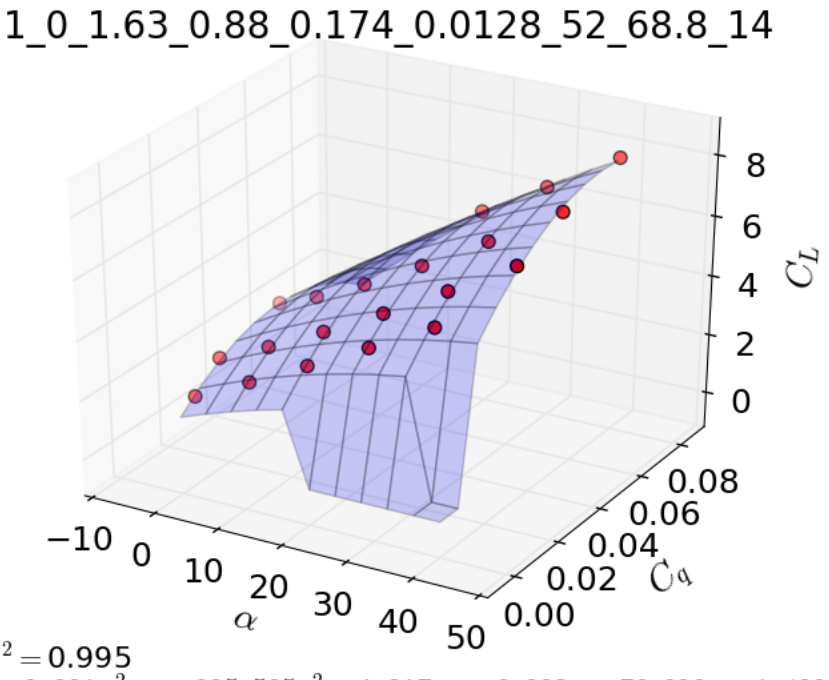

$R^2 = 0.995$

$C_L(x, y) = -0.001x^2 + -885.505y^2 + 1.317xy + 0.083x + 76.633y + 1.409$

Figure C.44: Surface fit C_L for t/c=0.88

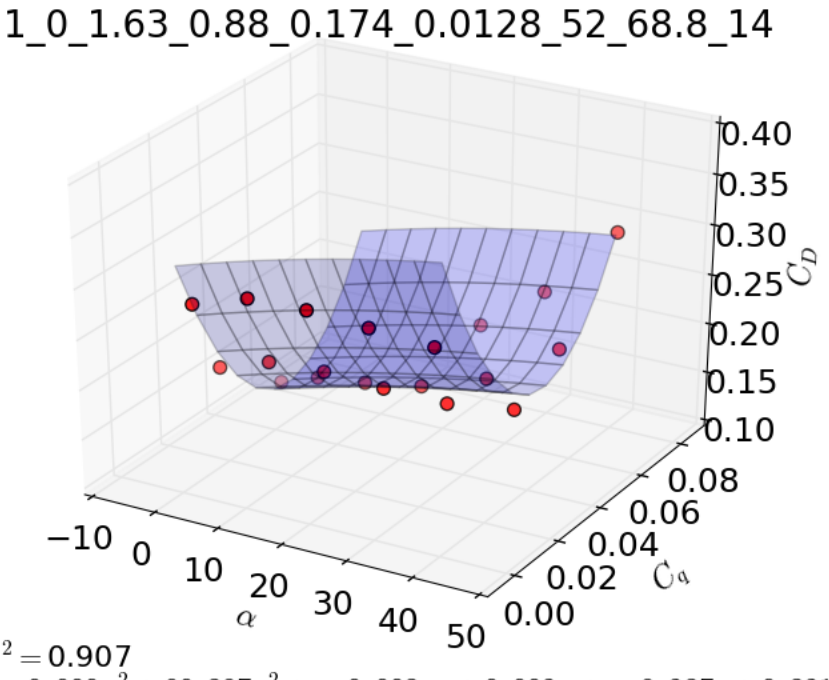

$R^2 = 0.907$

$C_D(x, y) = -0.000x^2 + 90.387y^2 + -0.003xy + 0.002x + -8.237y + 0.321$

Figure C.45: Surface fit C_D for t/c=0.88

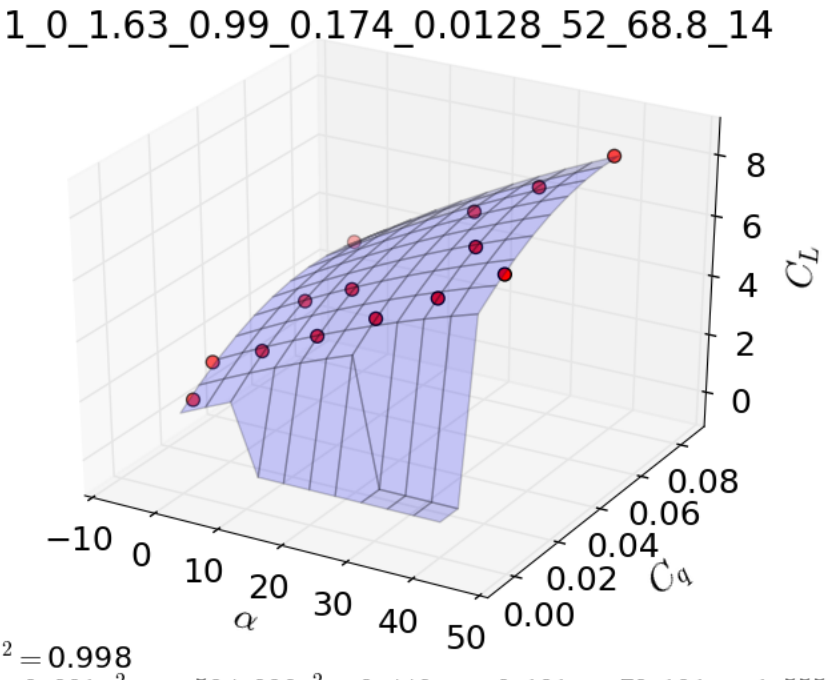

$R^2 = 0.998$

$C_L(x, y) = -0.001x^2 + -584.086y^2 + 0.446xy + 0.101x + 70.181y + 1.555$

Figure C.46: Surface fit C_L for t/c=0.99

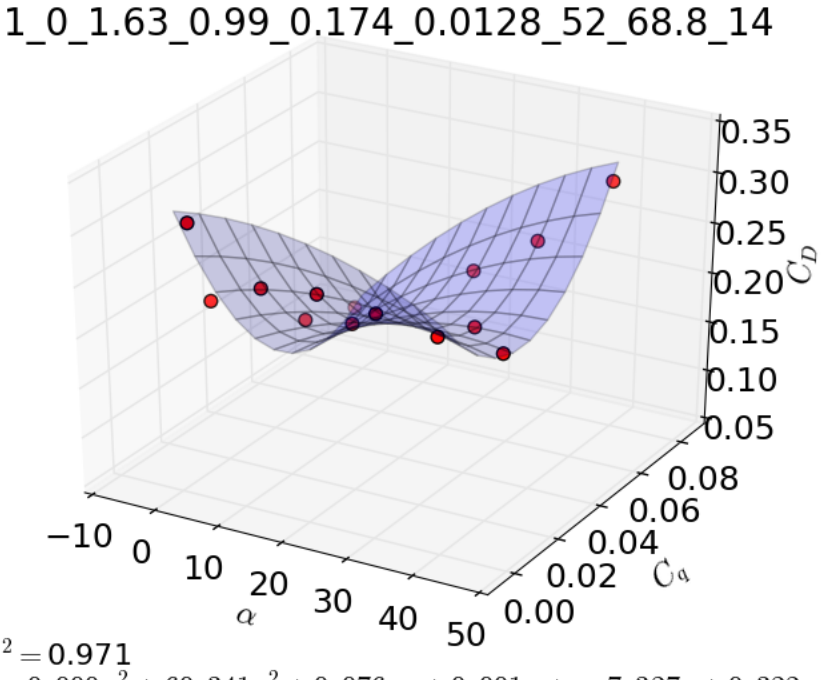

$R^2 = 0.971$

$C_D(x, y) = -0.000x^2 + 60.341y^2 + 0.076xy + 0.001x + -7.327y + 0.322$

Figure C.47: Surface fit C_D for t/c=0.99

C.5 Variation in suction width

Variation in θ.

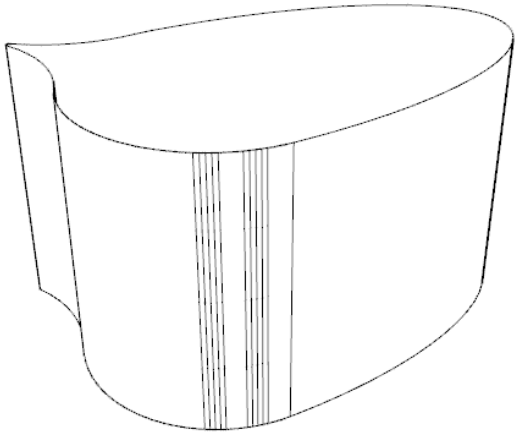

Figure C.48: Configurations θ variation

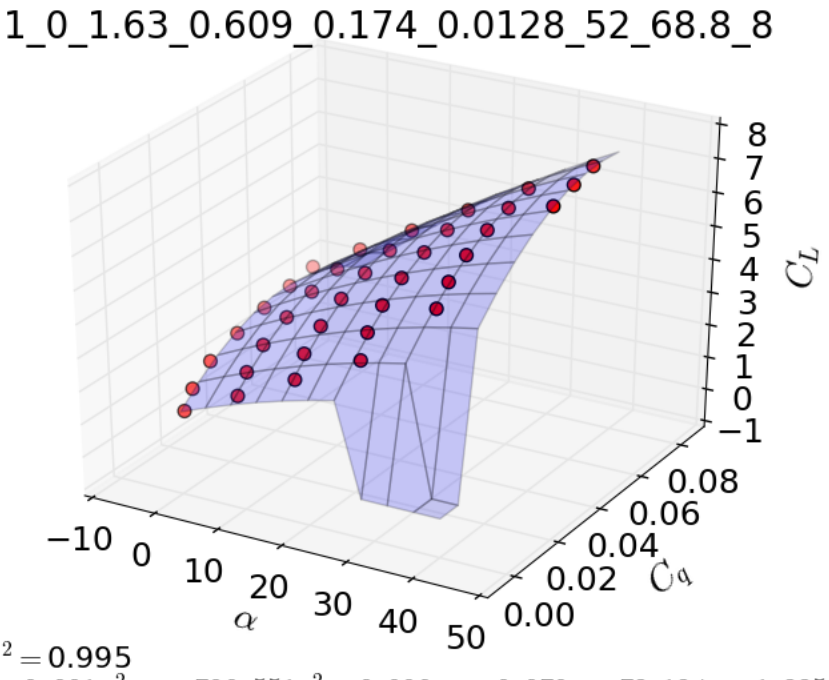

$R^2 = 0.995$

$C_L(x, y) = -0.001x^2 + -789.551y^2 + 0.996xy + 0.079x + 73.134y + 1.335$

Figure C.49: Surface fit C_L for θ=8[°]

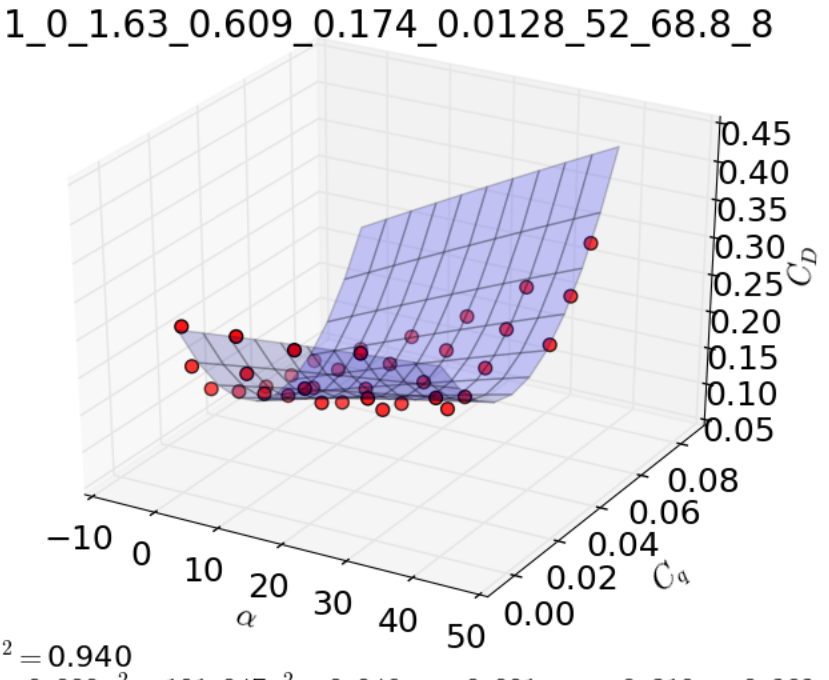

$R^2 = 0.940$

$C_D(x, y) = -0.000x^2 + 101.047y^2 + 0.046xy + 0.001x + -8.319y + 0.262$

Figure C.50: Surface fit C_D for θ=8[°]

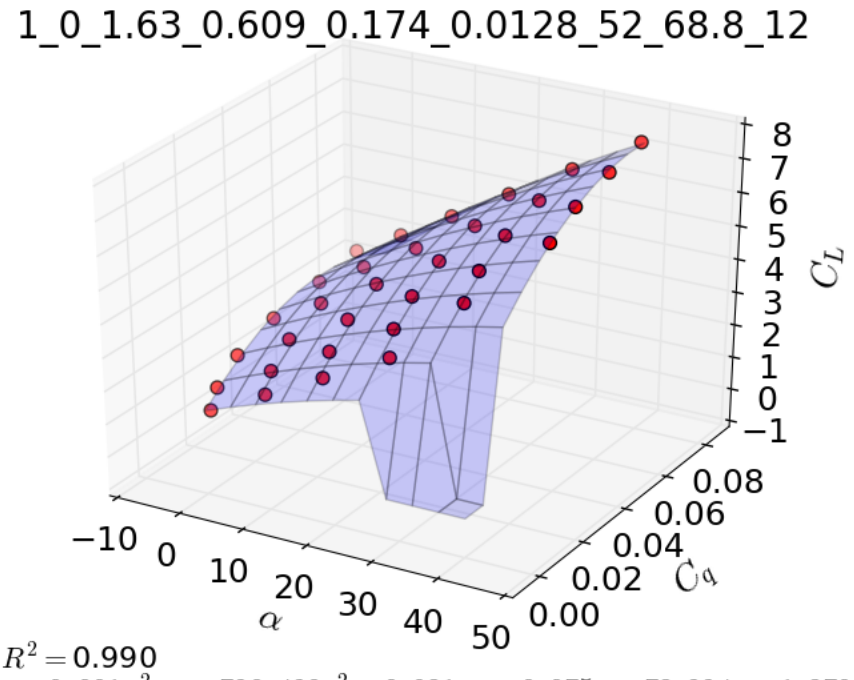

$R^2 = 0.990$

$C_L(x, y) = -0.001x^2 + -728.428y^2 + 0.931xy + 0.075x + 73.224y + 1.370$

Figure C.51: Surface fit C_L for θ=12[°]

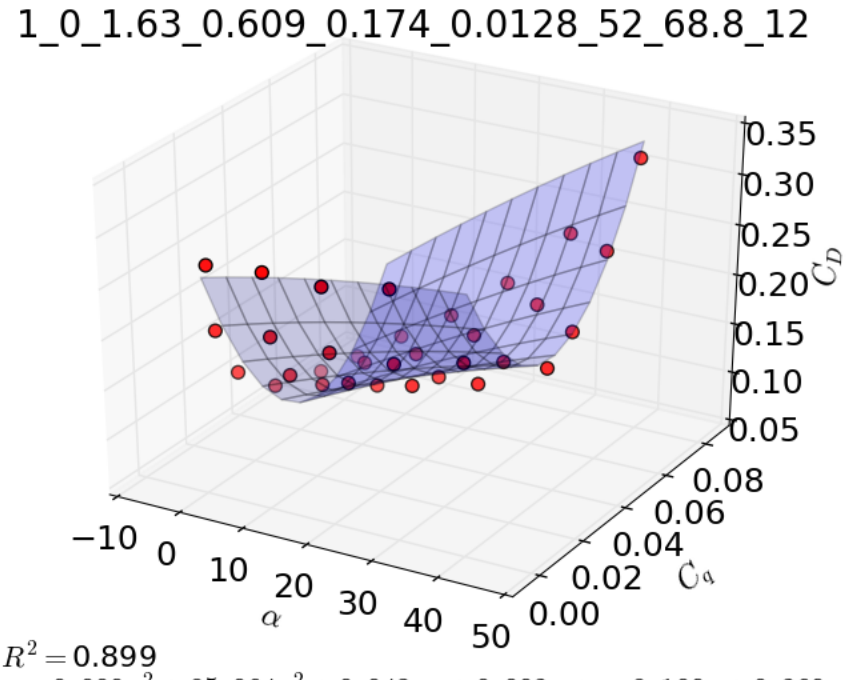

$R^2 = 0.899$

$C_D(x, y) = -0.000x^2 + 85.064y^2 + 0.043xy + 0.002x + -8.100y + 0.260$

Figure C.52: Surface fit C_D for θ=12[°]

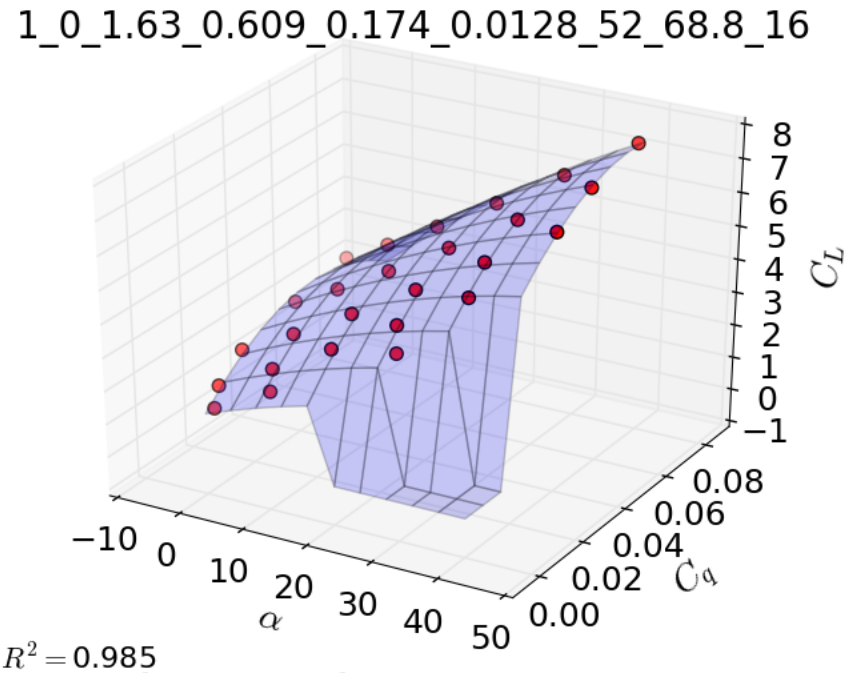

$R^2 = 0.985$

$C_L(x, y) = -0.001x^2 + -833.051y^2 + 1.110xy + 0.074x + 79.707y + 1.276$

Figure C.53: Surface fit C_L for θ=16[°]

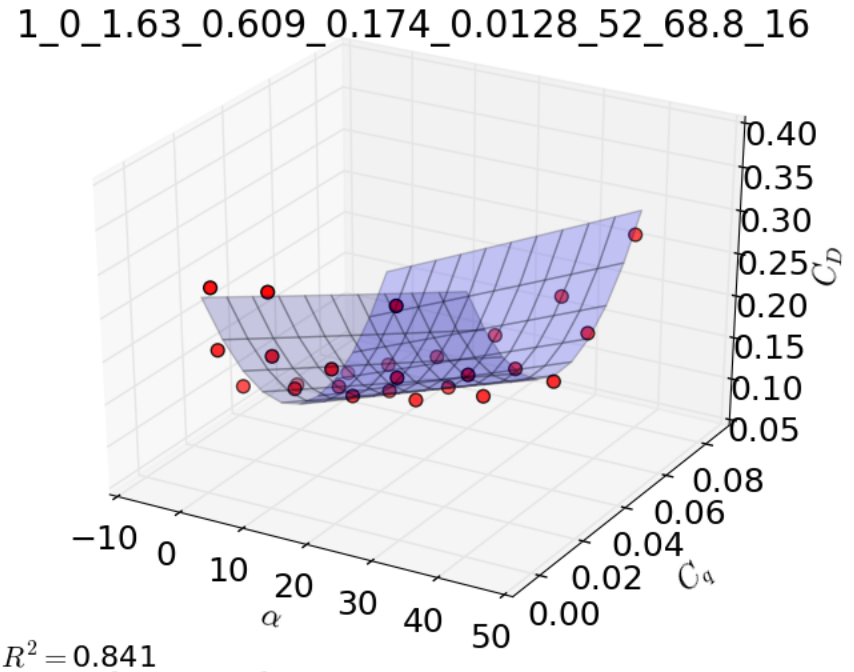

$R^2 = 0.841$

$C_D(x, y) = 0.000x^2 + 90.423y^2 + 0.020xy + 0.002x + -8.579y + 0.273$

Figure C.54: Surface fit C_D for θ=16[°]

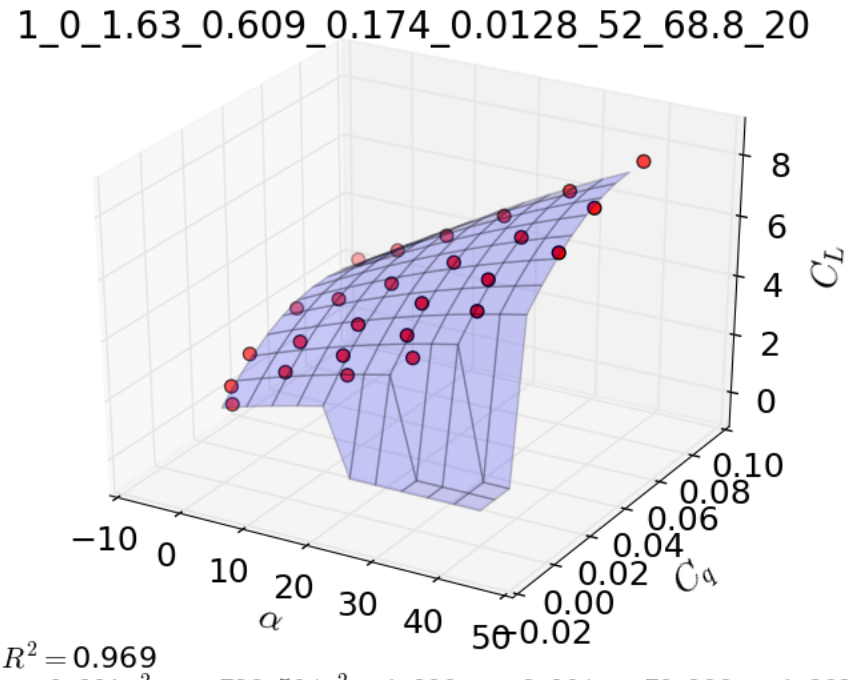

$R^2 = 0.969$

$C_L(x, y) = -0.001x^2 + -728.594y^2 + 1.006xy + 0.064x + 78.066y + 1.368$

Figure C.55: Surface fit C_L for θ=20[°]

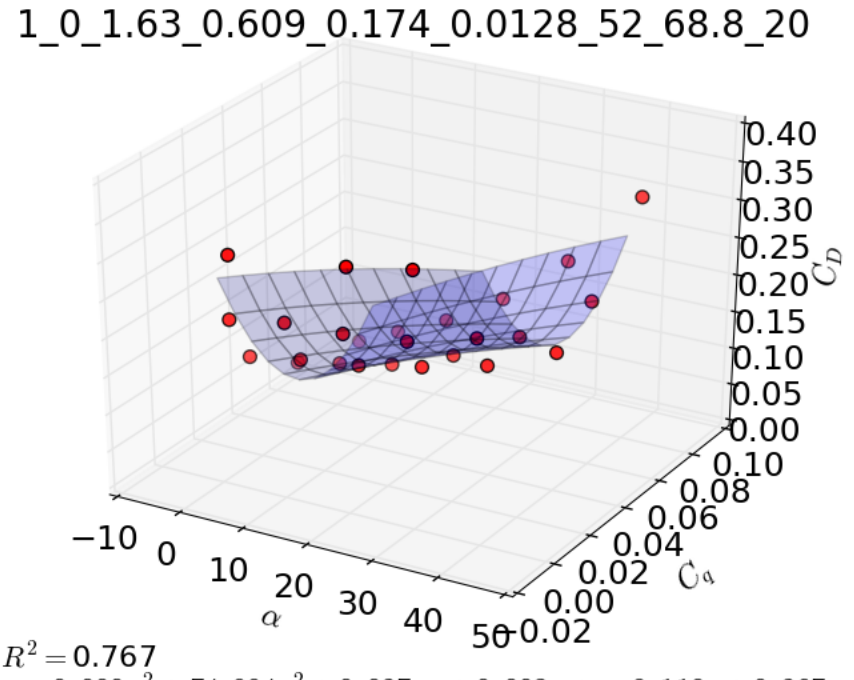

$R^2 = 0.767$

$C_D(x, y) = -0.000x^2 + 74.994y^2 + 0.027xy + 0.003x + -8.118y + 0.267$

Figure C.56: Surface fit C_D for θ=20[°]

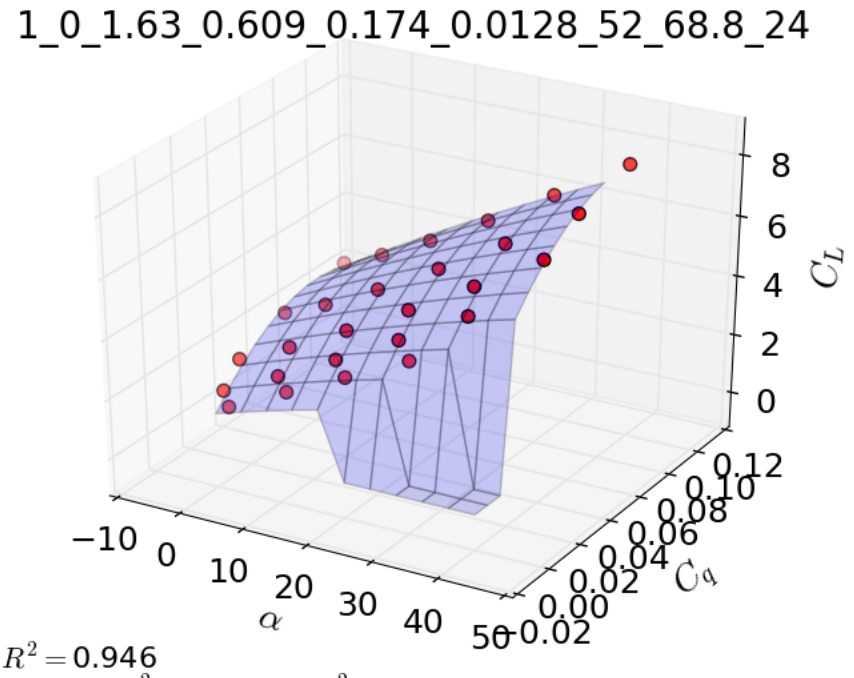

$R^2 = 0.946$

$C_L(x, y) = -0.000x^2 + -598.252y^2 + 0.798xy + 0.065x + 74.476y + 1.308$

Figure C.57: Surface fit C_L for θ=24[°]

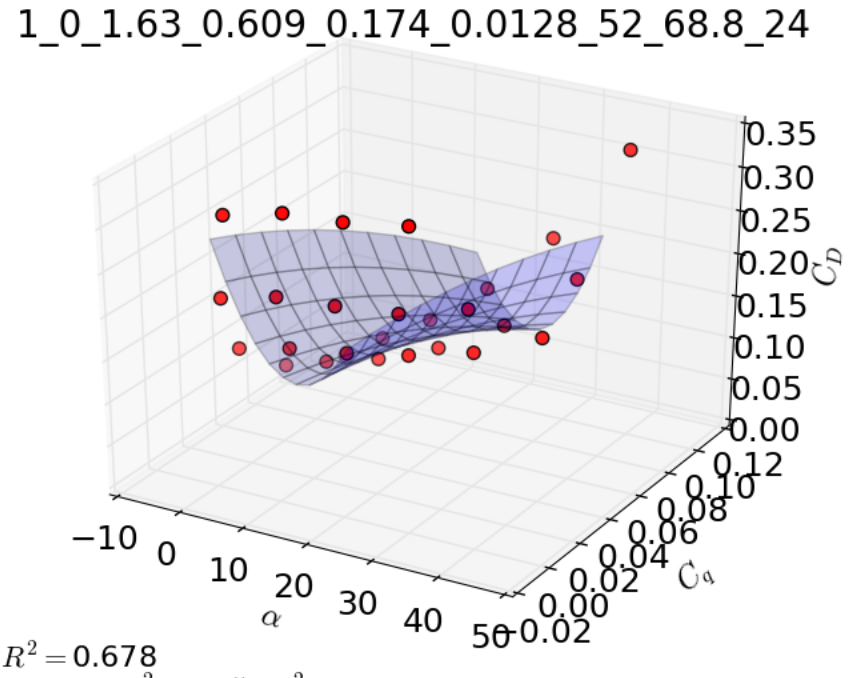

$R^2 = 0.678$

$C_D(x, y) = -0.000x^2 + 60.548y^2 + 0.047xy + 0.003x + -7.706y + 0.281$

Figure C.58: Surface fit C_D for θ=24[°]

C.6 Variation in suction location

Variation in θ_m.

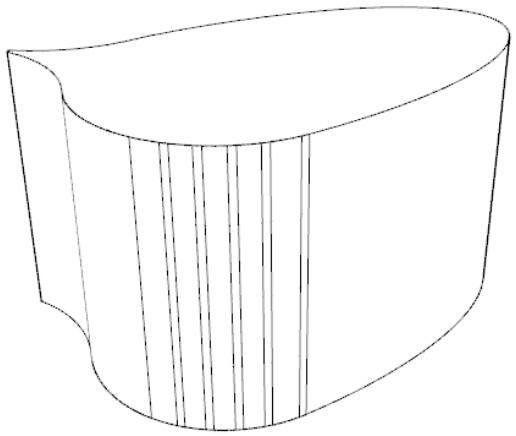

Figure C.59: Configurations θ_m variation

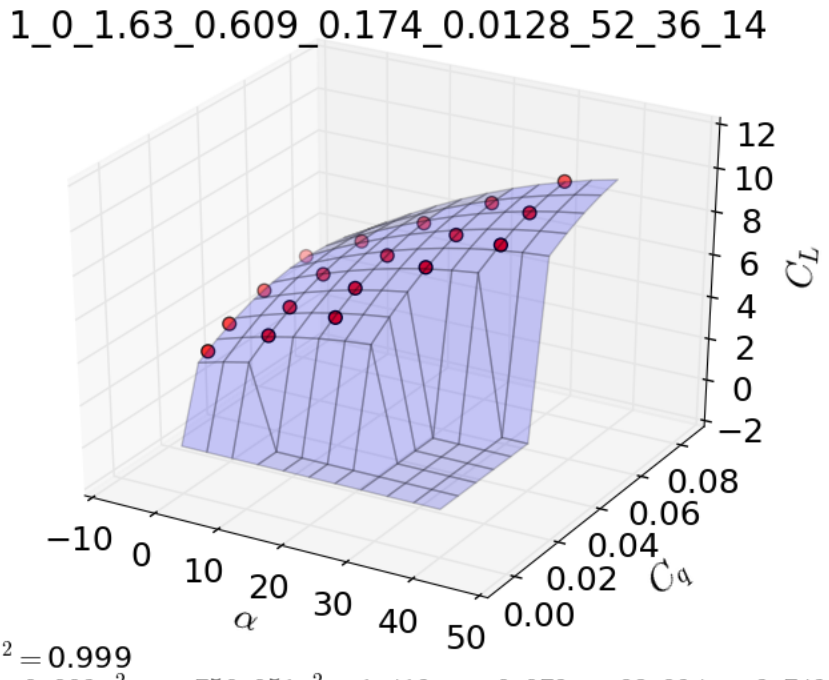

$R^2 = 0.999$

$C_L(x, y) = -0.002x^2 + -759.051y^2 + 1.412xy + 0.072x + 83.824y + 2.742$

Figure C.60: Surface fit C_L for θ_m=36[°]

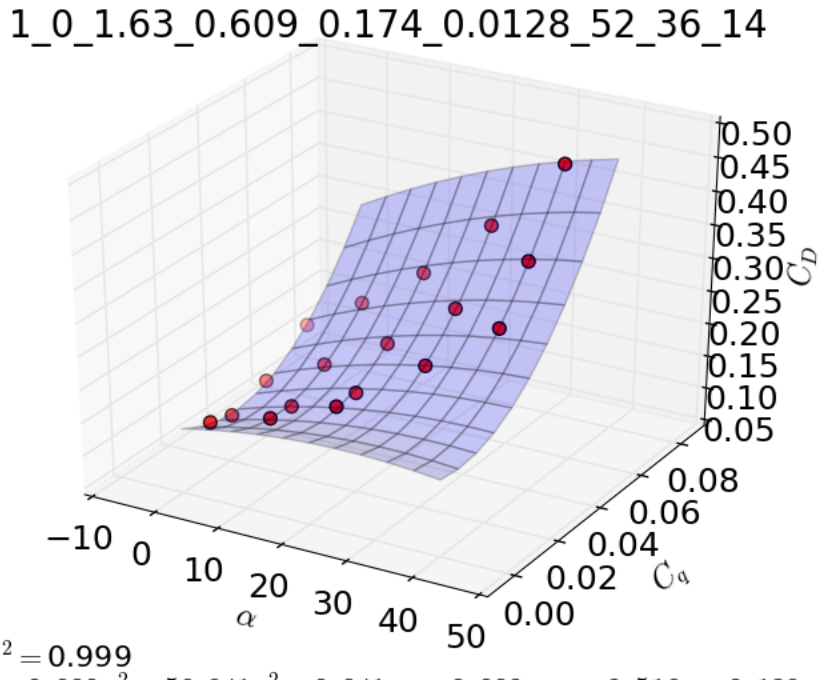

$R^2 = 0.999$

$C_D(x, y) = -0.000x^2 + 56.841y^2 + 0.041xy + 0.002x + -2.516y + 0.139$

Figure C.61: Surface fit C_D for θ_m=36[°]

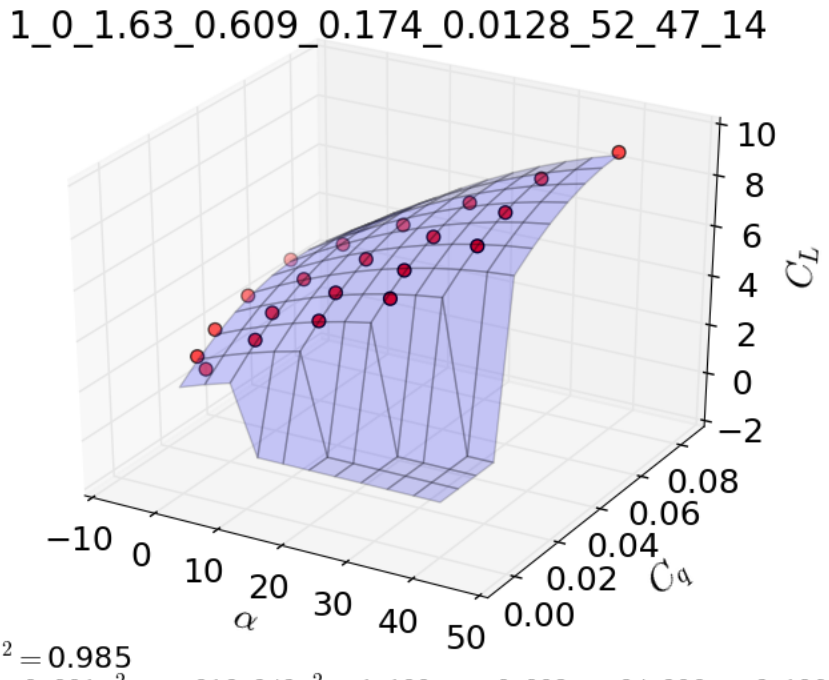

$R^2 = 0.985$

$$C_L(x, y) = -0.001x^2 + -812.242y^2 + 1.188xy + 0.093x + 84.288y + 2.106$$

Figure C.62: Surface fit C_L for θ_m=47[°]

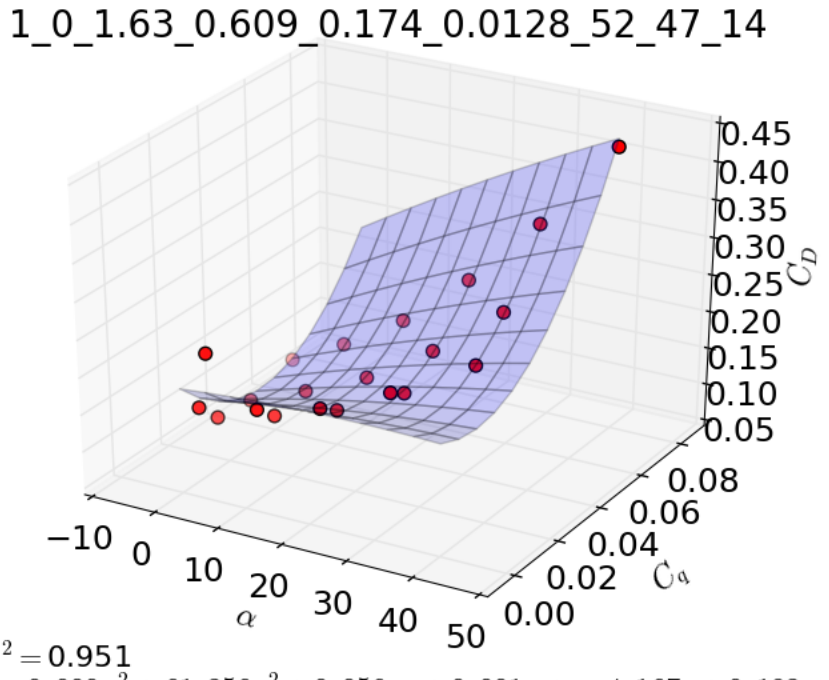

$R^2 = 0.951$

$$C_D(x, y) = -0.000x^2 + 61.356y^2 + 0.056xy + 0.001x + -4.167y + 0.183$$

Figure C.63: Surface fit C_D for θ_m=47[°]

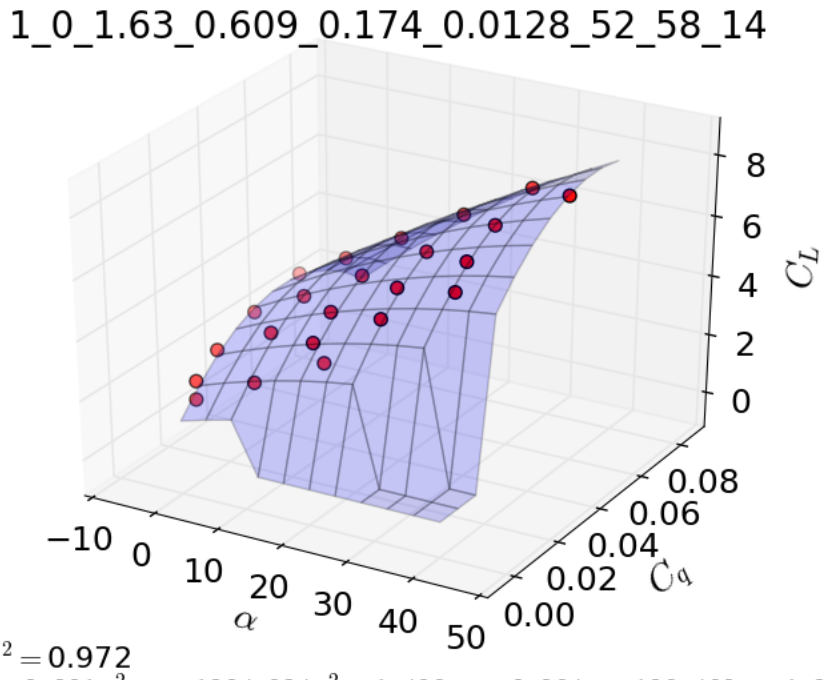

$R^2 = 0.972$

$$C_L(x, y) = -0.001x^2 + -1204.934y^2 + 1.496xy + 0.064x + 106.460y + 1.283$$

Figure C.64: Surface fit C_L for θ_m=58[°]

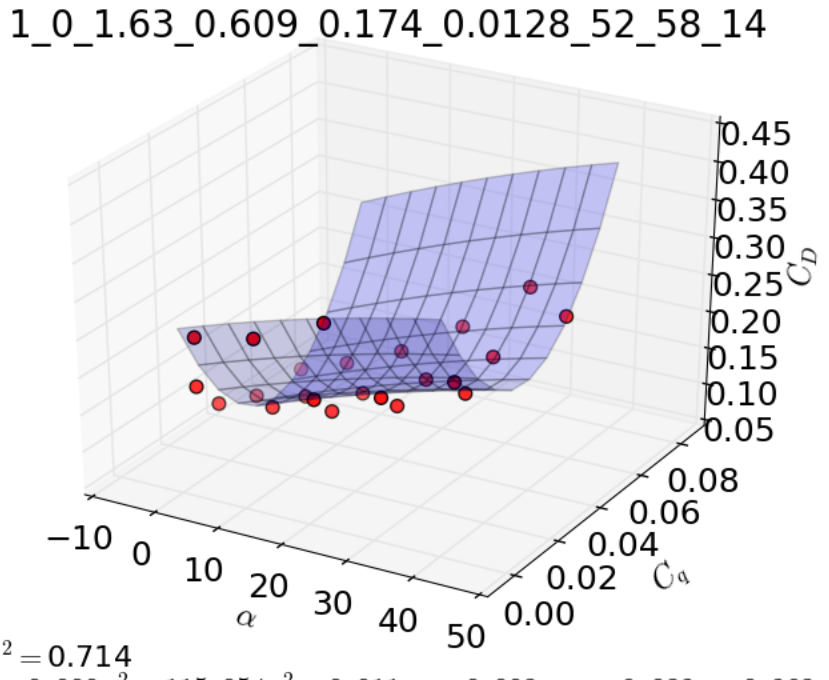

$R^2 = 0.714$

$$C_D(x, y) = -0.000x^2 + 115.054y^2 + 0.011xy + 0.003x + -9.032y + 0.263$$

Figure C.65: Surface fit C_D for θ_m=58[°]

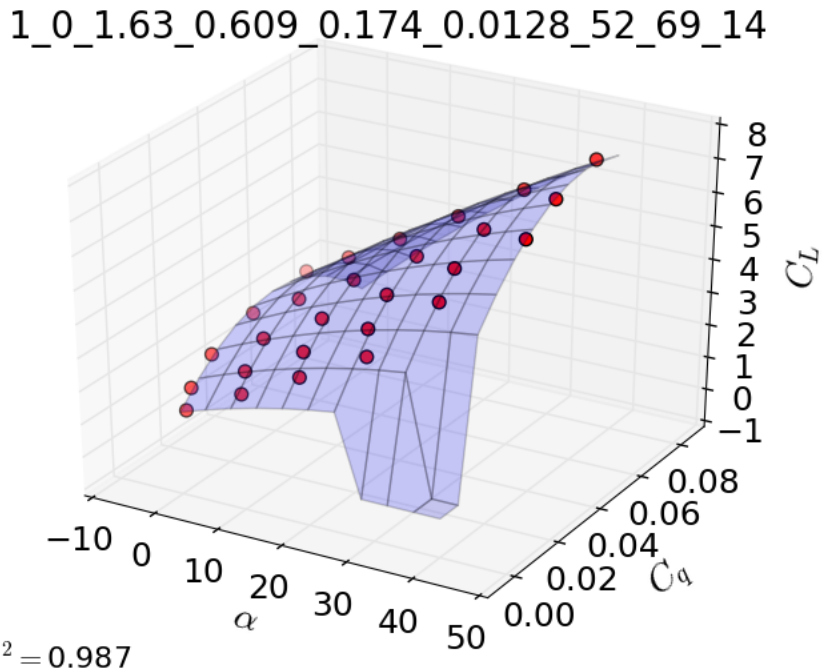

$R^2 = 0.987$

$$C_L(x, y) = -0.001x^2 + -1102.330y^2 + 1.362xy + 0.066x + 89.807y + 1.327$$

Figure C.66: Surface fit C_L for θ_m=69[°]

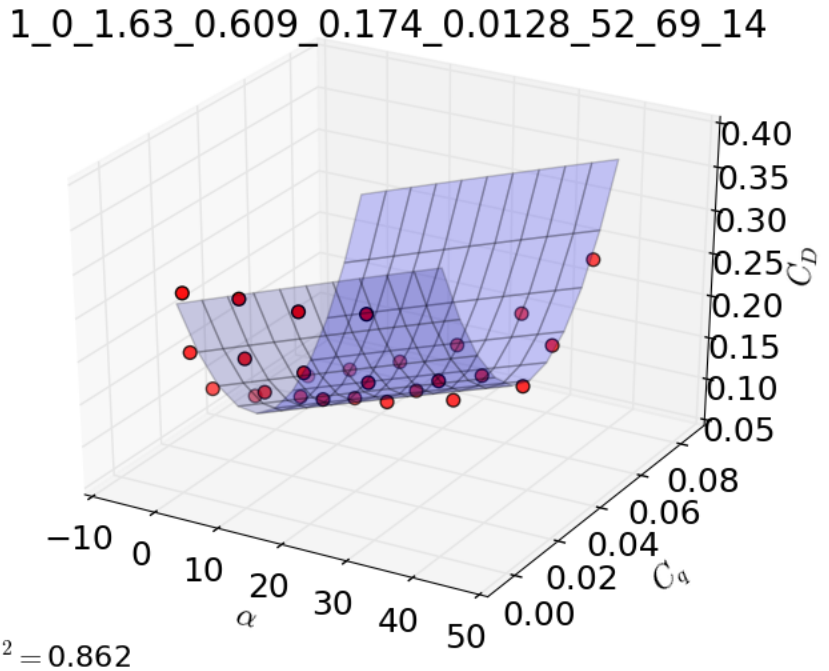

$R^2 = 0.862$

$$C_D(x, y) = -0.000x^2 + 120.403y^2 + -0.001xy + 0.003x + -9.719y + 0.265$$

Figure C.67: Surface fit C_D for θ_m=69[°]

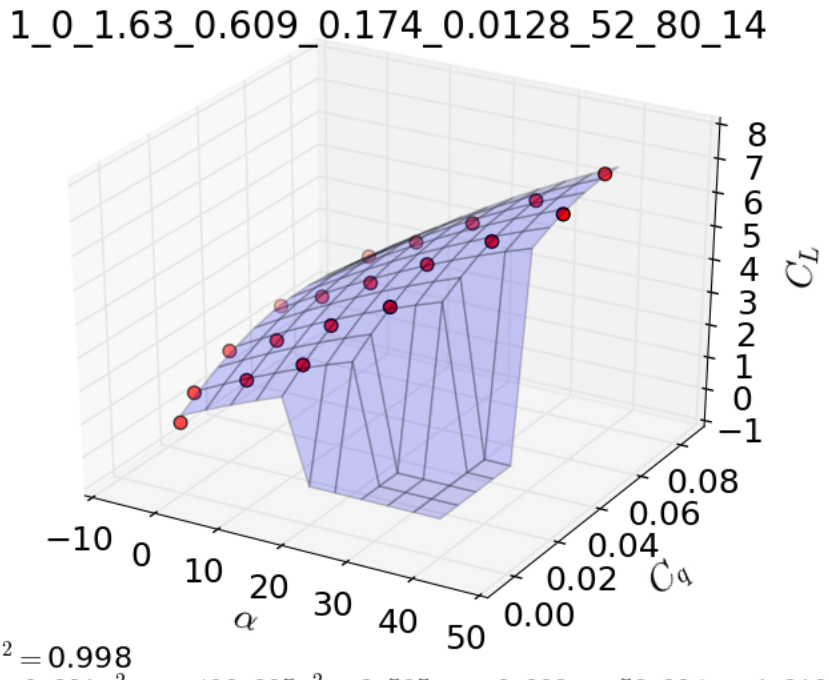

$R^2 = 0.998$

$$C_L(x, y) = -0.001x^2 + -492.895y^2 + 0.585xy + 0.092x + 52.924y + 1.216$$

Figure C.68: Surface fit C_L for θ_m=80[°]

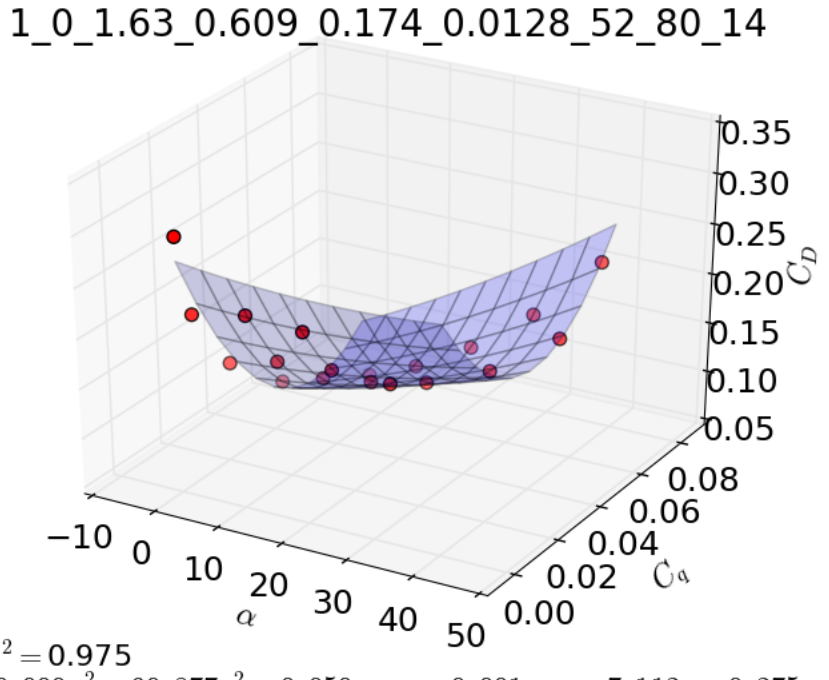

$R^2 = 0.975$

$$C_D(x, y) = 0.000x^2 + 60.877y^2 + 0.050xy + -0.001x + -7.112y + 0.275$$

Figure C.69: Surface fit C_D for θ_m=80[°]